

1993

# A model of coal combustion dynamics in a fluidized bed combustor

Kenneth William Junk  
*Iowa State University*

Follow this and additional works at: <https://lib.dr.iastate.edu/rtd>

 Part of the [Chemical Engineering Commons](#), and the [Mechanical Engineering Commons](#)

## Recommended Citation

Junk, Kenneth William, "A model of coal combustion dynamics in a fluidized bed combustor " (1993). *Retrospective Theses and Dissertations*. 10459.  
<https://lib.dr.iastate.edu/rtd/10459>

This Dissertation is brought to you for free and open access by the Iowa State University Capstones, Theses and Dissertations at Iowa State University Digital Repository. It has been accepted for inclusion in Retrospective Theses and Dissertations by an authorized administrator of Iowa State University Digital Repository. For more information, please contact [digirep@iastate.edu](mailto:digirep@iastate.edu).

## **INFORMATION TO USERS**

This manuscript has been reproduced from the microfilm master. UMI films the text directly from the original or copy submitted. Thus, some thesis and dissertation copies are in typewriter face, while others may be from any type of computer printer.

**The quality of this reproduction is dependent upon the quality of the copy submitted.** Broken or indistinct print, colored or poor quality illustrations and photographs, print bleedthrough, substandard margins, and improper alignment can adversely affect reproduction.

In the unlikely event that the author did not send UMI a complete manuscript and there are missing pages, these will be noted. Also, if unauthorized copyright material had to be removed, a note will indicate the deletion.

Oversize materials (e.g., maps, drawings, charts) are reproduced by sectioning the original, beginning at the upper left-hand corner and continuing from left to right in equal sections with small overlaps. Each original is also photographed in one exposure and is included in reduced form at the back of the book.

Photographs included in the original manuscript have been reproduced xerographically in this copy. Higher quality 6" x 9" black and white photographic prints are available for any photographs or illustrations appearing in this copy for an additional charge. Contact UMI directly to order.

# U·M·I

University Microfilms International  
A Bell & Howell Information Company  
300 North Zeeb Road, Ann Arbor, MI 48106-1346 USA  
313/761-4700 800/521-0600



**Order Number 9321176**

**A model of coal combustion dynamics in a fluidized bed combustor**

**Junk, Kenneth William, Ph.D.**

**Iowa State University, 1993**

**U·M·I**  
300 N. Zeeb Rd.  
Ann Arbor, MI 48106



**A model of coal combustion dynamics  
in a fluidized bed combustor**

**by**

**Kenneth William Junk**

**A Dissertation Submitted to the  
Graduate Faculty in Partial Fulfillment of the  
Requirements for the Degree of  
DOCTOR OF PHILOSOPHY**

**Department: Mechanical Engineering  
Major: Mechanical Engineering**

**Approved:** \_\_\_\_\_

Signature was redacted for privacy.

**In Charge of Major Work**

Signature was redacted for privacy.

**For the Major Department**

Signature was redacted for privacy.

**For the Graduate College**

**Iowa State University  
Ames, Iowa**

**1993**

## TABLE OF CONTENTS

<b>LIST OF FIGURES</b> .....	<b>v</b>
<b>LIST OF TABLES</b> .....	<b>viii</b>
<b>NOMENCLATURE</b> .....	<b>ix</b>
<b>1. INTRODUCTION</b> .....	<b>1</b>
<b>2. THE NONLINEAR COAL COMBUSTION MODEL</b> .....	<b>4</b>
2.1 Fluidized Bed Dynamics .....	4
2.2 Volatile Combustion .....	5
2.3 Char Combustion .....	7
2.3.1 The Population Balance Equation .....	13
2.3.2 Impulse Response of a Monodispersed Coal Distribution .....	16
2.3.3 Impulse Response of an Arbitrary Particle Distribution .....	18
2.3.4 Char Consumption for a Block Particle Distribution .....	20
2.4 Refinements of the Char Combustion Model .....	23
<b>3. LINEAR SYSTEM IDENTIFICATION THEORY</b> .....	<b>32</b>
3.1 Discrete-Time System Identification .....	32
3.1.1 Least-Squares Parameter Estimation .....	34
3.1.2 Extended Least-Squares Parameter Estimation .....	37

3.1.3	Remarks on Discrete-Time System Identification .....	43
3.2	Frequency Domain System Identification .....	44
3.2.1	Nonparametric Spectral Estimation Methods .....	45
3.2.2	Parametric Spectral Estimation Methods .....	52
3.3	Continuous-Time System Identification .....	56
3.3.1	Calculation of PMF Coefficients .....	57
3.3.2	Estimation of System Parameters from PMF Coefficients .....	59
3.3.3	Performance of the PMF Method: A Comparative Example .....	62
<b>4.</b>	<b>EXPERIMENTAL APPARATUS AND PROCEDURES .....</b>	<b>64</b>
4.1	Combustor Design .....	64
4.2	Data Acquisition .....	66
4.3	Experimental Procedures .....	67
<b>5.</b>	<b>RESULTS AND DISCUSSION .....</b>	<b>69</b>
5.1	The Nonlinear Combustion Model: Small Particle Distributions .....	69
5.2	The Nonlinear Combustion Model: Large Particle Distributions .....	72
5.3	The Linear Combustion Model: Small Particle Distributions .....	84
5.4	The Linear Combustion Model: Large Particle Distributions .....	95
<b>6.</b>	<b>CONCLUSION .....</b>	<b>102</b>
	<b>REFERENCES .....</b>	<b>105</b>
	<b>APPENDIX A: DERIVATION OF EQ. (2.60) .....</b>	<b>109</b>

<b>APPENDIX B: ELS AND PMF MATLAB MACROS .....</b>	<b>114</b>
<b>APPENDIX C: DERIVATION OF EQ. (3.72) .....</b>	<b>118</b>

## LIST OF FIGURES

Fig. 2.1:	Concentration profiles of Avedesian and Davidson's two-film combustion model .....	8
Fig. 2.2:	Impulse response of a monodispersed particle distribution .....	13
Fig. 2.3:	Impulse response of van der Post's linear transfer function approximation .....	16
Fig. 2.4:	Typical impulse response of a block particle distribution .....	22
Fig. 2.5:	Oxygen balance variable designations .....	23
Fig. 2.6:	Block diagram of the char combustion process .....	25
Fig. 2.7:	Combustion model No. 1 .....	30
Fig. 2.8:	Combustion model No. 2 .....	30
Fig. 2.9:	Combustion model No. 3 .....	31
Fig. 3.1:	Unbiased least-squares model .....	37
Fig. 3.2:	Unbiased extended least-squares model .....	38
Fig. 3.3:	Block diagram of the system to be identified .....	47
Fig. 3.4:	Frequency response estimate of Eq. (3.60) from a single periodogram .....	51
Fig. 3.5:	Frequency response estimate of Eq. (3.60) from the average of 50 periodograms .....	51
Fig. 3.6:	Block diagram of a Poisson filter chain .....	57

Fig. 4.1:	Schematic diagram of the experimental apparatus .....	65
Fig. 5.1:	Typical small particle response .....	70
Fig. 5.2:	Small particle char model (16 × 18 mesh) .....	73
Fig. 5.3:	Small particle char model (16 × 20 mesh) .....	74
Fig. 5.4:	Small particle char model (16 × 25 mesh) .....	75
Fig. 5.5:	Small particle char model (16 × 30 mesh) .....	76
Fig. 5.6:	Cumulative mass distribution .....	78
Fig. 5.7:	Estimated initial $\lambda$ distribution .....	79
Fig. 5.8:	Large particle char model (3.5 × 4 mesh) .....	80
Fig. 5.9:	Uniform $\lambda$ distribution .....	82
Fig. 5.10:	Theoretical impulse response for a uniform $\lambda$ distribution .....	83
Fig. 5.11:	Impulse response of the PMF estimated transfer function (16 × 18 mesh) .....	87
Fig. 5.12:	Impulse response of the PMF estimated transfer function (16 × 20 mesh) .....	88
Fig. 5.13:	Impulse response of the PMF estimated transfer function (16 × 25 mesh) .....	89
Fig. 5.14:	Impulse response of the PMF estimated transfer function (16 × 30 mesh) .....	90
Fig. 5.15:	Impulse response of the decomposed transfer function (16 × 18 mesh) .....	91
Fig. 5.16:	Impulse response of the decomposed transfer function (16 × 20 mesh) .....	92

Fig. 5.17: Impulse response of the decomposed transfer function (16 × 25 mesh) .....	93
Fig. 5.18: Impulse response of the decomposed transfer function (16 × 30 mesh) .....	94
Fig. 5.19: Impulse response of the PMF estimated transfer function (3.5 × 4 mesh) .....	97
Fig. 5.20: Impulse response of the decomposed transfer function (3.5 × 4 mesh) .....	98
Fig. 5.21: Impulse response of the PMF estimated transfer function (6 × 7 mesh) .....	99
Fig. 5.22: Impulse response of the decomposed transfer function (6 × 7 mesh) .....	100
Fig. A.1 Maclaurin series approximations of Eq. (A.2) .....	112

**LIST OF TABLES**

<b>Table 2.1: Variable designations for Eq. (2.20)</b> .....	<b>11</b>
<b>Table 2.2: Summary of impulse response models</b> .....	<b>29</b>
<b>Table 2.3: Coal combustion model parameters</b> .....	<b>29</b>
<b>Table 3.1: Performance of the ELS algorithm</b> .....	<b>40</b>
<b>Table 3.2: Performance of the PMF algorithm</b> .....	<b>63</b>
<b>Table 4.1: Indiana bituminous coal analyses</b> .....	<b>67</b>
<b>Table 5.1: Mass fractions for uniform <math>\lambda</math> distributions</b> .....	<b>71</b>
<b>Table 5.2: Impulse response data</b> .....	<b>72</b>
<b>Table 5.3: Transfer function estimates for small particle distributions</b> .....	<b>86</b>

**NOMENCLATURE***Coal combustion variables*

$A_r$	Cross-sectional area of the fluidized bed reactor ( $m^2$ )
$C_A$	Concentration of species A ( $kmol/m^3$ )
$C_b$	Oxygen concentration at the exit ( $kmol/m^3$ )
$C_o$	Oxygen concentration at the inlet ( $kmol/m^3$ )
$C_p$	Oxygen concentration in the emulsion phase ( $kmol/m^3$ )
$C_s$	Oxygen concentration at the particle surface ( $kmol/m^3$ )
$D$	Particle diameter (m)
$D_o$	Initial particle diameter (m)
$D_{AB}$	Binary molecular diffusion coefficient ( $m^2/s$ )
$E_a$	Activation energy ( $J/kmol$ )
$F$	Coal feed rate per unit size ( $kg/m/s$ )
$F_o$	Coal feed rate per unit mass ( $1/s$ )
$f$	Combustion rate coefficient ( $m^2/s$ )
$G$	Volumetric flow rate ( $m^3/s$ )
$h(\cdot)$	Heaviside step function

<b>J</b>	<b>Molar flux kmol/m<sup>3</sup>/s</b>
<b>k</b>	<b>Frequency factor for volatile generation (1/s)</b>
<b>k<sub>o</sub></b>	<b>Frequency factor for char combustion (1/s)</b>
<b>K(t)</b>	<b>Rate of char consumption (kg/s)</b>
<b>K</b>	<b>Overall burning coefficient (m/s)</b>
<b>m<sub>c</sub></b>	<b>Mass of carbon (kg)</b>
<b>M<sub>c</sub></b>	<b>Molecular weight of carbon (kg/kmol)</b>
<b>N</b>	<b>Total number of particles; upper index limit</b>
<b>r</b>	<b>Radial distance from the center of a particle (m)</b>
<b>r<sub>A</sub></b>	<b>Rate of generation (or consumption) of species A (kmol/s)</b>
<b>R<sub>u</sub></b>	<b>Universal gas constant (J/kmol/K)</b>
<b>R(t)</b>	<b>Shrinking rate of coal particles (m/s)</b>
<b>Sh</b>	<b>Sherwood number</b>
<b>t</b>	<b>Time (s)</b>
<b>T</b>	<b>Temperature (K)</b>
<b>U</b>	<b>Superficial velocity (m/s)</b>
<b>U<sub>mf</sub></b>	<b>Superficial velocity at minimum fluidization (m/s)</b>
<b>v</b>	<b>Bulk fluid velocity (m/s)</b>
<b>V</b>	<b>Volatile fraction</b>
<b>V*</b>	<b>Maximum volatile fraction</b>
<b>V<sub>r</sub></b>	<b>Volume of the fluidized bed reactor</b>

<b>x</b>	<b>Mass fraction</b>
<b>X</b>	<b>Cross-flow factor</b>
<b>Y</b>	$Y = [U - (U - U_{mf}) \exp(-X)]$ (m/s)

### Greek Symbols

$\delta(\cdot)$	Dirac delta function
$\varepsilon$	Bed voidage
$\phi_0$	Initial mass distribution of coal particles (kg/mm)
$\rho_c$	Density of char (kg/m <sup>3</sup> )
$\rho_s$	Density of sand (kg/m <sup>3</sup> )
$\lambda$	Mass distribution of coal particles (kg/mm)

### *System identification variables*

<b>E</b>	<b>Expectation operator</b>
<b>e</b>	<b>Output error</b>
$f_k$	<b>k<sup>th</sup>-order Poisson moment functional</b>
<b>I</b>	<b>Identity matrix</b>
<b>k</b>	<b>Sequential index</b>
<b>P</b>	<b>Covariance matrix</b>
<b>q</b>	<b>Forward-shift operator</b>
$q^{-1}$	<b>Backward-shift operator</b>
<b>R</b>	<b>Correlation function</b>

$s$	Laplace transform variable
$S$	Power spectral density function
$t$	Time (s)
$T$	Final time (s)
$u$	System input
$u_F$	Filtered system input
$y$	System output
$y_F$	Filtered system output
$z$	Discrete transform variable

### Greek Symbols

$\delta$	Kronecker delta function; Dirac delta function
$\lambda$	Poisson filter chain constant
$\eta$	Filtered output error
$\phi$	Data vector
$\psi$	Filtered data vector
$\sigma^2$	Variance
$\theta$	Coefficient vector
$\omega$	Frequency (rad/s)

Usage: **Bold type** denotes a vector or matrix.  
 The diacritical (^) denotes an estimate.

## 1. INTRODUCTION

Since the early 1970s, considerable attention has been directed towards coal combustion in fluidized bed combustors. Most of this work focuses on steady-state or end-point analyses [36]. Indeed, little attention has been directed towards transient responses, which contain significant information about the mechanisms of coal combustion. Accordingly, analyses of transient responses, such as step and impulse responses, can provide a better understanding of coal combustion in fluidized beds. While step and impulse responses contain the same information, system dynamics, especially fast dynamics, are more pronounced with impulse responses. In practice, impulse functions cannot be generated, but they can be approximated by a finite block pulse function (i.e., a "batch" test). In this light, this investigation examines coal combustion dynamics by generating CO<sub>2</sub> profiles from batch tests of coal.

When coal is introduced into a fluidized bed, two distinct combustion processes take place: volatile combustion and char combustion. For coal, volatiles are quickly consumed, leaving a slow-burning char residual. Although the details of volatile release and combustion are not well understood, the overall process can be approximated as a first-order chemical reaction [33]. In turn, for small perturbations in temperature, this reaction can be modeled as an exponential decay.

In contrast with volatile combustion, the mechanisms of char combustion are better understood. For example, Avedesian and Davidson [3] model char combustion as a shrinking sphere with a diffusion rate-limited chemical reaction. Ross and Davidson [29]

refine this model by including chemical kinetics. However, neither model adequately describes the transient response of char combustion in a fluidized bed. While the model premises are accurate, they are incomplete. Both models are predicated upon strictly monodispersed coal samples; however, monodispersed samples are rarely attained in practice. (The exception is a single coal particle, which is a limiting case.) In the laboratory, "monodispersed" samples actually comprise particle distributions wide enough to significantly affect transient responses. Furthermore, when large-particle bituminous coal is introduced into a fluidized bed combustor, some particles fragment [7], creating a wide initial particle distribution. This fragmented particle distribution has a profound effect on the transient CO<sub>2</sub> response. Consequently, to accurately model the transient characteristics of char combustion, the effects of particle distributions should be addressed.

This investigation has two objectives. The first objective is to develop a nonlinear, transient model of coal combustion in a fluidized bed combustor. This model is carried out on the premise that char combustion and volatile combustion are distinct and separable processes. For an impulse in the coal feed rate, volatile combustion is modeled as an exponential decay. On the other hand, the transient model of char combustion is based on a closed-form solution to a population balance equation. To verify this model, theoretical responses are compared with experimental data obtained from batch tests of coal with known initial distributions.

The second objective of this investigation is to develop a linear, time-invariant transfer function that approximates the dynamics of coal combustion. Provided that deviations are small, linear transfer functions offer many advantages over their nonlinear counterparts. Chief among these, linear system theory is well developed and often reduces the complexity of system analysis to manageable levels. However, as with many chemical processes, data signals from fluidized bed systems invariably contain measurement noise.

Consequently, this investigation examines the applicability of various system identification algorithms to processes with significant measurement noise. Included in this investigation are studies of discrete-time domain, frequency domain, and continuous-time domain algorithms.

## **2. THE NONLINEAR COAL COMBUSTION MODEL**

Materials in this chapter review some of the important considerations concerning mixing dynamics, volatile combustion, and char combustion in bubbling bed combustors. In addition to briefly reviewing current literature, this chapter presents a new transient model of char combustion in a fluidized bed.

This chapter has been divided into four sections. In Section 2.1, fluidized bed modeling assumptions are presented, and the applicability of a quasi-steady approximation is briefly discussed. Volatile combustion transients are developed and discussed in Section 2.2, char combustion transients in Section 2.3. Finally, Section 2.4 examines refinements to the char combustion model.

### **2.1 Fluidized Bed Dynamics**

Fluidized bed combustors are characterized by turbulent fluid flow, making modeling difficult. Fortunately, turbulence in a bubbling bed is vigorous enough that the overall system can be adequately modeled as continuously stirred tank reactor (CSTR). As a CSTR, the reactor contents are presumed to be perfectly mixed so that spatial gradients in temperature, gas concentrations, and reaction rates can be neglected. Without spatial gradients, CO<sub>2</sub> concentrations exiting the combustor are described by the mass balance equation

$$V_R \frac{d}{dt} C_{\text{CO}_2}(t) + G C_{\text{CO}_2}(t) = r_v(t) + r_c(t) \quad (2.1)$$

where  $r_v$  is the rate of CO<sub>2</sub> production from volatile combustion, and  $r_c$  is the rate of CO<sub>2</sub> production from char combustion. Note that volatile combustion and char combustion are assumed to be separable. If mixing dynamics are fast, a quasi-steady approximation can be used to reduce the mass balance equation to

$$C_{\text{CO}_2}(t) = \frac{1}{G} [r_v(t) + r_c(t)] \quad (2.2)$$

In essence, mixing dynamics associated with the combustion chamber, freeboard, and gas sampling system behave as low-pass filters. A quasi-steady approximation is appropriate when the eigenvalues associated with mixing dynamics are much faster than CO<sub>2</sub> transients. In this study, mixing dynamics are much faster than char combustion transients and can be neglected. In contrast with char combustion transients, volatile combustion transients are fast enough that mixing dynamics cannot be neglected. In this case, measured CO<sub>2</sub> transients from volatile combustion are low-pass filtered versions of the actual CO<sub>2</sub> transients.

## 2.2 Volatile Combustion

When coal first enters a fluidized bed, it undergoes rapid thermal decomposition, releasing volatile matter, such as methane, tar, and other hydrocarbons [5,32,33]. For bituminous coals, volatile content can account for 30% to 50% of the total coal weight [5].

As a first approximation, volatile mass released from a batch of coal can be described through the single reaction model [1,5,32]

$$\frac{dV}{dt} = k(V^* - V) \quad (2.3)$$

where  $V^*$  denotes total volatile mass and  $k$  is defined by the Arrhenius relation

$$k = A \exp(-E_a / R_u T) \quad (2.4)$$

If perturbations in temperature are small,  $k$  is approximately constant. For zero initial conditions and  $k$  constant, Eq. (2.3) can be integrated with respect to time so that  $V(t)$  exponentially approaches  $V^*$ . Once created, volatiles are assumed to oxidize immediately to form  $\text{CO}_2$ . Because volatiles oxidize quickly, oxidation transients can be neglected, making  $\text{CO}_2$  concentrations directly proportional to the rate of volatile generation,  $dV(t)/dt$ ; that is,

$$C_{\text{CO}_2}(t) = g_o e^{-kt} \quad (2.5)$$

where  $g_o$  is a constant that is dependent on the mass and type of coal and inversely proportional to the volumetric air flow rate through the bed. Suuberg et al. [34] suggest that this model can be improved by accounting for multiple, parallel reactions. Using a multireaction model, Suuberg et al. approximate species generation as a collection of independent, first-order reactions such that for species  $i$ ,  $i = 1, 2, 3, \dots, N$ ,

$$\frac{dV_i}{dt} = k_i (V_i^* - V_i) \quad (2.6)$$

where

$$k_i = A_i \exp(-E_{a,i} / R_u T) \quad (2.7)$$

Anthony [1], Borghi [5], and Sarofim [32] use similar multireaction models. However, for mathematical tractability, they assume that all reactions have a common preexponential factor and that activation energies are normally distributed. Independent of these restrictions, the multireaction model suggests that, for small perturbations in temperature,  $\text{CO}_2$  production from each species exponentially approaches zero. Because volatiles are quickly consumed, each exponential can be approximated by a first-order Maclaurin series expansion:

$$\begin{aligned} C_{\text{CO}_2}(t)_i &= g_{o,i} \exp(-k_i t) \\ &\approx g_{o,i} (1 - k_i t) \end{aligned} \quad (2.8)$$

For a discrete distribution of species,  $h_i$ ,  $i = 1, 2, \dots, N$ , the total  $\text{CO}_2$  concentration leaving the combustor can be approximated by the summation

$$C_{\text{CO}_2}(t) \approx \sum_{i=1}^N h_i g_{o,i} (1 - k_i t) = \left( \sum_{i=1}^N h_i g_{o,i} \right) \left[ 1 - \frac{\left( \sum_{i=1}^N h_i g_{o,i} k_i \right)}{\sum_{i=1}^N h_i g_{o,i}} t \right] \quad (2.9)$$

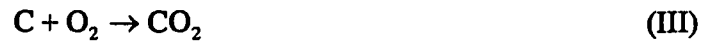
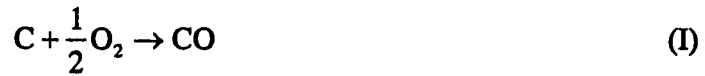
In turn, for  $t \geq 0$ , Eq. (2.9) can be approximated by the exponential

$$C_{\text{CO}_2}(t) \approx \left( \sum_{i=1}^N h_i g_{o,i} \right) \exp \left[ - \frac{\sum_{i=1}^N h_i g_{o,i} k_i}{\sum_{i=1}^N h_i g_{o,i}} t \right] \quad (2.10)$$

Comparison of the multireaction response, Eq. (2.10), with the single reaction response, Eq. (2.5), suggests that, independent of the model basis, the impulse response can be described as an exponential decay. However, with either approach, volatile combustion transients are fast enough where instrumentation dynamics become important and care must be taken to separate the volatile response from the instrumentation response.

### 2.3 Char Combustion

Volatiles are liberated from coal within a few seconds, leaving a slow burning char residual. Combustion times for char, a porous, carbonaceous material, are roughly one to two orders of magnitude larger than those of volatiles [32,33]. In contrast with volatile combustion, the mechanisms of char combustion are better understood. However, the precise mechanisms describing the oxidation of solid carbon remain elusive. Most research into these mechanisms concentrate on the following four reactions [17,36]:



Avedesian and Davidson [3] were the first to model char combustion in a fluidized bed. Their approach is based on a two-film model in which oxygen diffuses towards the char particle but is completely consumed by CO (reaction II) before it reaches the particle surface, producing a film of O<sub>2</sub> and CO<sub>2</sub>. A second film forms when CO<sub>2</sub> diffuses towards the particle surface and reacts with solid carbon to form 2CO (reaction IV). This model is illustrated in Fig. 2.1.

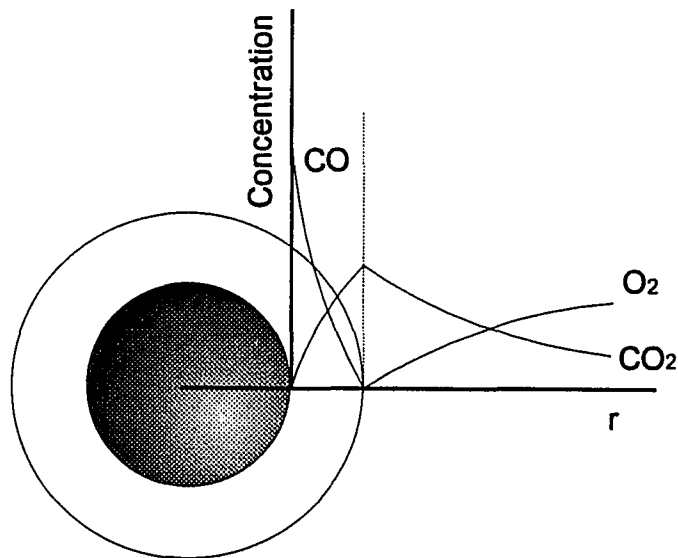


Fig. 2.1: Concentration profiles of Avedesian and Davidson's two-film combustion model

Subsequent work on the mechanisms of char combustion show that, at typical bed operating temperatures, reaction IV proceeds slowly and can be neglected [17,29,36]. As a result, the two-film model has been revised. Current models assume that O<sub>2</sub> diffuses towards the particle surface and reacts with C to form CO (reaction I). CO then diffuses from the particle surface and reacts with O<sub>2</sub> in accordance with reaction II to form CO<sub>2</sub>. In these models, reaction III is often ignored since it proceeds at a far slower rate than reaction I [17].

The location of reaction II is a matter of contention. Traditional models assume that CO oxidizes to CO<sub>2</sub> close to the particle surface so that the overall reaction is effectively  $C + O_2 \rightarrow CO_2$  [29]. Other models assume that reaction II proceeds so slowly that little CO<sub>2</sub> is produced near the surface. Instead, CO diffuses from the particle surface and burns in the interstices of the emulsion-phase [29]. In contrast with these models, Hayhurst theorizes that the emulsion-phase interstices are small enough to quench a CO flame [17]. In other words, the emulsion-phase behaves as a flame arrester. Hayhurst contends that CO diffuses to the bubble-phase where it is consumed by O<sub>2</sub> within the bubbles.

The location of reaction II is not critical in formulating the system response to a batch input of coal. Whether CO<sub>2</sub> diffuses from the particle surface or whether 2CO diffuses from the particle surface, the governing equations are the same. In either case, a continuity equation can be written for species  $A$ ,  $A \in \{O_2, CO, CO_2\}$ :

$$\frac{\partial C_A}{\partial t} + \nabla \cdot (C_A \mathbf{v}) = \nabla \cdot (D_{AB} \nabla C_A) + r_A \quad (2.11)$$

where  $\mathbf{v}$  is the bulk fluid velocity,  $D_{AB}$  is a binary diffusion coefficient, and  $r_A$  is the rate at which species  $A$  is generated (or consumed). Provided that concentration profiles develop quickly, a quasi-steady approximation reduces the continuity equation to

$$\frac{d}{dr} \left( r^2 \frac{dC_A}{dr} \right) = 0 \quad (2.12)$$

For a diffusion rate-limited reaction, boundary conditions for oxygen are

$$\begin{aligned} C_{O_2}(D/2) &= 0 \\ \lim_{r \rightarrow \infty} C_{O_2}(r) &= C_p \end{aligned} \quad (2.13)$$

where  $C_p$  is the emulsion-phase oxygen concentration. The oxygen concentration profile can be obtained by integrating Eq. (2.12) with boundary conditions (2.13):

$$C_{O_2}(r) = \begin{cases} C_p \left( 1 - \frac{D}{2r} \right) & \frac{D}{2} \leq r < \infty \\ 0 & r < \frac{D}{2} \end{cases} \quad (2.14)$$

Using Fick's law, this profile can be used to find the molar flux of oxygen to the particle surface:

$$\mathbf{J}_{O_2} = -D_{AB} \nabla C_{O_2} \quad (2.15)$$

Evaluating Eq. (2.15) at the particle surface, the molar rate of oxygen transfer to a particle is given by

$$\begin{aligned} n_{O_2} &= \pi D^2 D_{AB} \left. \frac{d}{dr} C_{O_2} \right|_{r=\frac{D}{2}} \\ &= 2\pi D_{AB} D C_p \end{aligned} \quad (2.16)$$

In terms of a mass transfer coefficient,  $h_m$ , the rate of oxygen transfer to the particle surface is

$$n_{O_2} = h_m \pi D^2 C_p \quad (2.17)$$

Equivalently, the mass transfer coefficient can be replaced by a Sherwood number, defined as

$$Sh = \frac{h_m D}{D_{AB}} \quad (2.18)$$

so that

$$n_{O_2} = \pi Sh D_{AB} D C_p \quad (2.19)$$

Comparing Eq. (2.16) with Eq. (2.19),  $Sh = 2$ . In practice, bed material interferes with oxygen diffusion, reducing the effective Sherwood number. As a result, theoretical correlations for the Sherwood number are often corrected to account for bed voidage. For char particles larger than the bed material, Avedesian and Davidson speculate that the Sherwood number approaches  $2\varepsilon_{mf}$ , where  $\varepsilon_{mf}$  is the emulsion phase voidage [3]. On the other hand, for particles significantly smaller than the bed material, Avedesian and Davidson suggest that interference from the sand is less important and the Sherwood number approaches 2 [3].

Using Eq. (2.19) to balance the rate of oxygen consumption with the rate of char consumption,

$$n_B = -\frac{1}{M_c} \frac{d}{dt} \left( \rho_c \frac{\pi D^3}{6} \right) = \alpha \pi D Sh D_{AB} C_p \quad (2.20)$$

where  $M_c$  is the molecular weight of carbon. Subscript  $B$  and coefficient  $\alpha$  in Eq. (2.20) depend on the surface reaction model; designations for  $B$  and  $\alpha$  are presented in Table 2.1.

Table 2.1: Variable designations for Eq. (2.20)

Surface Reaction Model	B	$\alpha$
$C + O_2 \rightarrow CO_2$	$CO_2$	1
$2C + O_2 \rightarrow 2CO$	CO	2

Assuming that a char particle burns as a constant density shrinking sphere, the time rate of change in the particle diameter can be evaluated directly from Eq. (2.20):

$$\frac{dD}{dt} = -\frac{2\alpha M_c Sh D_{AB} C_p}{\rho_c D} \quad (2.21)$$

or

$$\frac{dD}{dt} = -\frac{f}{D}, \quad f = \frac{2\alpha M_c Sh D_{AB} C_p}{\rho_c} \quad (2.22)$$

This formulation has been revised to include chemical kinetics [29] and a variable Sherwood number [24]. Chemical kinetics become significant when particles are smaller than 100  $\mu\text{m}$  [3], which is far removed from the experimental work done in this investigation on 0.8-6.0 mm particles. On the other hand, for a diffusion controlled reaction, a variable Sherwood number does not appreciably change the curvature of the impulse response. Consequently, a constant Sherwood number that characterizes the entire response is a reasonable approximation [3].

For a single particle, Eq. (2.22) can be integrated directly to find  $D(t)$ , which, in turn, can be used with Eq. (2.20) to calculate  $\text{CO}_2$  production. For an initial particle diameter  $D_o$  and volumetric air flow rate  $G$ ,

$$D(t) = \sqrt{D_o^2 - 2ft} \quad (2.23)$$

and

$$\begin{aligned} C_{\text{CO}_2}(t) &= -\frac{1}{GM_c} \frac{d}{dt} \left( \rho_c \frac{\pi D^3}{6} \right) \\ &= -\frac{1}{GM_c} \left( \rho_c \frac{\pi D^2}{2} \frac{dD}{dt} \right) \\ &= \frac{\pi \rho_c f}{2M_c G} \sqrt{D_o^2 - 2ft} \end{aligned} \quad (2.24)$$

Assuming that all the particles have the same initial diameter, the total CO<sub>2</sub> production is found by multiplying the CO<sub>2</sub> production from a single particle by the total number of particles,  $N$ . In terms of the initial char mass  $m_o$ ,  $N = 6m_o / \pi\rho_c D_o^3$  so that the total CO<sub>2</sub> production is

$$C_{\text{CO}_2}(t) = \begin{cases} \frac{3fm_o}{M_c G D_o^3} \sqrt{D_o^2 - 2ft}, & 0 \leq t \leq \frac{D_o^2}{2f} \\ 0, & \text{Otherwise} \end{cases} \quad (2.25)$$

A plot of Eq. (2.25) is presented in Fig. 2.2 for a fluidizing medium of air at 1173 K,  $D_o = 1 \text{ mm}$ ,  $m_o = 5 \text{ g}$ ,  $f = 0.01 \text{ mm}^2/\text{s}$ , and  $G = 0.13 \text{ m}^3/\text{s}$ .

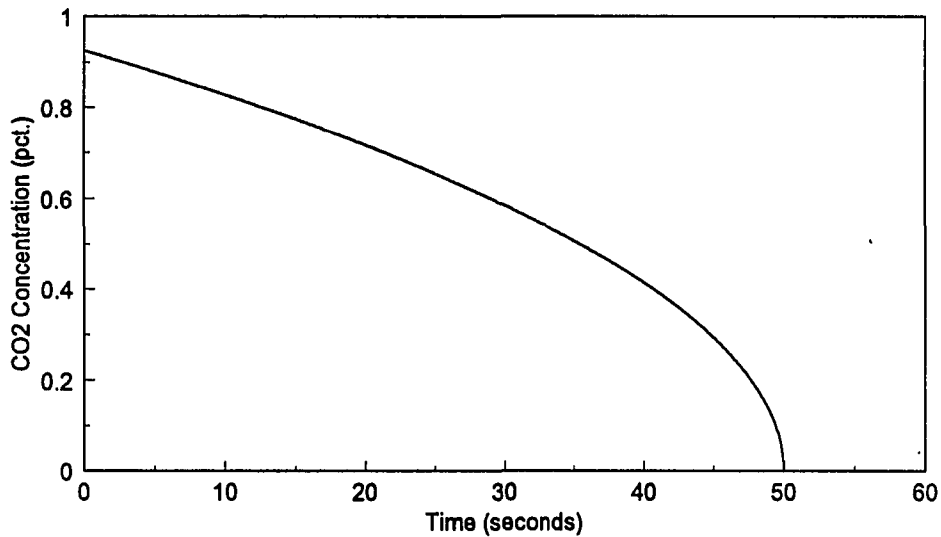


Fig. 2.2: Impulse response of a monodispersed particle distribution

### 2.3.1 The Population Balance Equation

Eq. (2.25) is limited to a strictly monodispersed coal sample. In practice, char combustion is better modeled through a mass distribution function,  $\lambda(D,t)$ . This

distribution can be integrated with respect to  $D$  to obtain the total mass of char in the bed at any time:

$$m_c(t) = \int_0^{\infty} \lambda(D,t) dD \quad (2.26)$$

A detailed description of the population balance equation is presented by Kunii and Levenspiel [22], and a partial solution for a monodispersed particle distribution is presented by van der Post et al. [38]. Following the notation of van der Post et al., a mass balance can be written for coal particles in the interval  $D$  to  $D + \Delta D$  [38]:

$$\begin{aligned} \frac{\partial}{\partial t} \left\{ \begin{array}{l} \text{coal mass in} \\ \text{the interval} \\ D \text{ to } D + \Delta D \end{array} \right\} &= \left\{ \begin{array}{l} \text{the feed rate of particles} \\ \text{into the combustor with} \\ \text{size } D \text{ to } D + \Delta D \end{array} \right\} + \left\{ \begin{array}{l} \text{the rate that particles shrink} \\ \text{into the interval } D \text{ to } D + \Delta D \\ \text{from a larger diameter} \end{array} \right\} \\ &- \left\{ \begin{array}{l} \text{the rate that particles shrink out} \\ \text{of the interval } D \text{ to } D + \Delta D \\ \text{to a smaller diameter} \end{array} \right\} - \left\{ \begin{array}{l} \text{the rate of consumption} \\ \text{within the interval } D \text{ to} \\ D + \Delta D \end{array} \right\} \end{aligned} \quad (2.27)$$

For simplicity, this formulation omits carbon loss through attrition and secondary fragmentation. By modeling burning char particles as constant density spheres whose diameters shrink at the rate  $R(D)$ , the mass balance equation becomes

$$\begin{aligned} \frac{\partial}{\partial t} \{ \lambda(D,t) \Delta D \} &= F(D,t) \Delta D - \lambda(D + \Delta D, t) R(D + \Delta D) \\ &+ \lambda(D,t) R(D) + \frac{6\lambda(D,t) \Delta D}{\pi \rho_c D^3} \cdot \frac{\pi \rho_c D^2 R(D)}{2} \end{aligned} \quad (2.28)$$

where  $F(D,t)$  is the feed rate of coal per unit size into the bed. For a diffusion rate-limited chemical reaction,  $R(D) = -f/D$ . Dividing each side by  $\Delta D$  and taking the limit as  $\Delta D \rightarrow 0$ , the population balance equation becomes

$$\frac{\partial}{\partial t} \lambda(D,t) = F(D,t) + \frac{\partial}{\partial D} \left[ \frac{f}{D} \lambda(D,t) \right] - \frac{3f}{D^2} \lambda(D,t) \quad (2.29)$$

Equivalently,

$$\frac{\partial}{\partial t} \lambda(D,t) = F(D,t) + \frac{f}{D} \frac{\partial}{\partial D} \lambda(D,t) - \frac{4f}{D^2} \lambda(D,t) \quad (2.30)$$

The total rate of char consumption is found by integrating the rate of char consumption in the interval  $D$  to  $D + \Delta D$  over all  $D$ :

$$K(t) = \int_0^{D_{\max}} \frac{3f\lambda(D,t)}{D^2} dD \quad (2.31)$$

Finally, assuming that the combustion of carbon is complete, the concentration of  $\text{CO}_2$  leaving the combustor is found by dividing the rate of char consumption by the volumetric air flow rate through the bed and by the molecular weight of carbon:

$$C_{\text{CO}_2}(t) = \frac{K(t)}{M_c G} \quad (2.32)$$

A closed-form solution of the population balance equation for a monodispersed particle distribution was originally proposed by van der Post et al. [38]. Their solution is presented in the Laplace domain and is expanded in a Laurent series. From the Laurent series expansion, they use a Pade approximation to model char combustion through a first-order, linear transfer function. However, in the time domain, their linear approximation and the analytical solution are incompatible (Fig. 2.3). As such, no physical significance can be attributed to their linear approximation. Although their analysis is flawed, it provides a useful basis for a nonlinear, time-domain solution.

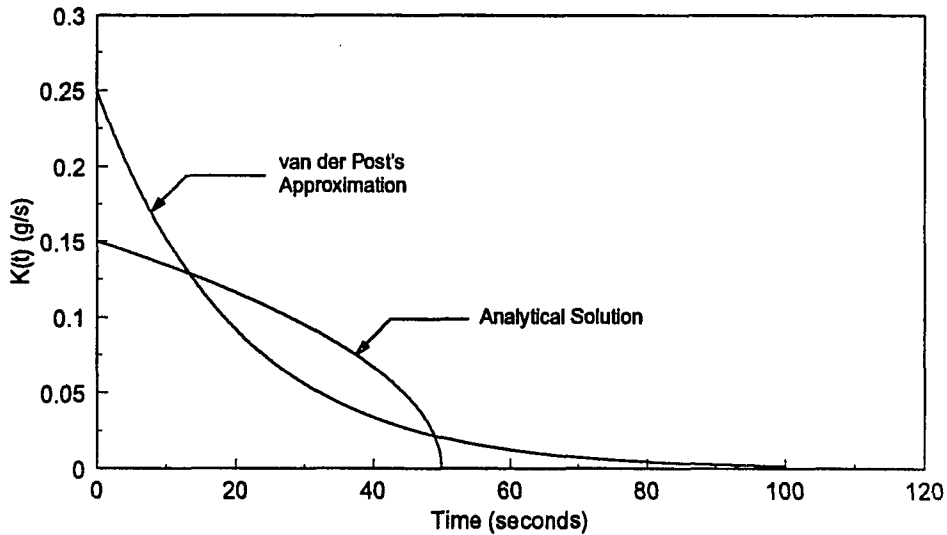


Fig. 2.3: Impulse response of van der Post's linear transfer function approximation

### 2.3.2 Impulse Response of a Monodispersed Coal Distribution

For a system initially relaxed at  $t = 0$ , the population balance equation can be transformed into the Laplace domain as

$$\frac{\partial}{\partial D} \lambda(D, s) = -\frac{D}{f} F(D, s) + \left( \frac{4}{D} + \frac{D}{f} s \right) \lambda(D, s) \quad (2.33)$$

In general,  $F(D, t)$  is the product of the coal feed rate per unit mass (1/s) and mass distribution (kg/m) such that the integral of  $F(D, t)$  with respect to  $D$  gives the total coal feed rate (kg/s). For a monodispersed sample of coal, the mass distribution is described by a Dirac delta function; in the Laplace domain,  $F(D, t)$  is

$$F(D, s) = F_o(s) \delta(D_o - D) \quad (2.34)$$

Note that the delta function argument is  $(D_o - D)$ , not  $(D - D_o)$ . This distinction is important since the integral of feed distribution with respect to  $D$  must be nonzero for  $D < D_o$  (i.e., particles shrink). Substituting Eq. (2.34) into Eq. (2.33) yields a first-order ordinary differential equation in  $D$ :

$$\frac{\partial \lambda}{\partial D} - \left( \frac{4}{D} + \frac{D}{f} s \right) \lambda = -\frac{D}{f} F_o(s) \delta(D_o - D) \quad (2.35)$$

This differential equation can be solved by multiplying both sides by the integrating factor

$$\begin{aligned} v(D,s) &= \exp \left[ - \int \left( \frac{4}{D} + \frac{D}{f} s \right) dD \right] \\ &= D^{-4} \exp(-sD^2 / 2f) \end{aligned} \quad (2.36)$$

so that

$$\lambda D^{-4} \exp(-sD^2 / 2f) = F_o(s) \frac{D_o^{-3} \exp(-sD_o^2 / 2f)}{f} h(D_o - D) \quad (2.37)$$

where  $h(\cdot)$  is a Heaviside step function. Rearranging Eq. (2.37),

$$\lambda(D,s) = \frac{F_o(s) D^4}{f D_o^3} \exp \left[ \frac{-s}{2f} (D_o^2 - D^2) \right] h(D_o - D) \quad (2.38)$$

For a unit impulse in the coal feed rate,  $F_o(s) = 1$ . Taking the inverse Laplace transform, a monodispersed particle distribution evolves through time as

$$\lambda(D,t) = \frac{D^4}{f D_o^3} \delta \left( \frac{D_o^2 - D^2}{2f} - t \right) \quad (2.39)$$

To find the CO<sub>2</sub> concentration, Eq. (2.39) can substituted into Eqs. (2.31) and (2.32) and integrated over  $0 \leq D \leq D_o$ :

$$C_{\text{CO}_2}(t) = \frac{1}{M_c G} \int_0^{D_o} \frac{3f}{D^2} \cdot \frac{D^4}{f D_o^3} \delta \left( \frac{D_o^2 - D^2}{2f} - t \right) dD \quad (2.40)$$

Making the following change of variables

$$\sigma = \frac{D_o^2 - D^2}{2f} - t \quad (2.41)$$

$$d\sigma = -\frac{D}{f} dD \quad (2.42)$$

$$D = \xi(\sigma) = \sqrt{D_o^2 - 2f\sigma - 2ft} \quad (2.43)$$

Eq. (2.40) becomes

$$C_{\text{CO}_2}(t) = \frac{1}{M_c G} \int_{-t}^{\frac{D_o^2 - t}{2f}} \frac{3f \xi(\sigma)}{D_o^3} \delta(\sigma) d\sigma \quad (2.44)$$

Evaluating the integral gives

$$C_{\text{CO}_2}(t) = \begin{cases} \frac{3f}{M_c G D_o^3} \sqrt{D_o^2 - 2ft}, & 0 \leq t \leq \frac{D_o^2}{2f} \\ 0, & \text{Otherwise} \end{cases} \quad (2.45)$$

Notice that since  $F_o(s) = 1$  in Eq. (2.38), Eq. (2.45) is consistent with Eq. (2.25) for  $m_o = 1$ .

### 2.3.3 Impulse Response of an Arbitrary Particle Distribution

Eq. (2.39) describes the impulse response for a monodispersed coal sample. This response can be generalized by integrating it over an initial particle distribution,  $\phi(D_o)$ . Consider an initial particle distribution that is nonzero over  $D_{\min} \leq D_o \leq D_{\max}$  and is zero otherwise. Multiplying Eq. (2.39) by  $\phi(D_o)$  and integrating the product over all  $D_o$  gives

$$\lambda(D, t) = \int_{-\infty}^{\infty} \phi(D_o) h(D_{\max} - D_o) h(D_o - D_{\min}) \frac{D^4}{f D_o^3} \delta\left(\frac{(D_o^2 - D^2)}{2f} - t\right) dD_o \quad (2.46)$$

Evaluating the Heaviside functions, Eq. (2.46) reduces to

$$\lambda(D,t) = \int_{D_{\min}}^{D_{\max}} \phi(D_o) \frac{D^4}{fD_o^3} \delta\left(\frac{D_o^2 - D^2}{2f} - t\right) dD_o \quad (2.47)$$

Making the following change of variables

$$\sigma = \frac{D_o^2 - D^2}{2f} - t \quad (2.48)$$

$$d\sigma = \frac{D_o}{f} dD_o \quad (2.49)$$

$$D_o = \psi(\sigma) = \sqrt{D^2 + 2f\sigma + 2ft} \quad (2.50)$$

Eq. (2.47) becomes

$$\lambda(D,\sigma) = \int_{\frac{D_{\min}^2 - D^2}{2f} - t}^{\frac{D_{\max}^2 - D^2}{2f} - t} \phi(\psi(\sigma)) \frac{D^4}{\psi(\sigma)^4} \delta(\sigma) d\sigma \quad (2.51)$$

Before integrating this equation, recall that for  $a < b$

$$\int_a^b f(x) \delta(x) dx = \begin{cases} 0, & b < 0 \\ f(0), & a < 0 < b \\ 0, & a > 0 \end{cases} \quad (2.52)$$

$$= f(0) h(b) h(-a)$$

Making the appropriate substitutions for  $\psi(0)$ , Eq. (2.51) becomes

$$\lambda(D,t) = \frac{\phi(\sqrt{D^2 + 2ft}) D^4}{(D^2 + 2ft)^2} h\left(\frac{D_{\max}^2 - D^2}{2f} - t\right) h\left(t - \frac{D_{\min}^2 - D^2}{2f}\right) \quad (2.53)$$

### 2.3.4 Char Consumption for a Block Particle Distribution

In the laboratory, "monodispersed" coal samples are formed by sieving coal particles between consecutive screen sizes. For example, coal sieved to 16 x 18 mesh has a maximum diameter of 1.18 mm and a minimum diameter of 1.00 mm. In this case,  $D_{\min} = 0.85D_{\max}$ , which suggests that the particle distribution has a significant variance. Usually, the actual particle distribution of coal collected from consecutive screen sizes is unknown. However, if the distribution is narrow, it can be approximated as a block function:

$$\phi(D_o) = \begin{cases} \phi_o, & D_{\min} \leq D_o \leq D_{\max} \\ 0, & \text{Otherwise} \end{cases} \quad (2.54)$$

where  $\phi_o$  is a constant. This distribution, in conjunction with Eq. (2.53), can be substituted into Eqs. (2.31) and (2.32) to find the rate of char consumption. For  $D_{\min} > 0$ , the Heaviside functions in Eq. (2.53) partition the impulse response into several distinct regions:

$$K(t) = \begin{cases} \frac{\int_{\sqrt{D_{\min}^2 - 2ft}}^{\sqrt{D_{\max}^2 - 2ft}} \frac{3f\lambda}{D^2} dD,}{\sqrt{D_{\min}^2 - 2ft}}, & 0 \leq t \leq \frac{D_{\min}^2}{2f} \\ \int_0^{\sqrt{D_{\max}^2 - 2ft}} \frac{3f\lambda}{D^2} dD, & \frac{D_{\min}^2}{2f} \leq t \leq \frac{D_{\max}^2}{2f} \\ 0, & \text{Otherwise} \end{cases} \quad (2.55)$$

where

$$\lambda(D,t) = \frac{\phi_o D^4}{(D^2 + 2ft)^2} \quad (2.56)$$

The solution to Eq. (2.55) is uniformly continuous in the interval  $0 \leq t \leq D_{\max}^2 / 2f$ . For  $0 \leq t \leq D_{\min}^2 / 2f$ ,

$$K(t) = \frac{3f\phi_o}{4\sqrt{ft}D_{\max}^2 D_{\min}^2} \left[ \sqrt{2}D_{\max}^2 D_{\min}^2 \tan^{-1} \left( \frac{1}{2} \sqrt{\frac{2}{ft}} \sqrt{D_{\max}^2 - 2ft} \right) - 2D_{\min}^2 \sqrt{ft} \sqrt{D_{\max}^2 - 2ft} \right. \\ \left. - \sqrt{2}D_{\max}^2 D_{\min}^2 \tan^{-1} \left( \frac{1}{2} \sqrt{\frac{2}{ft}} \sqrt{D_{\min}^2 - 2ft} \right) + 2D_{\max}^2 \sqrt{ft} \sqrt{D_{\min}^2 - 2ft} \right] \quad (2.57)$$

For  $D_{\min}^2 / 2f \leq t \leq D_{\max}^2 / 2f$ ,

$$K(t) = \frac{3f\phi_o}{4\sqrt{ft}D_{\max}^2} \left[ \sqrt{2}D_{\max}^2 \tan^{-1} \left( \frac{1}{2} \sqrt{\frac{2}{ft}} \sqrt{D_{\max}^2 - 2ft} \right) - 2\sqrt{ft} \sqrt{D_{\max}^2 - 2ft} \right] \quad (2.58)$$

And for  $t \geq D_{\max}^2 / 2f$ ,

$$K(t) = 0 \quad (2.59)$$

A typical impulse response for  $D_{\max} = 1.00$  mm,  $D_{\min} = 0.80$  mm,  $\phi_o = 25.0$  g/mm and  $f = 0.01$  mm<sup>2</sup>/s is presented in Fig. 2.4.

For reference, the limits of  $K(t)$  and its first five derivatives as time approaches zero are presented in Eqs. (2.60) through (2.65). A derivation for Eq. (2.60) is presented in Appendix A; derivations of Eqs. (2.61) through (2.65) are similar.

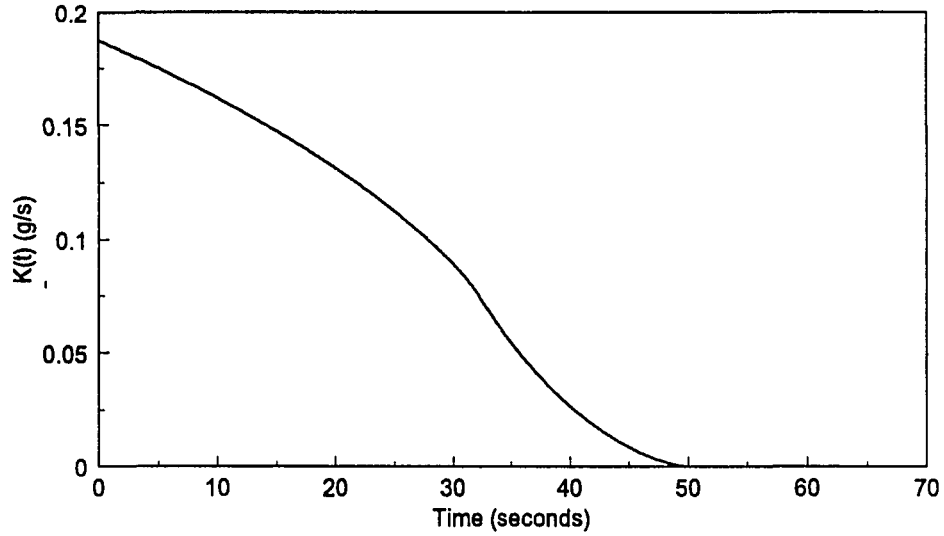


Fig. 2.4: Typical impulse response of a block particle distribution

$$\lim_{t \rightarrow 0} K(t) = 3f\phi_o \left[ \frac{1}{D_{\min}} - \frac{1}{D_{\max}} \right] \quad (2.60)$$

$$\lim_{t \rightarrow 0} K'(t) = f^2\phi_o \left[ \frac{1}{D_{\max}^3} - \frac{1}{D_{\min}^3} \right] \quad (2.61)$$

$$\lim_{t \rightarrow 0} K''(t) = \frac{3}{5}f^3\phi_o \left[ \frac{1}{D_{\max}^5} - \frac{1}{D_{\min}^5} \right] \quad (2.62)$$

$$\lim_{t \rightarrow 0} K'''(t) = \frac{9}{7}f^4\phi_o \left[ \frac{1}{D_{\max}^7} - \frac{1}{D_{\min}^7} \right] \quad (2.63)$$

$$\lim_{t \rightarrow 0} K^{(4)}(t) = 5f^5\phi_o \left[ \frac{1}{D_{\max}^9} - \frac{1}{D_{\min}^9} \right] \quad (2.64)$$

$$\lim_{t \rightarrow 0} K^{(5)}(t) = \frac{315}{11}f^6\phi_o \left[ \frac{1}{D_{\max}^{11}} - \frac{1}{D_{\min}^{11}} \right] \quad (2.65)$$

## 2.4 Refinements of the Char Combustion Model

Several refinements can be made to the combustion model. Perhaps the single most important improvement that can be made in modeling combustion dynamics is to account for variations in the emulsion-phase oxygen concentration.

When operating a fluidized bed combustor under excess air conditions, variations in the emulsion-phase oxygen concentration primarily affect char combustion dynamics. Volatile combustion dynamics are not greatly affected since most volatiles are released and burned within the freeboard. However, for char, the combustion rate coefficient is directly proportional to the emulsion-phase oxygen concentration,  $C_p$ . In turn,  $C_p$  depends on the inlet oxygen concentration,  $C_o$ , the rate of char consumption,  $K(t)$ , and the efficiency of gas exchange between the bubble-phase and the emulsion-phase. These dependencies can be found through an oxygen balance about the combustion chamber (see Fig. 2.5).

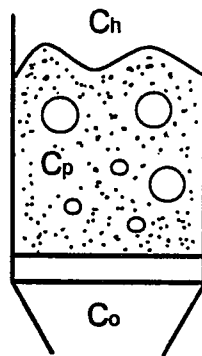


Fig. 2.5: Oxygen balance variable designations

The first step in constructing an oxygen balance is to realize that oxygen leaving the top of the bed is the aggregate of oxygen leaving the emulsion-phase and the oxygen leaving bubble-phase. Using the two-phase theory of fluidization, oxygen leaves the emulsion-phase at  $U_{mf}A_rC_p$  kmol/s. Likewise, oxygen leaves the bubble-phase at

$(U - U_{mf})A_r C_h$  kmol/s, where  $C_h$  is the concentration of oxygen inside a bubble just before it breaks through the bed surface. A separate oxygen balance around a single bubble can be used to show that [3]

$$C_h = C_p + (C_o - C_p) \exp(-X) \quad (2.66)$$

where  $X$  is a cross-flow factor, a quantity that characterizes the exchange of gas between the bubble-phase and the emulsion-phase. Details of the cross-flow factor and a derivation of Eq. (2.66) are given by Hayhurst [17]. The total  $O_2$  concentration just above the bed,  $C_{O_2}$ , is obtained by summing the contributions from the bubble-phase and the emulsion-phase:

$$C_{O_2} U A_r = (U - U_{mf}) A_r C_h + U_{mf} A_r C_p \quad (2.67)$$

Using a quasi-steady approximation,  $O_2$  consumed within the bed is the difference between the amount of oxygen entering the combustion chamber and the amount of oxygen exiting the combustion chamber:

$$\begin{aligned} r_{O_2} &= U A_r C_o - [(U - U_{mf}) A_r C_h + U_{mf} A_r C_p] \\ &= (C_o - C_p) A_r [U - (U - U_{mf}) \exp(-X)] \end{aligned} \quad (2.68)$$

With the assumption of complete combustion, oxygen consumption must balance carbon consumption; therefore,

$$(C_o - C_p) A_r [U - (U - U_{mf}) \exp(-X)] = \frac{1}{M_c} K(t) \quad (2.69)$$

so that

$$C_p = C_o - \frac{1}{M_c A_r [U - (U - U_{mf}) \exp(-X)]} K(t) \quad (2.70)$$

This equation describes a feedback loop in the combustion dynamics. A block diagram of this loop is illustrated in Fig. 2.6. Unfortunately, with this feedback loop, a closed-form

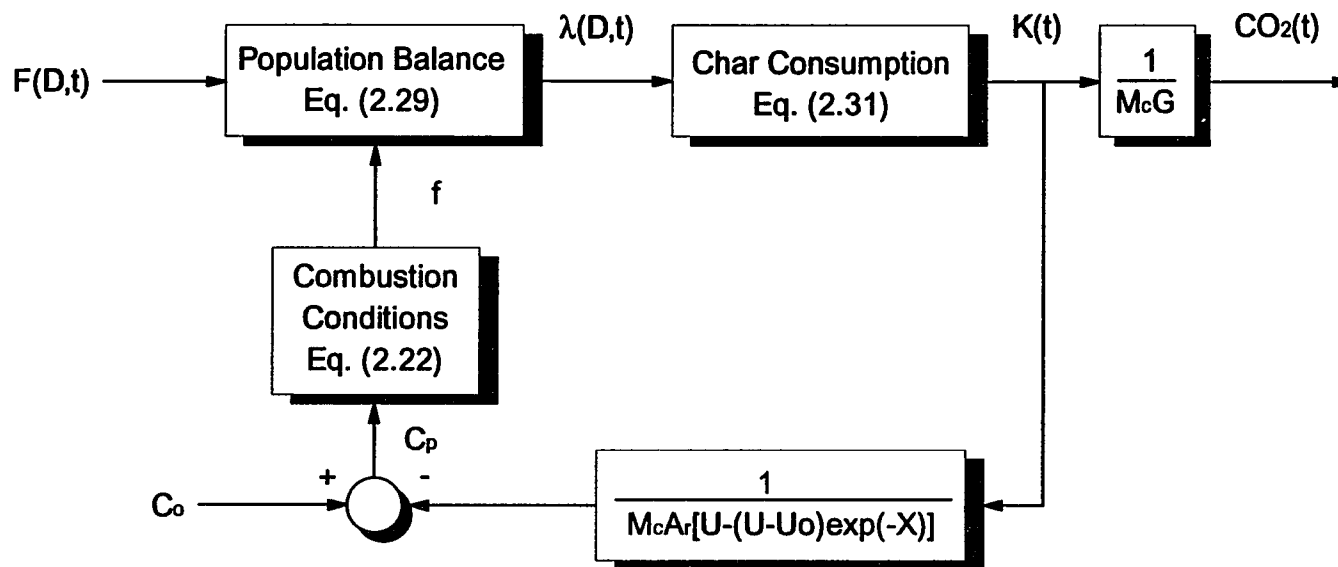


Fig. 2.6: Block diagram of the char combustion process

solution for a general particle distribution is difficult to obtain. However, a closed-form solution can be found for a monodispersed particle distribution. For a monodispersed particle distribution, Eq. (2.69) can be modified by rewriting  $K(t)$  in terms of the mass loss of a shrinking sphere:

$$(C_o - C_p)A_r Y = -\frac{N}{M_c} \frac{d}{dt} \left( \rho_c \frac{\pi D^3}{6} \right) \quad (2.71)$$

where  $N$  is the number of particles and  $Y = [U - (U - U_{mf}) \exp(-X)]$ . By modeling burning char particles as constant density shrinking spheres, Eq. (2.71) reduces to

$$C_p = C_o + \frac{N \rho_c \pi D^2}{2 M_c A_r Y} \cdot \frac{dD}{dt} \quad (2.72)$$

Recall that, for a diffusion rate limited reaction, particles shrink according to

$$\frac{dD}{dt} = -\frac{2 \alpha M_c Sh D_{AB}}{\rho_c D} C_p \quad (2.73)$$

Substituting Eq. (2.72) into Eq. (2.73) and solving for  $dD/dt$  gives

$$\frac{dD}{dt} = -\frac{2 M_c C_o}{\rho_c \left( \frac{D}{\alpha Sh D_{AB}} + \frac{N \pi D^2}{A_r Y} \right)} \quad (2.74)$$

with the initial condition  $D(0) = D_o$ . For a monodispersed particle distribution, the concentration of  $\text{CO}_2$  leaving the combustor is proportional to the total rate of change in char volume:

$$\begin{aligned} C_{\text{CO}_2}(t) &= -\frac{N}{GM_c} \frac{d}{dt} \left( \rho_c \frac{\pi D^3}{6} \right) \\ &= -\frac{N}{GM_c} \left( \rho_c \frac{\pi D^2}{2} \frac{dD}{dt} \right) \end{aligned} \quad (2.75)$$

This model can be refined further by including the effects of chemical kinetics. If chemical kinetics are infinitely fast, oxygen is consumed as soon as it reaches the particle

surface. In this case, the concentration of oxygen at the particle surface is identically zero. On the other hand, if the rate of chemical reaction is finite, the concentration of oxygen at the particle surface is also finite. Assuming that the rate of char consumption follows a first-order chemical reaction, a single particle burns according to

$$r_c = k_o \pi D^2 C_s \quad (2.76)$$

where  $C_s$  is the concentration of oxygen at the particle surface. Under quasi-steady conditions, the rate at which char is consumed must equal the rate at which oxygen diffuses to the particle surface; therefore,

$$r_c = \alpha \pi D Sh D_{AB} (C_p - C_s) \quad (2.77)$$

Eliminating the surface concentration of oxygen from these two equations gives

$$r_c = K \pi D^2 C_p \quad (2.78)$$

where

$$\frac{1}{K} = \frac{1}{k_o} + \frac{D}{\alpha Sh D_{AB}} \quad (2.79)$$

For a monodispersed distribution,

$$r_c = K \pi D^2 C_p = \frac{1}{M_c} \frac{d}{dt} \left( \rho_c \frac{\pi D^3}{6} \right) \quad (2.80)$$

so that, for constant density shrinking spheres,

$$\frac{dD}{dt} = -\frac{2M_c K}{\rho_c} C_p \quad (2.81)$$

Provided that CO oxidizes to CO<sub>2</sub> near the particle surface or within the emulsion-phase, the oxygen balance developed in Eqs. (2.66) through (2.72) is valid. Hence,  $C_p$  in Eq.

(2.81) can be replaced by Eq. (2.72) so that

$$\frac{dD}{dt} = -\frac{2M_c C_o}{\rho_c \left( \frac{1}{K} + \frac{N\pi D^2}{A_r Y} \right)} \quad (2.82)$$

For a fast surface reaction,  $k_o \rightarrow \infty$ ,  $K \rightarrow \alpha Sh D_{AB}/D$ , and Eq. (2.82) collapses into Eq. (2.74).

Incorporating a variable emulsion-phase oxygen concentration or chemical kinetics in the char combustion model will slightly alter the curvature of the impulse response. Fortunately, for small batches of coal, the entire char combustion response can be adequately approximated as a diffusion rate-limited process. However, the influences of a variable emulsion-phase oxygen concentration and chemical kinetics cannot be ignored. Hence, by modeling the entire response as a diffusion rate-limited process, the combustion rate coefficient must be interpreted as a characteristic constant that embodies these influences.

The effects of the emulsion-phase oxygen concentration and chemical kinetics on the impulse response are illustrated in Figs. 2.7 through 2.9. In all cases, theoretical responses are presented for strictly monodispersed particle distributions. Combustion models are summarized in Table 2.2; physical parameters used to calculate the transient responses are outlined in Table 2.3. These parameters were chosen to closely approximate the experimental conditions in this investigation.

Although the details of these transient responses are different, these responses share the same curvature characteristics. There are some differences in the curvatures; however, these differences will not greatly influence the impulse response of a general particle distribution since these differences become less pronounced when they are integrated over the initial distribution. Therefore, independent of the model basis, char combustion can be approximated by an appropriately scaled, diffusion rate-limited model.

Table 2.2: Summary of impulse response models

	Diffusion	Variable $C_p$	Chemical Kinetics	Governing Equation
Fig. 2.7	✓			Eq. (2.22)
Fig. 2.8	✓	✓		Eq. (2.74)
Fig. 2.9	✓	✓	✓	Eq. (2.82)

Table 2.3: Coal combustion model parameters

<b>Sand:</b>	
Density	$\rho_s = 2650 \text{ kg/m}^3$
Mean particle diameter	$D_s = 0.55 \text{ mm}$
<b>Bed:</b>	
Fluidizing medium	Air
Cross-sectional area <sup>a</sup>	$A_r = 0.013 \text{ m}^2$
Operating temperature	$T = 1173 \text{ K}$
Superficial velocity	$U = 1 \text{ m/s}$
Minimum fluidization velocity	$U_{mf} = 0.110 \text{ m/s}$
Inlet oxygen concentration	$C_o = 7.17 \times 10^{-4} \text{ kmol/m}^3$
<b>Fuel:</b>	
Type	Char
Density	$\rho_c = 720 \text{ kg/m}^3$
Mean initial diameter	$D_o = 1.55 \text{ mm}$
Mass of fuel charge	$m_o = 1.0 \text{ g}$
<b>Physical Properties:</b>	
Surface reaction model	$\text{C} + \text{O}_2 \rightarrow \text{CO}_2$
Diffusion coefficient <sup>b</sup>	$D_{AB} = 208 \text{ mm/s}$
Chemical reaction rate <sup>c</sup>	$k_o = 4065 \text{ mm/s}$
Cross-flow factor <sup>d</sup>	$X = 2$
Sherwood number <sup>e</sup>	$Sh = 3.5$

<sup>a</sup> Since batches of particles tend to cluster together, the effective cross sectional area was estimated to be one-tenth of the actual cross sectional bed area.

<sup>b</sup> From Ross and Davidson [29].

<sup>c</sup> Estimated from Fig. 19.50 in Essenhigh [11, p. 1273].

<sup>d</sup> From Ross and Davidson [29].

<sup>e</sup> From La Nauze [24].

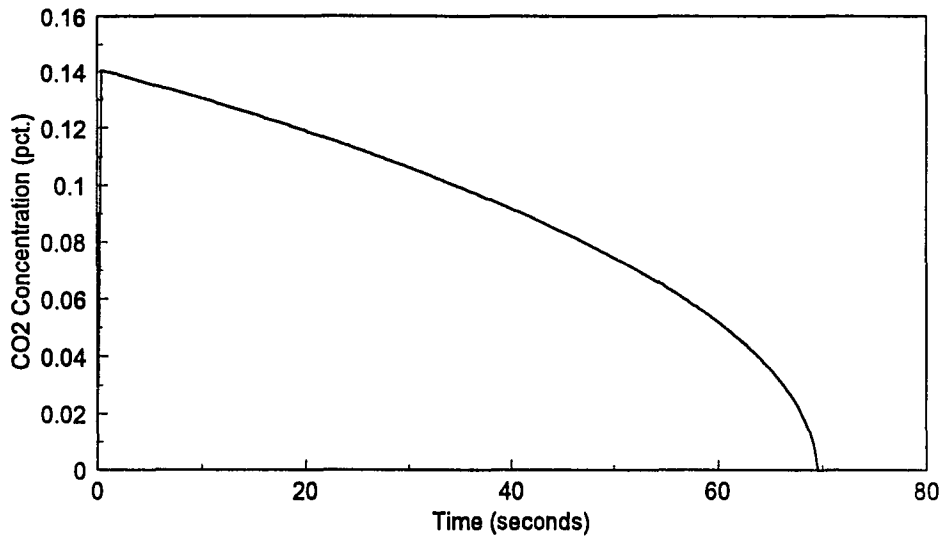


Fig. 2.7: Combustion model No. 1

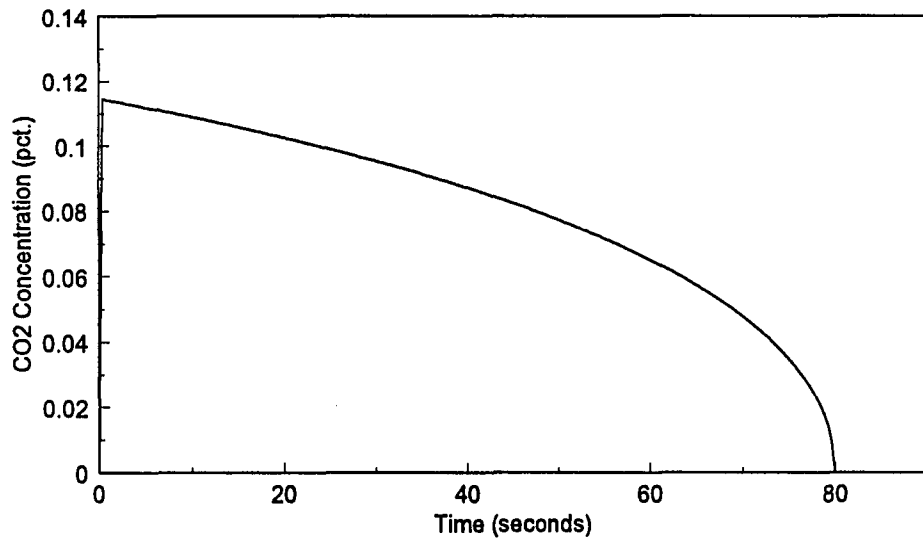


Fig. 2.8: Combustion model No. 2

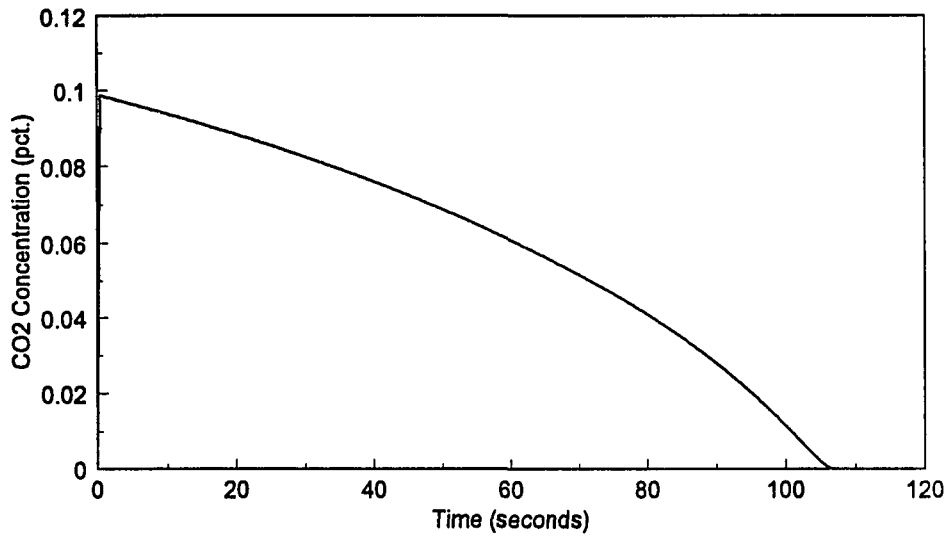


Fig. 2.9: Combustion model No. 3

### 3. LINEAR SYSTEM IDENTIFICATION THEORY

One difficulty often encountered with chemical and thermodynamic processes is measurement noise. Measurement noise can be attributed to random electrical fluctuations in transducers, random fluctuations associated with turbulent flow, or inhomogeneities in the process itself. In many cases, measurement noise can be modeled as an uncorrelated, zero-mean, additive random variable.

Because measurement noise is ubiquitous, special attention must be given to its effect on system identification algorithms. This chapter reviews several system identification schemes used to estimate system dynamics in the presence of noise. The literature review is divided into the following sections: (1) discrete-time system identification, (2) frequency domain system identification, and (3) continuous-time system identification. Although this literature review is not exhaustive, it does present some of the better known algorithms.

#### 3.1 Discrete-Time System Identification

In the discrete-time domain, systems are described through a shift operator representation. The forward-shift operator is denoted by  $q$ , the backward-shift operator by  $q^{-1}$ . For a sequence  $y(k)$ , where  $k \in \{\dots, -1, 0, 1, 2, \dots\}$ ,  $qy(k)$  references the sequence at index  $(k + 1)$ . In a similar manner,  $q^{-1}y(k)$  references the sequence at index  $(k - 1)$ . In general,

$$\begin{aligned} q^i y(k) &= y(k+i) \\ q^{-i} y(k) &= y(k-i) \end{aligned} \quad (3.1)$$

In terms of addition and multiplication, the shift operator, with constant coefficients, satisfies all the algebraic laws of polynomials. Formally, transfer functions are written in terms of the z-transform. The distinction is that  $q$  is an operator whereas  $z$  is a complex variable. Details concerning this distinction can be found in Oppenheim and Schaffer [27] and Astrom and Wittenmark [2].

Using backward-shift operator representation, linear systems are modeled through linear combinations of past outputs,  $y(k)$ , and past inputs,  $u(k)$ . Following the notation of Goodwin and Sin [14], linear systems are expressed in the discrete-time domain as

$$A(q^{-1})y(k) = B(q^{-1})u(k) \quad (3.2)$$

where  $A$  and  $B$  are the scalar polynomials

$$\begin{aligned} A(q^{-1}) &= 1 + a_1 q^{-1} + a_2 q^{-2} + \dots + a_n q^{-n} \\ B(q^{-1}) &= b_0 + b_1 q^{-1} + b_2 q^{-2} + \dots + b_m q^{-m} \end{aligned} \quad (3.3)$$

In Eq. (3.2), previous values of  $y$  are designated autoregressive (AR) components and values for  $u$  are designated exogenous (X) components. The complete, deterministic model is abbreviated ARX. In many references (e.g., [2,14]), previous values of  $u$  are designated moving average (MA) components. In this case, the complete model is sometimes abbreviated DARMA, where the qualifier "deterministic" (D) has been introduced to suggest an input signal that is not a white noise process.

The deterministic system in Eq. (3.2) can be extended by incorporating stochastic components in the model structure, which are often idealized as additive inputs to the deterministic system. That is,

$$\begin{aligned} A(q^{-1})y(k) &= B(q^{-1})u(k) + C(q^{-1})e(k) \\ z(k) &= y(k) + w(k) \end{aligned} \quad (3.4)$$

where  $e(k)$  models process noise,  $w(k)$  models measurement noise, and

$$C(q^{-1}) = 1 + c_1q^{-1} + c_2q^{-2} + \dots + c_lq^{-l} \quad (3.5)$$

In this model, values of  $e$  are designated MA components, and the entire stochastic model is abbreviated ARMAX.

Additional considerations concerning stochastic modeling, including discussions pertaining to innovations modeling, are presented by Astrom and Wittenmark [2] and Goodwin and Sin [14].

### 3.1.1 Least-Squares Parameter Estimation

In the discrete-time domain, parameters are regularly estimated through least-squares techniques. For time series, least-squares identification algorithms yield unbiased results provided the system can be described by the model

$$A(q^{-1})y(k) = B(q^{-1})u(k) + e(k) \quad (3.6)$$

where  $e(k)$  is an uncorrelated, zero-mean residual. In terms of the fluidized bed system,  $y(k)$  is a deviation from steady-state conditions in  $\text{CO}_2$  concentration, and  $u(k)$  is a deviation from steady-state conditions in the feed rate of coal. To simplify notation, subsequent developments will be made for a second-order model; extensions to higher-order models are straightforward. As a second-order model, Eq. (3.6) can be expanded and rearranged in the following manner:

$$y(k) = -a_1y(k-1) - a_2y(k-2) + b_1u(k-1) + b_2u(k-2) + e(k) \quad (3.7)$$

The method of least-squares is built upon dividing the ARX model between variates and coefficients such that

$$y(k) = \phi(k-1)^T \theta + e(k) \quad (3.8)$$

where

$$\phi(k-1)^T = [-y(k-1), -y(k-2), u(k-1), u(k-2)] \quad (3.9)$$

and

$$\theta = [a_1, a_2, b_1, b_2]^T \quad (3.10)$$

In keeping with the notation presented by Astrom and Wittenmark [2] and Goodwin and Sin [14],  $\phi$  has been indexed with respect to  $y(k-1)$ , which is the most recent value in the data vector. Accordingly, for  $k$  observations, the ARX model may be collectively written as

$$\begin{bmatrix} y(1) \\ y(2) \\ y(3) \\ \vdots \\ y(k) \end{bmatrix} = \begin{bmatrix} \phi(0)^T \\ \phi(1)^T \\ \phi(2)^T \\ \vdots \\ \phi(k-1)^T \end{bmatrix} \begin{bmatrix} a_1 \\ a_2 \\ b_1 \\ b_2 \end{bmatrix} + \begin{bmatrix} e(1) \\ e(2) \\ e(3) \\ \vdots \\ e(k) \end{bmatrix} \quad (3.11)$$

In vector-matrix notation,  $\mathbf{Y} = \Phi\theta + \mathbf{e}$ , where  $\Phi$  is called the "model matrix" and  $\mathbf{e}$  is a column vector of residuals. The best estimate of  $\theta$  (in a least-squares sense) is found by minimizing the residual sum square error,  $\mathbf{J}$ , where

$$\mathbf{J} = \mathbf{e}\mathbf{e}^T \quad (3.12)$$

The minimal of  $\mathbf{J}$  is found through an elementary application of matrix calculus from which the normal equations

$$\Phi^T\Phi\hat{\theta} = \Phi^T\mathbf{Y} \quad (3.13)$$

are obtained. Provided that the positive semidefinite matrix  $\Phi^T\Phi$  is nonsingular, the solution to Eq. (3.13) is

$$\hat{\theta} = [\Phi^T\Phi]^{-1}\Phi^T\mathbf{Y} \quad (3.14)$$

Of particular interest is the relationship between  $[\Phi^T \Phi]^{-1}$  and the parameter vector  $\theta$ . On the assumption that residuals are independently distributed about a mean of zero and a variance of  $\sigma^2$ , the following covariance relation holds:

$$E\{[\theta - \hat{\theta}][\theta - \hat{\theta}]^T\} = \sigma^2 [\Phi^T \Phi]^{-1} \quad (3.15)$$

Additional considerations concerning the covariance matrix along with its derivation are presented by Cox [9].

When estimating parameters on-line, large quantities of data are recorded, and sequential calculations for  $[\Phi^T \Phi]^{-1}$  become prohibitively cumbersome. Consequently, to reduce computation time, standard least-squares are expressed recursively so that new estimates for  $\theta$  and  $[\Phi^T \Phi]^{-1}$  are obtained from old results, corrected for new data. For a single-input, single-output model, least-squares parameter estimates are calculated through the following sequential equations [14]:

$$\hat{\theta}(k) = \hat{\theta}(k-1) + \mathbf{P}(k-1)\phi(k-1)[y(k) - \hat{y}(k)] \quad (3.16)$$

where

$$\mathbf{P}(k-1) = \mathbf{P}(k-2) - \frac{\mathbf{P}(k-2)\phi(k-1)\phi(k-1)^T \mathbf{P}(k-2)}{1 + \phi(k-1)^T \mathbf{P}(k-2)\phi(k-1)} \quad (3.17)$$

and

$$\hat{y}(k) = \phi(k-1)^T \hat{\theta}(k-1) \quad (3.18)$$

For brevity, the covariance matrix  $[\Phi^T \Phi]^{-1}$  is abbreviated by  $\mathbf{P}$ , where  $\mathbf{P}$  has been indexed with respect to the most recent data set,  $\phi(k-1)$ . This algorithm is initialized with  $\hat{\theta}(0) = 0$  and  $\mathbf{P}(-1) = \sigma^2 \mathbf{I}$ , where  $\sigma^2$  is a sufficiently large, positive constant.

A block diagram of an unbiased standard least squares model is depicted in Fig. 3.1. Note that this model is restricted to additive noise shaped by the transfer function

$1/A(z^{-1})$ , which is often an unrealistic assumption. If measurement noise deviates from this model, biased estimates are obtained. Improvements can be made by modeling stochastic components and estimating their parameters through modified least-squares algorithms, such as extended least-squares.

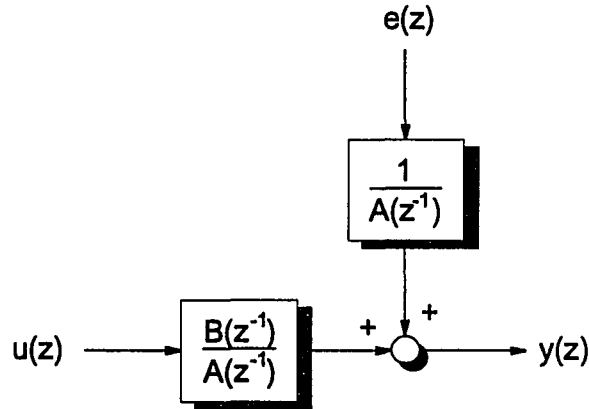


Fig. 3.1: Unbiased least-squares model

### 3.1.2 Extended Least-Squares Parameter Estimation

The extended least-squares (ELS) method, also known as pseudo linear regression, is used to find parameters of the ARMAX model

$$A(q^{-1})y(k) = B(q^{-1})u(k) + C(q^{-1})e(k) \quad (3.19)$$

where  $\{e(k)\}$  is uncorrelated white noise. This model is illustrated in block diagram form in Fig. 3.2.

If no stochastic process disturbances are present, measurement noise can be modeled with  $C(q^{-1}) = A(q^{-1})$ . As with the standard least-squares model, Eq. (3.19) can be expanded and rearranged as

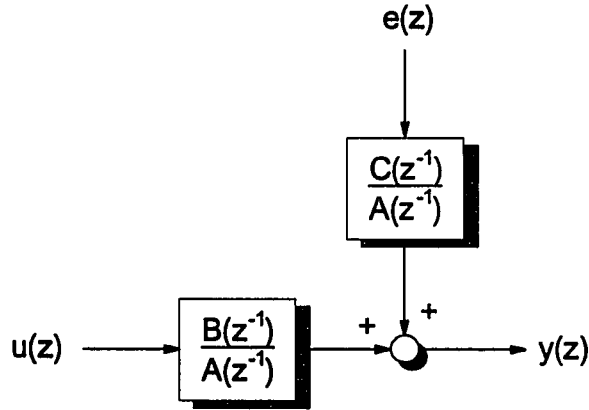


Fig. 3.2: Unbiased extended least-squares model

$$y(k) = -a_1y(k-1) - a_2y(k-2) + b_1u(k-1) + b_2u(k-2) + c_1e(k-1) + c_2e(k-2) + e(k) \quad (3.20)$$

The difficulty with this ARMAX model is that the sequence  $\{e(k)\}$  is not known nor is it directly measurable. However, a regression model can be obtained if  $e(k)$  is approximated by  $\varepsilon(k)$ , where

$$\varepsilon(k) = y(k) - \hat{y}(k) \quad (3.21)$$

In terms of the estimated partial regression vector,

$$\varepsilon(k) = y(k) - \phi(k-1)^T \hat{\theta}(k-1) \quad (3.22)$$

where

$$\phi(k-1)^T = [-y(k-1), -y(k-2), u(k-1), u(k-2), \varepsilon(k-1), \varepsilon(k-2)] \quad (3.23)$$

and

$$\theta = [a_1, a_2, b_1, b_2, c_1, c_2]^T \quad (3.24)$$

By estimating the error residual in this manner, parameters of the ARMAX model can be estimated through standard recursive least-squares (Eqs. (3.16) through (3.18)).

Performance of the ELS algorithm can be improved slightly by updating the error prediction in Eq. (3.22) with an a posteriori prediction:

$$\bar{\varepsilon}(k) = y(k) - \phi(k-1)^T \hat{\theta}(k) \quad (3.25)$$

Convergence properties of the ELS method are given by Goodwin and Sin [14] and Ljung and Soderstrom [25]. In short, estimated parameters will converge to actual system parameters provided the following conditions are met [14]:

- 1) The model order is known exactly
- 2) The polynomials  $A(z^{-1})$  and  $C(z^{-1})$  are stable
- 3) The input signal is persistently exciting
- 4) The data are mean-square bounded

Although convergence analysis is comforting, in practice, unbiased parameter estimates are difficult to obtain when signals are corrupted with measurement noise. As an example, consider the transfer function

$$\frac{y(s)}{u(s)} = \frac{3.5}{s^2 + 3s + 3.5} \quad (3.26)$$

With a 15 Hz sampling frequency and a zero-order hold, the discrete-time representation of this transfer function is

$$\frac{y(z)}{u(z)} = \frac{10^{-3}(7.2749z + 6.8056)}{z^2 - 1.8047z + 0.8187} \quad (3.27)$$

Measurement noise can be simulated by corrupting the output signal with an additive random variable. Defining  $y_m(k)$  as the measured output signal,

$$y_m(k) = y(k) + n(k) \quad n(k) \sim N(0, \sigma^2) \quad (3.28)$$

Parameters of the discrete-time transfer function were estimated through the ELS algorithm with a posteriori predictions; a Matlab macro of the ELS algorithm is presented in Appendix B. For this example, input signals were generated from a zero-mean, unity-variance Gaussian-random sequence. As a simplification, input signals were free of measurement noise. Defining the noise-to-signal (NSR) ratio as the ratio of measurement noise variance to uncorrupted output variance, Table 3.1 lists estimated coefficients of Eq. (3.27) for various NSRs. Note that the performance of the ELS algorithm degrades significantly as the NSR increases modestly.

Table 3.1: Performance of the ELS algorithm

	$a_1$	$a_2$	$b_1$	$b_2$
True	-1.8047	0.8187	0.0073	0.0068
Initial Est.	0.0000	0.0000	0.0000	0.0000
NSR				
0%	-1.7946	0.8086	0.0073	0.0069
1%	-1.6908	0.7066	0.0088	0.0082
2%	-1.5252	0.5444	0.0095	0.0096
3%	-1.4003	0.4220	0.0101	0.0107
4%	-1.3021	0.3259	0.0107	0.0117
5%	-1.2209	0.2465	0.0111	0.0126

Because estimated system coefficients deviate from actual values at low noise levels, the utility of the ELS algorithm is dubious. The difficulty with the ELS algorithm, as with most least-squares algorithms, lies within the nature of the ARMAX model. Traditionally, stochastic signals are characterized by a noise-to-signal ratio, which is a

time-averaged quantity. However, an ARMAX model is defined within a relatively narrow time interval. For example, the data vector for Eq. (3.27) only contains the elements  $y(k-1)$  and  $y(k-2)$ . To get accurate coefficient estimates,  $y(k)$ ,  $y(k-1)$ , and  $y(k-2)$  must be sufficiently distinguishable relative to the measurement noise within that interval. In other words, although noise-to-signal ratio may be low, the output signal within a small interval can be dominated by measurement noise, making parameter estimation difficult.

One solution to this difficulty is to increase the sampling interval so that changes in  $y(k)$ ,  $y(k-1)$ , and  $y(k-2)$  are large when compared with measurement noise within that interval. However, by increasing the sampling interval, fast system dynamics become difficult to estimate. Alternatively, data can be digitally filtered before being processed by the least-squares algorithm. With this approach, data vector  $\psi(k-1)$  is formed by filtering input and output signals with the fixed AR filter

$$D(q^{-1}) = 1 + d_1 q^{-1} + \dots + d_p q^{-p} \quad (3.29)$$

so that

$$D(q^{-1})y_F(k) = y(k) \quad (3.30)$$

and

$$D(q^{-1})u_F(k) = u(k) \quad (3.31)$$

where  $y_F(k)$  denotes the filtered output signal, and  $u_F(k)$  denotes the filtered input signal. Note that both the input signal and the output signal are processed through the same fixed filter. This procedure prevents the least-squares algorithm from converging to filter coefficients. That is, for the nominal transfer function  $B(z^{-1})/A(z^{-1})$ , the filtered transfer function reduces to

$$\frac{y_F(z)}{u_F(z)} = \frac{D(z^{-1})B(z^{-1})}{D(z^{-1})A(z^{-1})} = \frac{B(z^{-1})}{A(z^{-1})} \quad (3.32)$$

Using filtered data, the output error is redefined as

$$\eta(k) = y_F(k) - \hat{y}_F(k) \quad (3.33)$$

where

$$\hat{y}_F(k) = \psi(k-1)^T \hat{\theta}(k-1) \quad (3.34)$$

$$\psi(k-1) = [-y_F(k-1), -y_F(k-1), u_F(k-1), u_F(k-1), \eta(k-1), \eta(k-2)] \quad (3.35)$$

and

$$\theta = [a_1, a_2, b_1, b_2, c'_1, c'_2]^T \quad (3.36)$$

For a single-input, single-output model, least-squares parameter estimates are calculated through the following sequential equations (cf. Eqs. (3.16) through (3.18)):

$$\hat{\theta}(k) = \hat{\theta}(k-1) + \mathbf{P}(k-1)\psi(k-1)\eta(k) \quad (3.37)$$

where

$$\eta(k) = y_F(k) - \hat{y}_F(k) \quad (3.38)$$

$$\mathbf{P}(k-1) = \mathbf{P}(k-2) - \frac{\mathbf{P}(k-2)\psi(k-1)\psi(k-1)^T\mathbf{P}(k-2)}{1 + \psi(k-1)^T\mathbf{P}(k-2)\psi(k-1)} \quad (3.40)$$

As with the standard ELS algorithm, performance can be improved by replacing  $\eta(k)$  with an a posteriori prediction error:

$$\bar{\eta}(k) = y_F(k) - \psi(k-1)^T \hat{\theta}(k) \quad (3.41)$$

This algorithm differs slightly from that presented by Goodwin and Sin [14]. Their algorithm uses a fixed filter based on an initial estimate of  $C(q^{-1})$ . However, if a good estimate of  $C(q^{-1})$  is available, there is little reason to use an extended least-squares algorithm. In any case, a digital filter only marginally addresses the difficulties associated with measurement noise dominating signals within a narrow time interval.

### 3.1.3 Remarks on Discrete-Time System Identification

In recent years, with the advent of inexpensive computing power, much work has been done to further the study of discrete-time identification algorithms. Today, system parameters are routinely estimated through standard least-squares, extended least-squares, generalized least-squares, instrument variable, and recursive maximum likelihood methods [19,25]. However, many applications, especially those in the process industries, are inherently continuous-time systems. In many of these cases, continuous-time parameter estimates are more meaningful when characterizing system dynamics. These parameters can be indirectly estimated by transforming the discrete-time transfer function into the continuous-time domain. Equivalent continuous-time transfer functions can be estimated from discrete-time transfer functions using Tustin's approximation, which is a bilinear transformation between the variables  $z$  and  $s$ . With Tustin's approximation, the discrete-time transform variable  $z$  maps onto the continuous-time transform variable  $s$  as

$$s = \frac{2(z-1)}{T(z+1)} \quad (3.42)$$

where  $T$  is the sampling interval. Therefore, an equivalent continuous-time transfer function can be found by replacing the argument of  $H(z^{-1})$  with  $s$  as defined in Eq. (3.42). Other approximations, such as the forward difference method, backward difference method, and step invariance method, are not suitable since they produce unnecessarily poor estimates of continuous-time transfer functions [2]. Unfortunately, even with Tustin's approximation, the inverse transform from the discrete-time domain to the continuous-time domain is ill conditioned, resulting in poor estimates of continuous-time system dynamics [37]. Hence, even if digital techniques were insensitive to

measurement noise, finding an equivalent continuous-time transfer function would be difficult.

### 3.2 Frequency Domain System Identification

Some of the difficulties associated with discrete-time system identification can be overcome by analyzing the frequency content of a signal. With the development of the fast Fourier transform (FFT), frequency analysis has become a powerful and manageable tool for characterizing system dynamics.

Spectral estimation techniques are classified as either parametric or nonparametric. With parametric methods, the spectral content of a signal is obtained by estimating parameters of a process model and then transforming that process model into the frequency domain. Some common parametric techniques include the autocorrelation method, the modified covariance method, the maximum entropy method, and Prony's method.

In contrast with parametric methods, nonparametric approaches are used to estimate the spectral content of a signal without a priori knowledge of the model structure. Some common nonparametric approaches include periodogram spectral estimation and minimum variance spectral estimation.

In this section, discussions of parametric and nonparametric methods will be restricted to real data sets; extensions to complex data sets are straightforward. More importantly, process signals are assumed to be stationary. A stationary process is one in which the stochastic elements have probability density functions that do not vary with time. In practice, this is not a serious restriction. In addition, process signals are assumed to be ergodic. An ergodic signal is one in which the statistical measures of the ensemble are

equivalent to the time-averaged measures of an individual realization. Details of stochastic signal classifications can be found in Brown [6], Helstrom [18], and Kay [21].

Spectral analysis is based on the analysis of correlation functions. For a zero-mean, stationary process, the autocorrelation function of a signal  $y(t)$  is defined as

$$R_{yy}(\tau) = E[y(t)y(t + \tau)] \quad (3.43)$$

where  $E$  is the expectation operator, which is referenced with respect to the ensemble, not an individual realization. The Fourier transform of the autocorrelation function is defined as the power spectral density function:

$$S_{yy}(i\omega) = F[R_{yy}(\tau)] = \int_{-\infty}^{\infty} R_{yy}(\tau) \exp(-i\omega\tau) d\tau \quad (3.44)$$

For a finite data set, the power spectral density function cannot be calculated directly from Eq. (3.44) since this equation requires knowledge of the autocorrelation function for all  $\tau \in (-\infty, \infty)$ . Consequently, spectral estimation is an exercise in estimating – either directly or indirectly – correlation functions from finite sets of data.

### 3.2.1 Nonparametric Spectral Estimation Methods

Nonparametric spectral estimation methods, such as classical Fourier analysis, have distinct advantages over many other system identification techniques. Chief among these, Fourier analysis is nonparametric; therefore, in contrast with many identification schemes, this approach is not sensitive to model order. However, care must be exercised when using Fourier techniques, especially when analyzing process signals that are corrupted by measurement noise. For example, although Fourier techniques are asymptotically unbiased, they are inconsistent, a characteristic that must be taken into account when synthesizing transfer functions from frequency data.

To calculate the power spectral density function, the autocorrelation function of the ensemble must be known a priori. However, if the process is ergodic, the autocorrelation function can be estimated from time-averaged realizations. In other words, if a signal is ergodic, the expectation operator in Eq. (3.44) can be replaced by the following time-averaged function:

$$R_{yy}(\tau) = \lim_{T \rightarrow \infty} \frac{1}{T} \int_0^T y(t)y(t+\tau)dt \quad (3.45)$$

This equation provides the basis for Eq. (3.46), which relates the power spectral density function to the Fourier transform of a single data set [6,18]:

$$S_{yy}(i\omega) = \int_{-\infty}^{\infty} R_{yy}(\tau) \exp(-i\omega\tau) d\tau = \lim_{T \rightarrow \infty} E \left[ \frac{1}{T} |F[y(t)]|^2 \right] \quad (3.46)$$

where the quantity

$$\frac{1}{T} |F[y(t)]|^2 \quad (3.47)$$

is known as the periodogram. In words, the mean periodogram is equivalent to the power spectral density function. In a similar fashion, this relation can be used to find the power and cross-power spectral density functions of the linear system defined in Fig. 3.3 [18,20]:

$$S_{uu}(i\omega) = \lim_{T \rightarrow \infty} E \left[ \frac{1}{T} U^*(i\omega)U(i\omega) \right] \quad (3.48)$$

$$S_{uy}(i\omega) = \lim_{T \rightarrow \infty} E \left[ \frac{1}{T} U^*(i\omega)Y(i\omega) \right] \quad (3.49)$$

where  $U(i\omega) = F[u(t)]$  and  $Y(i\omega) = F[y(t)]$ .

In practice, data are collected during a finite time interval; therefore, the Fourier transforms of  $u(t)$  and  $y(t)$  must be estimated from a truncated Fourier integral. For example, the Fourier transform of  $y(t)$  defined over  $[0, T]$  can be approximated as

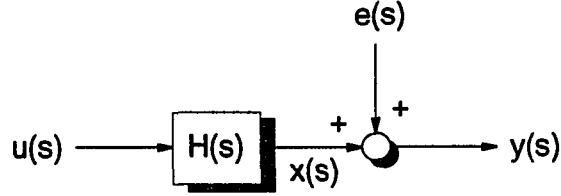


Fig. 3.3: Block diagram of the system to be identified

$$F[y(t)] \approx \int_0^T y(t) \exp(-i\omega t) dt \quad (3.50)$$

In many cases, a continuous data stream is not available; instead, signals are sampled at discrete time intervals. Therefore, for  $N$  evenly-spaced samples,  $\{y_0, y_1, \dots, y_{N-1}\}$ , Eq.

(3.50) can be approximated by the Riemann sum

$$Y(in\omega_o) = \sum_{k=0}^{N-1} y_k \exp(-in\omega_o k \Delta t) \Delta t, \quad n = -\frac{N}{2}, \dots, \frac{N}{2} \quad (3.51)$$

where  $\omega_o = 2\pi/T$ . The discrete Fourier transform of  $y(t)$  is found by eliminating  $\omega_o$  from the summation, i.e.,

$$Y(in\omega_o) = \Delta t \sum_{k=0}^{N-1} y_k \exp(-i2\pi kn / N) \quad (3.52)$$

For large data sets, the summation in this equation can be calculated efficiently with the Fast Fourier Transform (FFT) algorithm. Once the discrete Fourier transform has been calculated, it can be used to generate a periodogram; that is,

$$\hat{S}_{yy}(i\omega) = \frac{1}{N\Delta t} \left| \Delta t \sum_{k=0}^{N-1} y_k \exp(-i2\pi kn / N) \right|^2 \quad (3.53)$$

Unfortunately, the variance of a periodogram is as large as its mean [21]. Moreover, the variance is independent of  $N$ ; therefore, increasing the sample size will not decrease the variance. Although the variance cannot be reduced by increasing the sample size, the variance can be reduced by averaging several periodograms. Alternatively, a smooth estimate can be obtained by low-pass filtering the periodogram with the FFT algorithm. Details of smoothed spectral estimators are presented by Helstrom [18] and Jenkins and Watts [20].

From the estimates of the cross-power and power spectral density functions, a frequency response plot of the system transfer function can be generated. For the linear system in Fig 3.3, the spectral density functions  $S_{yy}(i\omega)$  and  $S_{uu}(i\omega)$  are related by the ratio [20,21]

$$\frac{S_{yy}(i\omega)}{S_{uu}(i\omega)} = H(i\omega) \quad (3.54)$$

Using the relation in Eq. (3.46), the spectral density functions in Eq. (3.54) can be estimated with discrete Fourier transforms of the input and output data sets. Many authors ignore the expectation operator in Eq. (3.46) (e.g., [8,15,16]) and reduce Eq. (3.54) to the following form:

$$\frac{U^*(i\omega)Y(i\omega)}{U^*(i\omega)U(i\omega)} = \frac{Y(i\omega)}{U(i\omega)} = H(i\omega) \quad (3.55)$$

For deterministic signals, the expectation operator can be ignored. However, the expectation operator cannot be ignored when signals contain stochastic components. Without the expectation operator, the ratio in Eq. (3.55) will not converge to any meaningful quantity [20,26].

An alternative approach to estimating the frequency response of a system takes advantage of the relationship between the input and the output power spectral density

functions. For the linear system in Fig. 3.3, the spectral density function  $S_{xx}(i\omega)$  is related to  $S_{uu}(i\omega)$  by [20,21]

$$S_{xx}(i\omega) = |H(i\omega)|^2 S_{uu}(i\omega) \quad (3.56)$$

Furthermore, since  $S_{yy}(i\omega) = S_{xx}(i\omega) + S_{ee}(i\omega)$  [20,21], the spectral density function of  $y(t)$  is

$$S_{yy}(i\omega) = |H(i\omega)|^2 S_{uu}(i\omega) + S_{ee}(i\omega) \quad (3.57)$$

If  $u(t)$  is a white noise forcing function,  $S_{uu}(i\omega)$  is constant for all  $\omega$ . In this case, if the output signal has not been corrupted by measurement noise, Eq. (3.57) can be used to generate a frequency response plot without direct measurements of the input signal. If measurement noise is present and the transfer function  $H(s)$  is strictly proper, the frequency response plot will asymptotically approach  $S_{ee}(i\omega)$ .

With either approach, transfer functions can be synthesized from frequency response data. However, because Fourier techniques are inconsistent, frequency response data have large variances and algorithms used to estimate transfer function parameters must be robust in the presence of noise. With this caveat, parameters  $b_0, \dots, b_m$  and  $a_0, \dots, a_n$  of the transfer function

$$\frac{B(s)}{A(s)} = \frac{b_0 + b_1s + \dots + b_ms^m}{a_0 + a_1s + \dots + a_ns^n} \quad (3.58)$$

are usually found by minimizing a performance index, such as a sum square error criterion:

$$J = \sum_{k=1}^N \left| \frac{B(i\omega_k)}{A(i\omega_k)} - H(i\omega_k) \right|^2 \quad (3.59)$$

This performance index is highly nonlinear, making minimization difficult. Since minimization frequently requires considerable computational effort, several approximate

linear least-squares methods have been devised, although many of these techniques have marginal utility. For example, Levy's method [10] is a noniterative least-squares scheme designed to estimate transfer function coefficients from frequency response data.

However, Levy's method is well known to be biased and produces poor transfer function estimates [39]. Refinements and alternatives to Levy's method, including those introduced by Sanathanan and Koerner, Lawrence and Rogers, Golubev and Horowitz, and Stahl, are described by Whitfield [39]. In his review, Whitfield concludes that when "frequency response data is corrupted by noise, none of the linear least squares approaches can guarantee a physically meaningful model, and a constrained optimization approach seems preferable" [39, p. 1425]. In this light, Eq. (3.59) can be minimized with the Levenberg-Marquardt or the downhill simplex procedures [28]. Convergence to unbiased estimates is usually obtained when the transfer function does not contain numerator dynamics.

Numerator dynamics are difficult to estimate since their contributions to the frequency response tend to get buried in the noise associated with Fourier techniques.

To illustrate the characteristics of Fourier techniques, periodograms were used to estimate the frequency response of the transfer function

$$H(s) = \frac{3.5}{s^2 + 3.0s + 3.5} \quad (3.60)$$

With a Gaussian random forcing function, periodograms were generated from the output data of Eq. (3.60) using data record lengths of 1024. Estimated frequency responses of the transfer function were calculated from the periodograms using Eq. (3.56). An estimate of the frequency response from a single periodogram is shown in Fig. 3.4, and an estimate of the frequency response from the average of 50 periodograms is shown in Fig. 3.5. Notice that while the frequency response of this transfer function can be accurately estimated by

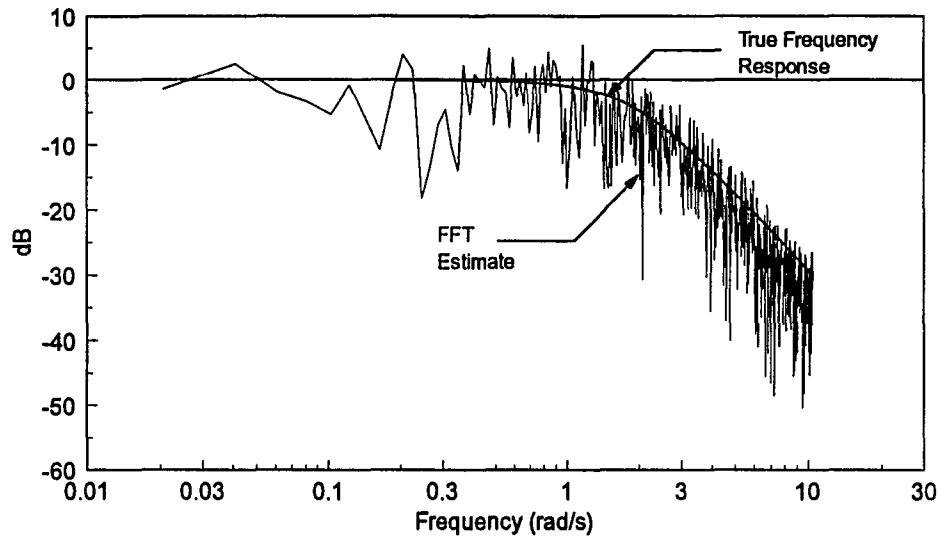


Fig. 3.4: Frequency response estimate of Eq. (3.60) from a single periodogram

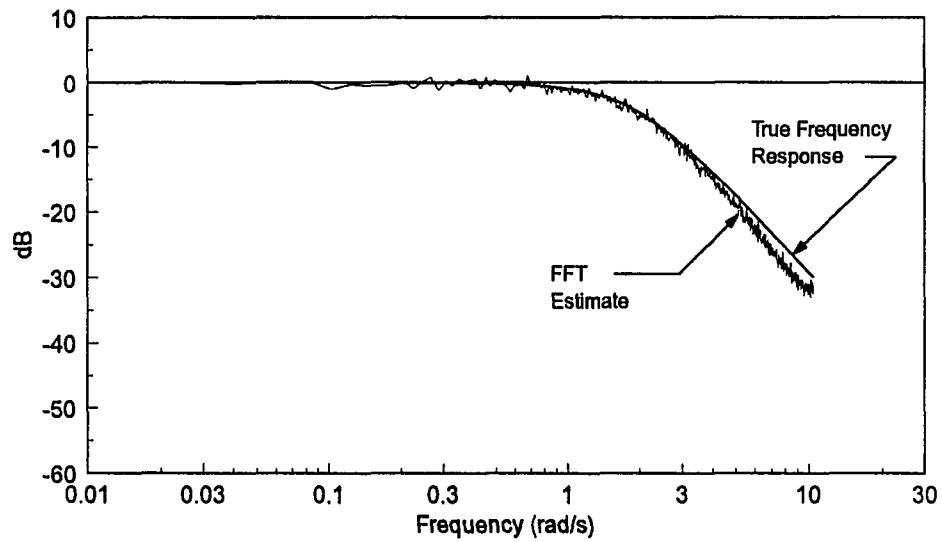


Fig. 3.5: Frequency response estimate of Eq. (3.60) from the average of 50 periodograms

averaging several periodograms, a good estimate requires an inordinate amount of data (i.e.,  $1024 \times 50$  data points).

### 3.2.2 Parametric Spectral Estimation Methods

One of the difficulties (among many) with Fourier techniques is that estimates of the frequency response are limited to integer multiples of  $\omega_o$ . This limitation can be overcome in part by zero-padding the data set [21]; however, this will not improve the resolution of the periodogram. While this is not a serious restriction for many slow-moving chemical processes, better spectral estimates can be generated through parametric techniques.

Parametric spectral estimation is done in three stages: (1) the model structure is selected, (2) the model parameters are estimated, and (3) the estimated system model is transformed into the frequency domain. Of the three stages in parametric modeling, selecting the correct model structure is perhaps the most difficult. This stage is often circumvented by assuming that the system structure is known a priori. With a known model structure, parametric spectral estimates have infinite resolution. That is, once the system is known, the frequency domain representation of that system can be calculated for all  $\omega$ . In practice, though, modeling errors create biases in the spectral estimates, limiting their ability to correctly resolve frequency characteristics.

One factor that distinguishes parametric spectral estimation methods from most other system identification schemes is that the input process is assumed to be unavailable for analysis. As with Fourier techniques, systems can be analyzed with output data alone if the input signal is a white noise process. Therefore, since only output data are assumed to be measurable, most parametric methods are designed to estimate parameters of the AR model

$$H(z) = \frac{1}{A(z)} \quad (3.61)$$

where  $A(z) = a_0 + a_1z^{-1} + \dots + a_nz^{-n}$ . For a linear system with an input signal  $u(z)$  and an uncorrupted output signal  $x(z)$ , the spectral density function  $S_{xx}(z)$  is related to  $S_{uu}(z)$  by

$$S_{xx}(z) = H(z)H(z^{-1})S_{uu}(z) \quad (3.62)$$

where  $z$  is evaluated on the unit circle (i.e.,  $z = e^{i\omega}$ ) [21]. If the input signal is a white noise process,  $S_{uu}(e^{i\omega}) = \sigma_u^2$ , where  $\sigma_u^2$  is a constant. Therefore, the power spectral density function for an AR model driven by a white noise process is

$$S_{xx}(e^{i\omega}) = \frac{\sigma_u^2}{|A(e^{i\omega})|^2} \quad (3.63)$$

Once the polynomial  $A(z)$  is known, the power spectral density of the system can be easily calculated with Eq. (3.63). Therefore, the principal objective of parametric spectral estimation methods is to accurately estimate the coefficients of this polynomial. Several parameter estimation schemes have been developed for this purpose, many of which make extensive use of the autocorrelation function. One such scheme is the autocorrelation method. This method is based on the Yule-Walker equations, which relate the autocorrelation function to coefficients of an  $n^{\text{th}}$ -order AR model:

$$r_{xx}(k) = \begin{cases} -\sum_{i=1}^n a_i r_{xx}(k-i) & k \geq 1 \\ -\sum_{i=1}^n a_i r_{xx}(-i) + \sigma_u^2 & k = 0 \end{cases} \quad (3.64)$$

For  $k = 1, 2, \dots, n$ , a set of  $n$  linearly independent equations can be generated. Collectively,

$$\begin{bmatrix} r_{xx}(0) & r_{xx}(-1) & \cdots & r_{xx}(1-n) \\ r_{xx}(1) & r_{xx}(0) & \cdots & r_{xx}(2-n) \\ \vdots & \vdots & \ddots & \vdots \\ r_{xx}(n-1) & r_{xx}(n-2) & \cdots & r_{xx}(0) \end{bmatrix} \begin{bmatrix} a_1 \\ a_2 \\ \vdots \\ a_n \end{bmatrix} = \begin{bmatrix} -r_{xx}(1) \\ -r_{xx}(2) \\ \vdots \\ -r_{xx}(n) \end{bmatrix} \quad (3.65)$$

In most cases, the autocorrelation function is not known a priori and must be estimated from a finite data set. For a set of  $N$  data points,  $\{x(0), x(1), \dots, x(N-1)\}$ , the autocorrelation function can be estimated through the following summation [21]:

$$\hat{r}_{xx}(k) = \begin{cases} \frac{1}{N} \sum_{j=0}^{N-1-k} x(j)x(j+k) & k = 0, 1, 2, \dots, N-1 \\ \hat{r}_{xx}(-k) & k = -(N-1), \dots, -1 \end{cases} \quad (3.66)$$

Substituting  $\hat{r}_{xx}(k)$  for  $r_{xx}(k)$  in Eq. (3.65), coefficients  $a_1, a_2, \dots, a_n$  can be solved by inverting the autocorrelation data matrix. Because this matrix is symmetric Toeplitz, it can be efficiently inverted with Levinson's recursion [28].

Many other methods are available for estimating coefficients of AR models, including the modified covariance method, the maximum entropy method, and Prony's method. However, AR parameter estimation methods yield poor results when output data are corrupted by even the slightest amount of noise [21]. For example, consider a dynamic system with output  $y(z) = x(z) + e(z)$ , where  $x(z)$  is the uncorrupted process signal and  $e(z)$  is a white noise process. In terms of power spectral density functions,

$$\begin{aligned} S_{yy}(e^{i\omega}) &= S_{xx}(e^{i\omega}) + S_{ee}(e^{i\omega}) \\ &= |H(e^{i\omega})|^2 S_{uu}(e^{i\omega}) + S_{ee}(e^{i\omega}) \end{aligned} \quad (3.67)$$

For an AR process,  $H(e^{i\omega}) = 1/A(e^{i\omega})$  and  $S_{ee}(e^{i\omega}) = \sigma_e^2$ . Therefore, the power spectral density function of  $y(z)$  is

$$\begin{aligned} S_{yy}(e^{i\omega}) &= \frac{\sigma_u^2}{|A(e^{i\omega})|^2} + \sigma_e^2 \\ &= \frac{\sigma_u^2 + \sigma_e^2 |A(e^{i\omega})|^2}{|A(e^{i\omega})|^2} \end{aligned} \quad (3.68)$$

The right-hand side of Eq. (3.68) describes a power spectral density function of an ARMA process. This suggests that an AR process corrupted by measurement noise is better

modeled as an ARMA process. Unfortunately, MA parameter estimators are the weak link in parametric spectral estimation techniques since MA parameters are difficult to estimate without direct measurements of the input signal. As a result, only a few MA parameter estimation schemes have been developed. One of these schemes is Durbin's method. This method relies on a theorem due to Kolmogorov, which states that a finite-order MA model can be represented by an infinite-order AR model [21]. By approximating an infinite-order AR model with a large – but finite – AR model, AR parameters can be estimated with the autocorrelation method. Once the AR parameters have been calculated, MA parameters can be estimated through an inverse transformation.

While Durbin's method can be used to estimate MA parameters, the problem of efficiently separating AR coefficients from MA coefficients has yet to be solved. AR and MA parameters can be estimated simultaneously with a maximum likelihood estimator; however, this involves minimizing a set of highly nonlinear equations through iterative optimization techniques [21,26]. Besides being difficult to implement, iterative optimization techniques may not converge or they may converge to the wrong solution [21,26]. Suboptimal schemes are available, many of which estimate AR and MA parameters independently. For example, Akaike's procedure uses modified Yule-Walker equations to estimate AR coefficients. Once the AR parameters have been estimated, the process data are filtered by  $A(z)$  to generate an approximate MA process. Finally, parameters of the MA process are estimated through Durbin's method or through an equivalent MA estimation scheme.

Difficulties with estimating ARMA parameters limits the practical utility of modern spectral estimation methods. While parametric AR spectral estimators are high resolution estimators, most experimental data are corrupted by measurement noise, making ARMA parameter estimation necessary. Moreover, even with an uncorrupted process signal, few

physical systems are strictly AR processes; many dynamic systems have MA components. Therefore, for many practical applications, Fourier techniques, despite their shortcomings, are preferable.

### 3.3 Continuous-Time System Identification

Although estimating system coefficients from frequency data can be difficult, classical spectral methods are nonparametric and can be useful when determining relative model order. For example, by constructing a Bode plot from frequency data, a  $-20$  dB/dec roll-off indicates a transfer function with numerator dynamics of order  $N$  and denominator dynamics of order  $N + 1$ . This information can be used to build a model structure for parametric system identification algorithms, such as the Poisson moment functional (PMF) approach.

With the PMF approach, signals are expressed as generalized functions. In the Laplace domain, this approach allows functions of differentials to be mapped onto linear combinations of cascaded filters. Because the PMF approach circumvents direct estimation of derivatives, it is resistant to the effects of measurement noise. With this method, linearly independent equations are generated by expressing a function and its derivatives in terms of Poisson moment functionals, which are found through a modified Poisson transformation. For example, consider a function  $f(t)$  defined in the interval  $[0, t_o]$ . The PMF transform of  $f(t)$  about  $t_o$  is defined as

$$M_k[f(t)] = f_k(t_o) = \int_0^{t_o} f(t) p_k(t_o - t) dt \quad (3.69)$$

$$p_k(t_o) = \frac{t_o^k}{k!} e^{-\lambda}, \quad \lambda \geq 0, \quad k = 0, 1, 2, 3, \dots$$

Like the Laplace transform,  $M_k[\cdot]$  is a linear operator [13]. However, the PMF transform differs from the Laplace transform in that it converts  $f(t)$  into a set of real numbers at  $t = t_o$ . Note that this transform can be interpreted as the convolution of  $f(t)$  with the impulse response of  $(k + 1)$  cascaded filters, each with the transfer function

$$\frac{1}{s + \lambda} \quad (3.70)$$

This cascade is often referred to as a Poisson filter chain (PFC). A block diagram of a PFC is illustrated in Fig. 3.6.

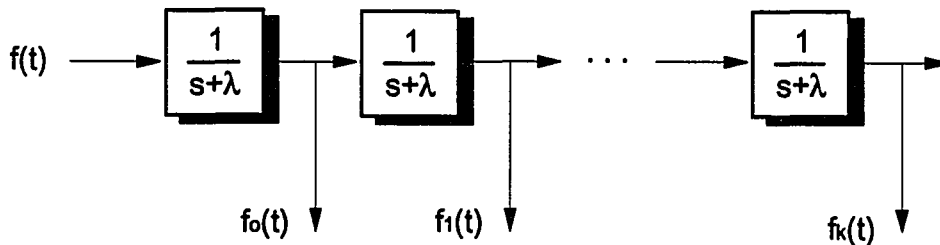


Fig. 3.6: Block diagram of a Poisson filter chain

### 3.3.1 Calculation of PMF Coefficients

In practice, values for  $f_k(t_o)$  can be measured directly from an analog filter chain. A complete description (including wiring diagrams) of an analog filter chain coupled with a microprocessor-based data acquisition system is presented by Saha and Rao [30]. A different approach is required when evaluating data numerically. Given input and output data, Poisson moment functionals can be evaluated numerically by transforming the PFC into the following set of first-order differential equations:

$$\begin{bmatrix} f'_0(t) \\ f'_1(t) \\ \vdots \\ f'_k(t) \end{bmatrix} = \begin{bmatrix} -\lambda & 0 & \dots & 0 \\ 1 & -\lambda & \dots & 0 \\ \vdots & \vdots & \ddots & \vdots \\ 0 & 0 & \dots & -\lambda \end{bmatrix} \begin{bmatrix} f_0(t) \\ f_1(t) \\ \vdots \\ f_k(t) \end{bmatrix} + \begin{bmatrix} 1 \\ 0 \\ \vdots \\ 0 \end{bmatrix} f(t) \quad (3.71)$$

For a smooth forcing function, Eq. (3.71) can be evaluated through standard integration algorithms, such as the Runge-Kutta or Bulirsch-Stoer methods. On the other hand, for signals corrupted by noise,  $f_k(t_o)$  can be evaluated by transforming Eq. (3.71) into the discrete-time domain. In the discrete-time domain, the numerical difficulties associated with stochastic processes are eliminated since forcing functions are assumed to be constant in the interval  $t$  to  $t + \Delta t$ . Clearly, better estimates are obtained as the sampling interval decreases. Note that this procedure does not have the difficulties associated with discrete-time parameter estimation since the system matrices are known precisely.

For a linear differential equation, PMF transforms can be evaluated for a function and its time derivatives. For nonzero initial conditions, the PMF transforms of a function  $f(t)$  and its first two time derivatives about  $t_o$  are [30]

$$\begin{aligned} M_k[f(t)] &= f_k(t_o) \\ M_k[f'(t)] &= f_{k-1}(t_o) - \lambda f_k(t_o) - p_k(t_o)f(0) \\ M_k[f''(t)] &= f_{k-2}(t_o) - 2\lambda f_{k-1}(t_o) + \lambda^2 f_k(t_o) \\ &\quad - [p_{k-1}(t_o) - \lambda p_k(t_o)]f(0) - p_k(t_o)f'(t_o) \end{aligned} \quad (3.72)$$

Derivations of these transforms are presented in Appendix C. Notice that for  $\lambda > 0$ ,  $\lim_{t_o \rightarrow \infty} p_k(t_o) = 0 \forall k$ . In words, a low-pass filter chain "filters-out" initial conditions as time increases. Therefore, if initial conditions are not well known,  $t_o$  should be set large enough to allow initial condition transients to subside. When calculating PMF transforms with a large  $t_o$ , initial conditions can be neglected, and the PMF transforms in Eq. (3.72) become

$$\begin{aligned} M_k[f(t)] &= f_k(t_o) \\ M_k[f'(t)] &= f_{k-1}(t_o) - \lambda f_k(t_o) \\ M_k[f''(t)] &= f_{k-2}(t_o) - 2\lambda f_{k-1}(t_o) + \lambda^2 f_k(t_o) \end{aligned} \quad (3.73)$$

For nonzero initial conditions, the time required for initial transients to subside depends on the choice of  $\lambda$ . As  $\lambda$  increases, initial transients settle faster. However, by increasing  $\lambda$ , the filter cascade becomes less effective in attenuating noise. Therefore, the choice of  $\lambda$  requires a tradeoff between knowledge of initial conditions and the need to attenuate measurement noise.

Designing an appropriate filter cascade is not an elementary task. Even when initial conditions are known exactly, consideration must be given to the tendency of low pass filters to "wash-out" fast system dynamics. As with initial conditions, the ability of the filter chain to track fast system dynamics competes directly with the ability to attenuate measurement noise. To date, there are no good design guidelines, and, as such, many authors arbitrarily choose  $\lambda = 1$  [4,30,35]. However, since the design requirements for a PFC are not far removed from the design requirements of an observer polynomial [23], insights into a possible compromise lie within the design guidelines of an observer. Intuitively, an observer must be fast enough to track system dynamics, but not so fast that the observer becomes sensitive to measurement noise. Therefore, observer polynomials are designed to have roots just to the left of the fastest system dynamics. The design requirements for a PFC are not as stringent as those for an observer in that the PMF method performs adequately when the filter roots are on the same order of magnitude as the fastest system dynamics.

### **3.3.2 Estimation of System Parameters from PMF Coefficients**

Parameter estimation through the PMF transform is best described by means of an example. Consider the following second-order system with forcing function  $u(t)$  and zero initial conditions:

$$y''(t) + a_1 y'(t) + a_2 y(t) = b_o u(t) \quad (3.74)$$

Taking transforms of each element about time  $t_o$ , Eq. (3.74) maps onto the following algebraic relationship:

$$\begin{aligned} [y_{k-2}(t) - 2\lambda y_{k-1}(t) + \lambda^2 y_k(t)] + a_1 [y_{k-1}(t) - \lambda y_k(t)] \\ + a_2 [y_k(t)] = b_o u_k(t) \end{aligned} \quad (3.75)$$

Two methods are available for estimating coefficients  $a_1$ ,  $a_2$ , and  $b_o$  of the transformed differential equation. In the first method,  $n$  independent equations are generated by fixing  $k$  and sampling the corresponding filter chain at times  $t_o, t_1, \dots, t_{n-1}$  (which may be nonuniformly spaced). Notice that identification is continuous-time even though process signals are sampled discretely.

Some mild restrictions exist for assigning  $k$ . For example,  $k$  must be chosen so that the lowest-order moment functional is no less than  $y_{-1}$  (i.e., the original, unfiltered signal). Some authors, such as Bergman and Hale [4], use the PMF method with  $y_{-1}$  to identify systems with process signals that are free of measurement noise. However, Saha recommends that process signals be filtered at least once to attenuate measurement noise [30]. To do this,  $k$  should be chosen so that the lowest-order moment functional is no less than  $y_o$ . Conversely,  $k$  should not be chosen so large that the filter chain completely filters out the process signal. While this is not a restriction, system dynamics, especially fast system dynamics, become difficult to estimate with higher-order Poisson filter chains. Therefore, to balance attenuation of noise with attenuation of the process signal,  $k$  is usually chosen so that the minimum moment functional is  $y_o$ .

With this in mind, let  $k = 2$  so that  $y_o$  becomes the minimum moment functional in Eq. (3.75). With  $k$  fixed,  $n$  independent equations can be generated by sampling the moment functionals at times  $t_o, t_1, \dots, t_{n-1}$ . Collectively, these equations can be written as

$$\Phi \theta = \Psi \quad (3.76)$$

where

$$\Phi = \begin{bmatrix} y_1(t_o) - \lambda y_2(t_o), & y_2(t_o), & -u_2(t_o) \\ y_1(t_1) - \lambda y_2(t_1), & y_2(t_1), & -u_2(t_1) \\ \vdots & \vdots & \vdots \\ y_1(t_{n-1}) - \lambda y_2(t_{n-1}), & y_2(t_{n-1}), & -u_2(t_{n-1}) \end{bmatrix} \quad (3.77)$$

$$\theta = [a_1, a_2, b_o]^T \quad (3.78)$$

and

$$\Psi = \begin{bmatrix} -y_o(t_o) + 2\lambda y_1(t_o) - \lambda^2 y_2(t_o) \\ -y_o(t_1) + 2\lambda y_1(t_1) - \lambda^2 y_2(t_1) \\ \vdots \\ -y_o(t_{n-1}) + 2\lambda y_1(t_{n-1}) - \lambda^2 y_2(t_{n-1}) \end{bmatrix} \quad (3.79)$$

An estimate of the coefficient vector can be obtained through a standard least-squares inversion. Notice that this approach lends itself well to parameter estimation through recursive least-squares [31]. Coupled with a forgetting factor or covariance modification, parameter estimation through recursive least-squares could prove to be a useful tool for tracking slowly varying system parameters.

Alternatively, the required number of independent equations can be generated at a single instant in time by evaluating the transformed differential equation for  $k = 2, 3, \dots, n+1$ . In other words, the required number of independent equations can be generated from a sequence of higher-order filter chains. Collectively, these equations can be written as

$$\bar{\Phi}\theta = \bar{\Psi} \quad (3.80)$$

where

$$\bar{\Phi} = \begin{bmatrix} y_1(t_o) - \lambda y_2(t_o), & y_2(t_o), & -u_2(t_o) \\ y_2(t_o) - \lambda y_3(t_o), & y_3(t_o), & -u_3(t_o) \\ \vdots & \vdots & \vdots \\ y_n(t_o) - \lambda y_{n+1}(t_o), & y_{n+1}(t_o), & -u_{n+1}(t_o) \end{bmatrix} \quad (3.81)$$

$$\theta = [a_1, a_2, b_o]^T \quad (3.82)$$

and

$$\bar{\Psi} = \begin{bmatrix} -y_o(t_o) + 2\lambda y_1(t_o) - \lambda^2 y_2(t_o) \\ -y_1(t_o) + 2\lambda y_2(t_o) - \lambda^2 y_3(t_o) \\ \vdots \\ -y_{n-1}(t_o) + 2\lambda y_n(t_o) - \lambda^2 y_{n+1}(t_o) \end{bmatrix} \quad (3.83)$$

As with the previous method, an estimate of the coefficient vector can be obtained through a standard least-squares inversion. However, in contrast with the previous method, the matrices  $\bar{\Phi}$  and  $\bar{\Psi}$  are calculated at a single moment in time. As a result, this approach does not lend itself well to parameter estimation through recursive least-squares.

Furthermore, estimating system parameters through a sequence of higher-order filter chains is not recommended as higher-order filter chains drastically attenuate the signal, making parameter estimation difficult.

### 3.3.3 Performance of the PMF Method: A Comparative Example

As a comparison with the ELS method, the PMF approach was used to estimate coefficients of the dynamic system

$$\frac{y(s)}{u(s)} = \frac{3.5}{s^2 + 3s + 3.5} \quad (3.84)$$

System parameters were estimated by sequentially sampling a fixed filter chain with  $k = 2$ ; a Matlab macro of the PMF algorithm is presented in Appendix B. For these tests, filter coefficients were set to 1.8 (transfer function poles are at  $-1.5 \pm 1.12i$ ); in all cases, zero initial conditions were enforced. A zero-mean, unity-variance Gaussian-random signal was used as a forcing function. As with the ELS tests, the output signal was corrupted by zero-

mean Gaussian-random noise. So that the performance of the PMF approach can be compared with that of the ELS method, estimated continuous-time transfer functions were transformed into the discrete-time domain. Experimental results are presented in Table 3.2. Notice that the PMF approach effectively estimates system parameters — even with 80% measurement noise.

Table 3.2: Performance of the PMF algorithm

	$a_1$	$a_2$	$b_1$	$b_2$
True	-1.8047	0.8187	0.0073	0.0068
NSR				
0%	-1.8071	0.8209	0.0072	0.0067
1%	-1.8069	0.8209	0.0072	0.0067
2%	-1.8069	0.8209	0.0072	0.0062
5%	-1.8072	0.8212	0.0072	0.0067
15%	-1.8084	0.8225	0.0072	0.0067
25%	-1.8099	0.8239	0.0072	0.0067
80%	-1.8180	0.8318	0.0069	0.0065

## **4. EXPERIMENTAL APPARATUS AND PROCEDURES**

One objective of this investigation is to develop a nonlinear dynamic model of coal combustion in a fluidized bed combustor. To verify this model, theoretical responses were compared with experimental data obtained from batch tests of coal with known initial distributions. The following sections describe the experimental apparatus and experimental procedures used to verify this model. Included in this chapter are descriptions of the fluidized bed system, data acquisition hardware, and test procedures.

### **4.1 Combustor Design**

Experiments were carried out in a 20 cm diameter bubbling bed combustor. A process diagram of the combustor is shown in Fig. 4.1. Air is introduced into the bed through a multiorifice distributor plate. The distributor plate, constructed from 12.7 mm thick stainless steel stock, has 250 evenly spaced orifices, each with a diameter of 2.4 mm. The large number of orifices prevent gas channeling and provide uniform fluidizing characteristics within the bed. Spot-welded to the upper surface of the distributor plate, a 100 mesh stainless steel screen restricts backflow of sand into the air plenum. In addition to retaining sand, the screen functions as a flame arrester, preventing unaided flame propagation of propane into the primary air supply line during combustor operations.

The combustor wall, constructed from a 3.2 mm thick stainless steel insert, is lined with 25 mm of Kaocast RFT refractory. Aside from the distributor plate and combustor

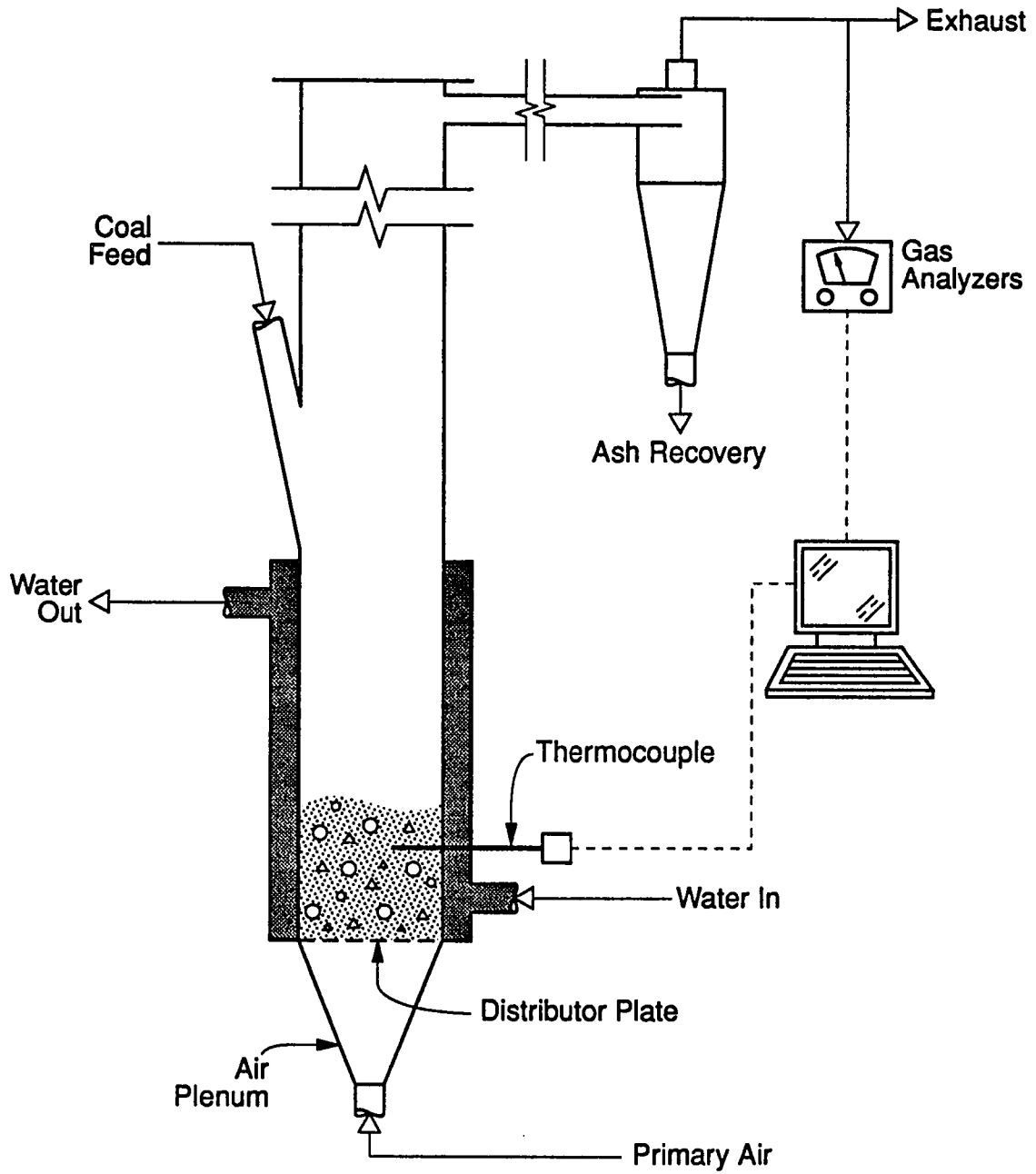


Fig. 4.1: Schematic diagram of the experimental apparatus

wall, all other construction is of mild steel. To cool the bed, the combustion chamber is surrounded by a water jacket. Above the combustion chamber, flue gases travel through a 1.2 m long, uninsulated freeboard. From the freeboard, flue gases pass through a high-efficiency cyclone where 90% of all entrained particles greater than 10  $\mu\text{m}$  are removed. Following the cyclone, combustion gases exhaust from the system through an induced draft fan.

## 4.2 Data Acquisition

Temperature, air flow rate, and gas concentration data were acquired with an HP Vectra QS/16S microcomputer. The Vectra QS/16S is based on the Intel 80386SX processor. The unit was configured with an Intel 80387 math coprocessor, 1 MB of addressable memory, and a 40 MB hard drive. The data interface consisted of a Metrabyte DAS-8 A/D converter. The DAS-8 is an 8-channel, 12-bit, successive approximation A/D converter with conversion time of 25  $\mu\text{s}$ . Data acquisition codes, written and compiled with Microsoft BASIC v. 7.1, logged data at 0.2 second intervals, roughly one-tenth the fastest measurable time constant.

Temperature data were obtained from type-K (chromel/alumel) thermocouple probes. The probes were connected to a Metrabyte sub-multiplexer board (Model EXP-16), which amplified thermoelectric voltages and provided cold junction compensation. Analog signals from the sub-multiplexer board were sent to the DAS-8 A/D interface board.

Primary air flow rates were calculated from pressure drops across an orifice flow meter. Pressure drops across the meter were measured with a Schaevitz LVDT pressure transducer (Model P3061) and calibrated against a laminar flow meter. Analog signals

from the pressure transducer were sent to the DAS-8 A/D converter, whereupon air flow rates were interpolated from calibrated pressure drop data.

To minimize particulate fouling, exhaust gas samples were drawn from the system immediately downstream of the cyclone. Beckman Model 870 infrared spectrometers measured CO and CO<sub>2</sub> concentrations, and a Beckman Model 855 oxygen analyzer measured O<sub>2</sub> concentrations. Off-line, the CO and CO<sub>2</sub> analyzers had 5% settling times under 2 seconds. On-line, the sample line volume increased the settling time to 8 seconds. In contrast, the oxygen analyzer had an off-line settling time of 20 seconds. Because the transient response of the oxygen analyzer was poor, it was only used to measure steady-state concentrations.

### 4.3 Experimental Procedures

Experiments were performed using a bed of river sand. The bed had a static height of 15 cm and contained sand sieved to a bottom size of 0.4 mm and a top size of 0.6 mm. Air at atmospheric pressure was used to fluidized the bed. In all tests, the primary air flow rate was set to produce a superficial velocity of 1 m/s at a bed temperature of 842 °C. For consistency, all experiments were performed using an Indiana bituminous coal. Proximate and ultimate analyses of this coal are presented in Table 4.1.

Table 4.1: Indiana bituminous coal analyses

Proximate Analysis	Pct.	Ultimate Analysis	Pct.
Moisture	13.86	Carbon	73.84
Volatile matter	33.05	Hydrogen	5.13
Fixed carbon	45.07	Nitrogen	1.12
Ash	8.02	Oxygen	8.76
		Sulfur	1.85

To reduce background noise, the bed was heated to  $842 \pm 15$  °C with propane throughout the test runs. At steady-state conditions, the combustor had a 14 – 15 % baseline CO<sub>2</sub> concentration with a corresponding 7 – 6 % baseline O<sub>2</sub> concentration. When steady-state conditions had been attained, samples of coal were batched into the bed, generating transient perturbations in CO<sub>2</sub> and O<sub>2</sub> concentrations.

## 5. RESULTS AND DISCUSSION

For these experiments, coal particle distributions are loosely classified as "small" particle (about 1 mm) or "large" particle (about 5 mm). The distinction pertains to the degree of fragmentation the particle experiences when it first enters the combustion chamber. Chirone et al. [7] survey recent fragmentation research, including work describing size dependent characteristics in bituminous coals. For Indiana bituminous coal, small particles do not fragment whereas large particles readily fragment.

As might be expected, particle fragmentation has a profound effect on the impulse response. For this reason, this chapter has been divided along small particle and large particle distributions.

### 5.1 The Nonlinear Combustion Model: Small Particle Distributions

Small particle distributions are small enough that they do not fragment but are not so small that chemical kinetics become rate-limiting (as with pulverized coal). A typical impulse response for a small particle block distribution is presented in Fig. 5.1. Initially, the CO<sub>2</sub> transient is dominated by volatile combustion. However, this transient response decays roughly as fast as the instrumentation response, making separation of signals difficult. The remainder of the transient response characterizes char combustion. Unlike the volatile response, char combustion is slow enough that the instrumentation can adequately track the signal.

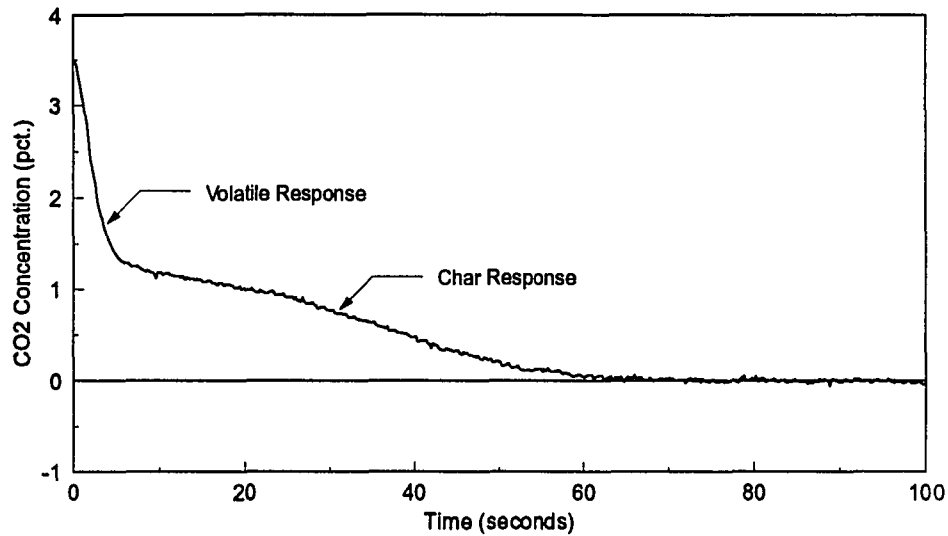


Fig. 5.1: Typical small particle response

An unusual feature of the char transient is the change in curvature from a negative second derivative to a positive second derivative. These characteristics are also present in Eqs. (2.57) and (2.58). That is, Eq. (2.57) has a negative definite second derivative whereas Eq. (2.58) has a positive definite second derivative. In these equations, the curvature changes at  $t = D_{\min}^2 / 2f$ , the time at which the smallest particles burn out. Physically, because smaller particles approach zero faster than large particles, a block distribution initially expands, creating a negative second derivative. This distribution expands until the smallest particles burn out. After that, the distribution can only contract, resulting in a change of curvature.

Although  $K(t)$  is uniformly continuous for  $0 \leq t \leq D_{\max}^2 / 2f$ , the first and second derivatives are piecewise continuous in this interval. A jump discontinuity occurs at  $t = D_{\min}^2 / 2f$ ; therefore, in a strict sense,  $K(D_{\min}^2 / 2f)$  is not a point of inflection. This discontinuity occurs because a block distribution has well-defined edges. In practice, these

edges are fuzzy, and the lack of sharp edges smoothes discontinuities, producing a response with a point of inflection. Therefore, with a slight abuse of terminology,  $K(D_{\min}^2 / 2f)$  will be referred to as a point of inflection.

A point of inflection at  $t_i = D_{\min}^2 / 2f$  suggests that  $t_i$  decreases as  $D_{\min}$  decreases. To test this hypothesis, several block distributions were formed where  $D_{\max}$  was held constant and  $D_{\min}$  was varied. So that a uniform distribution could be better approximated, consecutive screen samples were combined, each with a mass fraction

$$x_i = \frac{\lambda \Delta D_i}{\sum_{i=1}^N \lambda \Delta D_i} = \frac{\Delta D_i}{\sum_{i=1}^N \Delta D_i} \quad (5.1)$$

where  $\Delta D_i$  is the difference between the top and bottom particle sizes in each sieve. Small particle tests were carried out for  $16 \times 18$  through  $25 \times 30$  mesh coal; mass fractions for (nearly) uniform particle distributions are presented in Table 5.1. Since all tests were run with 5 g samples,  $\phi_o$  decreases as the distribution widens. In Table 5.1, different initial block distributions are denoted by a superscript index. For example, mass fractions for  $16 \times 20$  mesh coal are listed in the column labeled  $\phi_o^2$ .

Theoretical impulse responses for block particle distributions were fit to the experimental data sets. Given  $D_{\max}$ , coefficients  $D_{\min}$ ,  $\phi_o$ , and  $f$  were estimated by minimizing the sum square error with a fourth-order, downhill simplex [28]. So that the

Table 5.1: Mass fractions for uniform  $\lambda$  distributions

Mesh	$D_{\max}$ (mm)	$D_{\min}$ (mm)	$\Delta D$ (mm)	$\phi_o^1$	$\phi_o^2$	$\phi_o^3$	$\phi_o^4$
16 x 18	1.18	1.00	0.18	1.00	0.55	0.38	0.31
18 x 20	1.00	0.85	0.15		0.45	0.32	0.26
20 x 25	0.85	0.71	0.14			0.30	0.24
25 x 30	0.71	0.60	0.11				0.19

simplex would converge to realistic values, an exponential penalty function was used to enforce the following constraints:

$$\begin{aligned} 0 < D_{\min} < D_{\max} \\ f > 0 \\ \phi_o > 0 \end{aligned} \quad (5.2)$$

Numerical results are presented in Table 5.2; the data sets are plotted in Figs. 5.2 through 5.5.

Table 5.2: Impulse response data

Mesh Designation	16 x 18	16 x 20	16 x 25	16 x 30
<b>Sieve Data</b>				
$D_{\min}$ (mm)	1.00	0.85	0.71	0.60
$D_{\max}$ (mm)	1.18	1.18	1.18	1.18
<b>Simplex Est.</b>				
$D_{\min}$ (mm)	0.89	0.83	0.77	0.68
$f$ (mm <sup>2</sup> /s)	0.0091	0.0100	0.0100	0.0104
$\phi_o$ (g/mm)	6.19	5.26	4.53	3.67

Some discrepancies exist between the sieve data and the simplex estimates. Most of the error can be ascribed to insufficient knowledge of the particle distribution. When coal is sieved, many different shapes of coal, including shards and slivers, are classified as spheres with diameters bounded by the mesh openings. However, despite these discrepancies, experimental data follow theoretical trends well.

## 5.2 The Nonlinear Combustion Model: Large Particle Distributions

When large particle bituminous coal enters a fluidized bed, some particles fragment, a process referred to as primary fragmentation. Primary fragmentation – caused

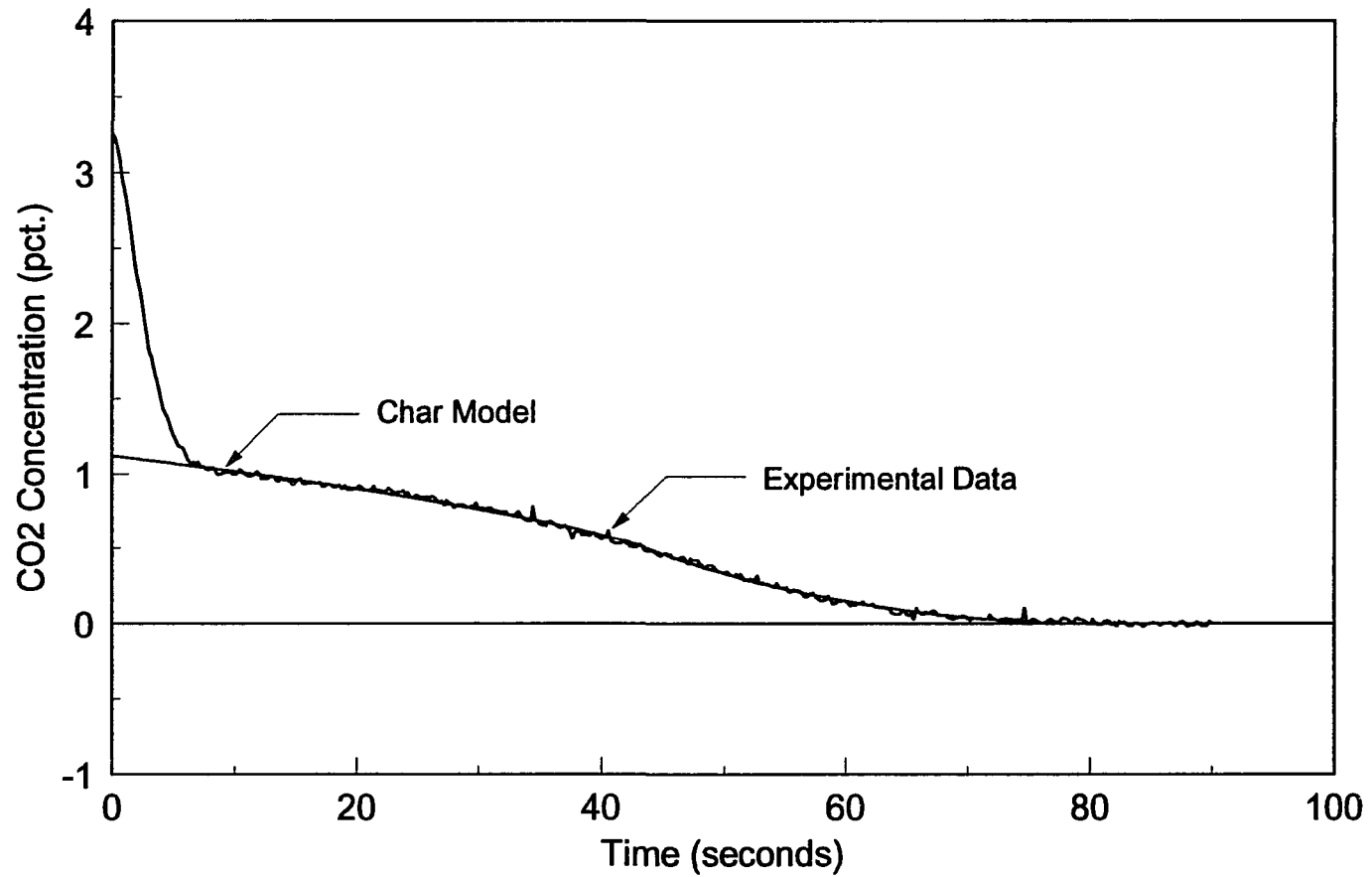


Fig. 5.2: Small particle char model (16 × 18 mesh)

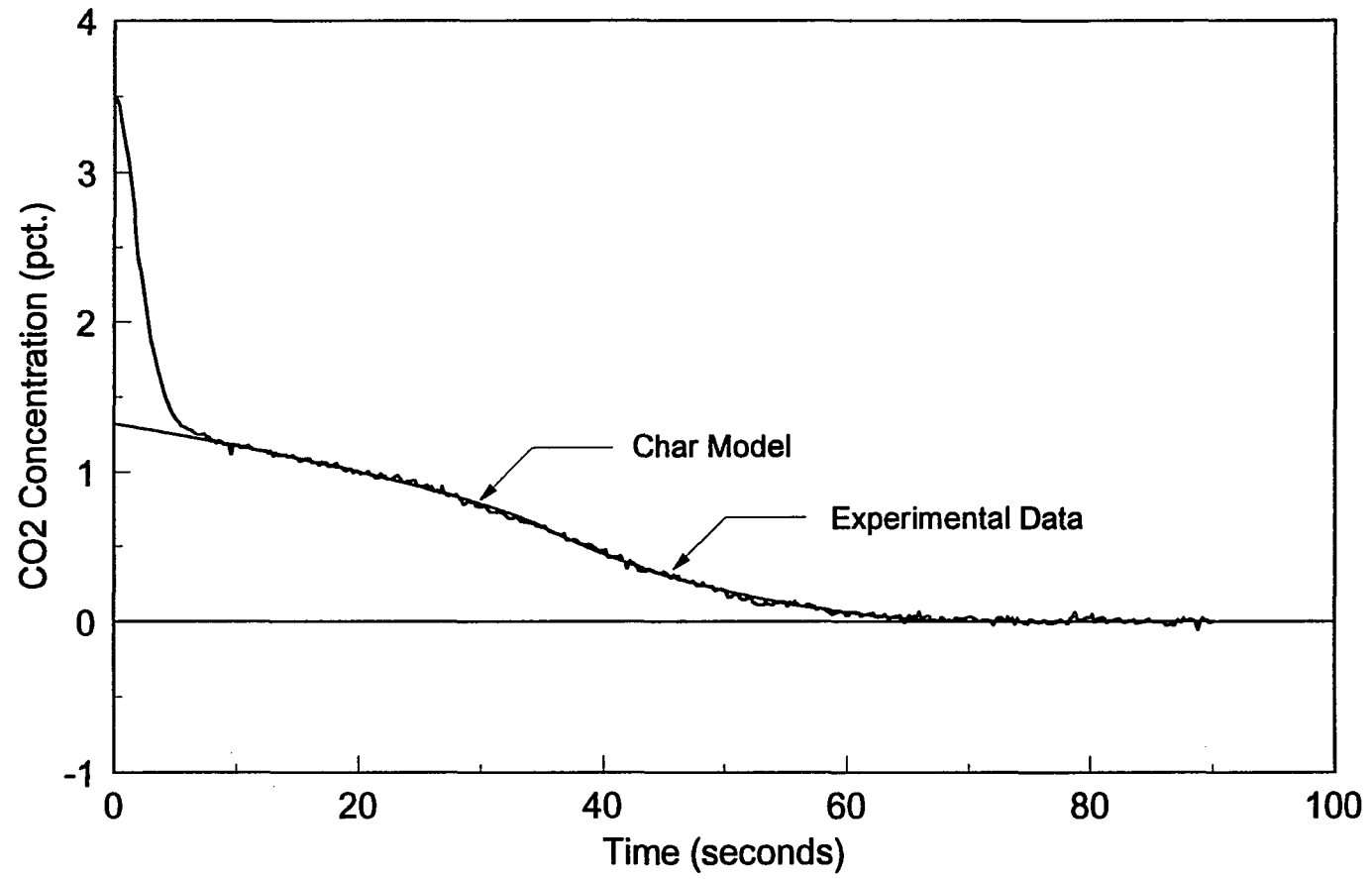


Fig. 5.3: Small particle char model (16 × 20 mesh)

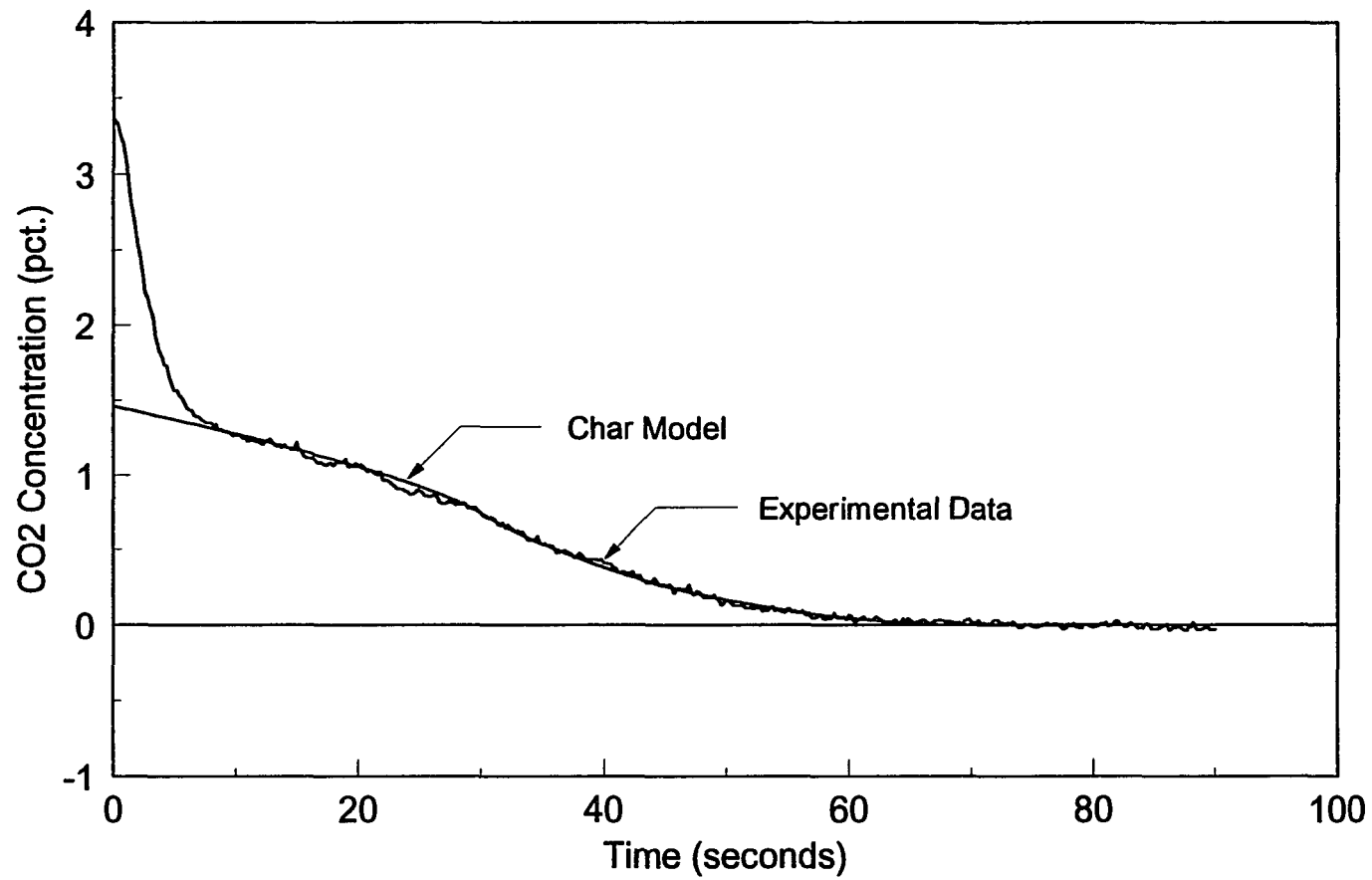


Fig. 5.4: Small particle char model (16 × 25 mesh)

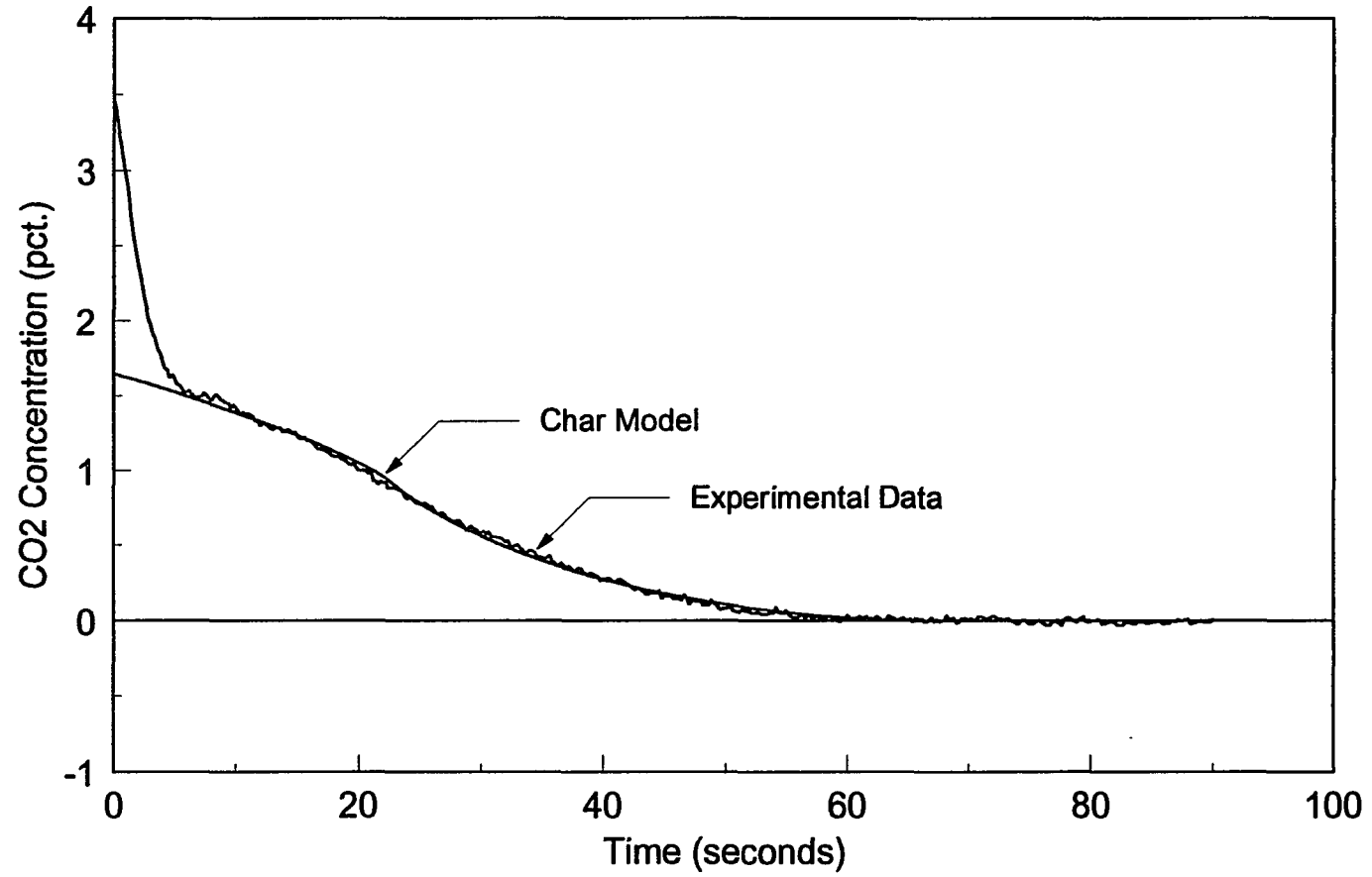


Fig. 5.5: Small particle char model (16 × 30 mesh)

by thermal shock and devolatilization – occurs quickly [7], and the resulting fragmented particle distribution guides the impulse response. As such, the effective initial mass distribution is the fragmented mass distribution [12]. However, because the fragmented particle distribution is not known beforehand, the impulse response for large particles is difficult to predict.

To examine the effects of fragmentation on the impulse response, two consecutive tests were performed: one to acquire the impulse response and another to obtain an estimate of the fragmented distribution. Fragmentation data from the second test were then used to model the impulse response of the first test.

A 40 g sample of 3.5 x 4 mesh (4.75 mm – 5.60 mm) coal was evenly divided into two, 20 g samples. One sample was batched into the combustor, and the transient response was recorded. When this transient response had decayed to zero, the second sample was batched into the combustor. After the volatile response had subsided, the bed was quenched with nitrogen. When the bed had cooled, char particles were separated from the bed material and classified. The cumulative char distribution, along with a continuous estimate, is shown in Fig. 5.6; the derivative of the cumulative distribution,  $\lambda(D,0^+)$ , is shown in Fig. 5.7. A noteworthy feature of  $\lambda(D,0^+)$  is the jump discontinuity at  $D \approx 4.00$ . This discontinuity is a separation between particle fragments ( $D < 4.00$  mm) and unfragmented particles ( $D > 4.00$  mm).

Because the coal samples came from the same stock, the particle distribution for the impulse response was assumed to be proportional to the distribution obtained from the quench test; i.e., for some constant,  $k$ ,  $\phi(D_o) = k\lambda(D_o,0^+) \forall D_o$ . Given  $D_{\max}$  and  $\lambda(D,0^+)$ , coefficients  $f$  and  $k$  were adjusted to fit the experimental data. The response for  $f = 2.1 \times 10^{-2}$  mm<sup>2</sup>/s, and  $k = 0.96$  is illustrated in Fig. 5.8

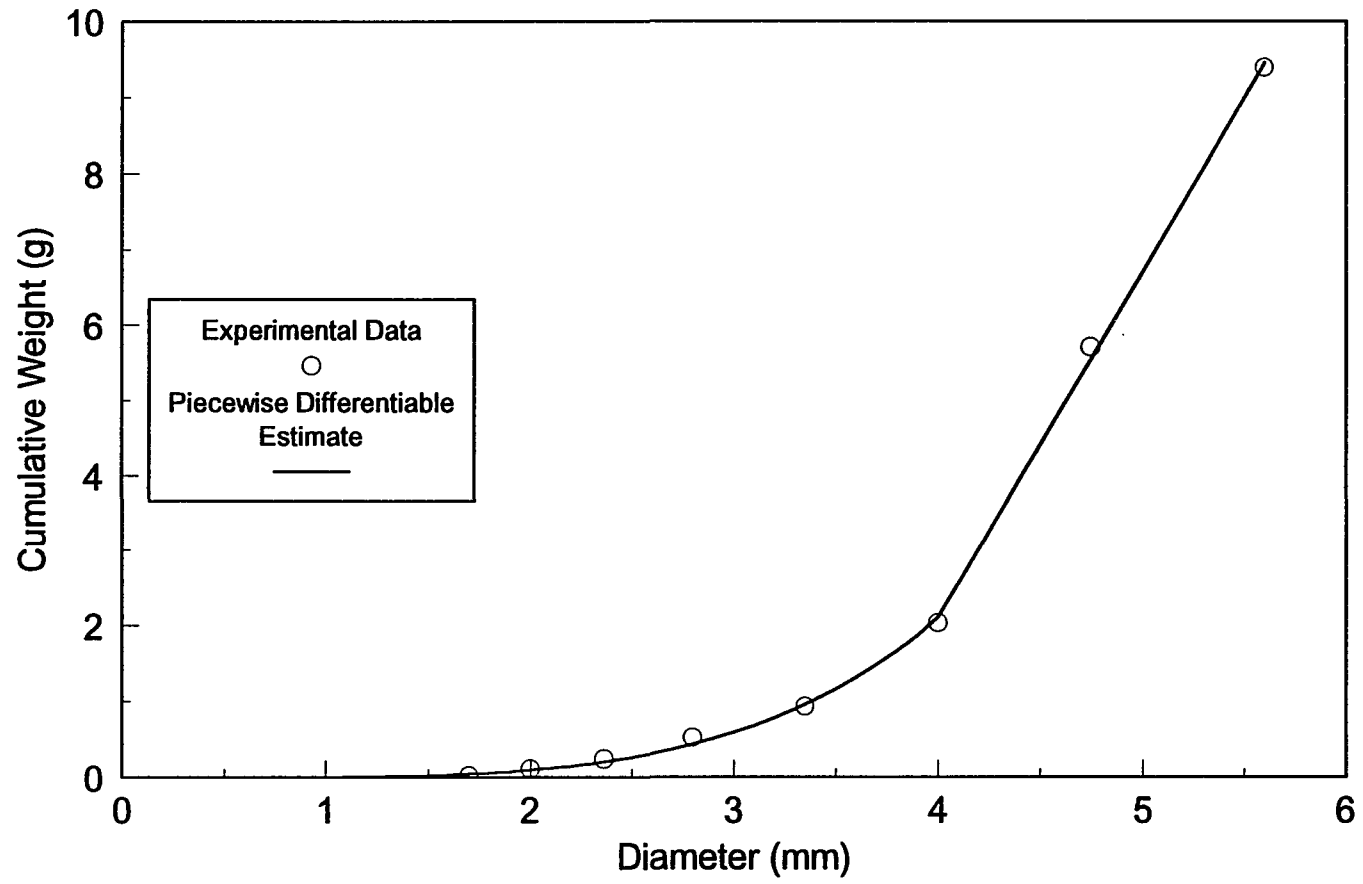


Fig. 5.6: Cumulative mass distribution

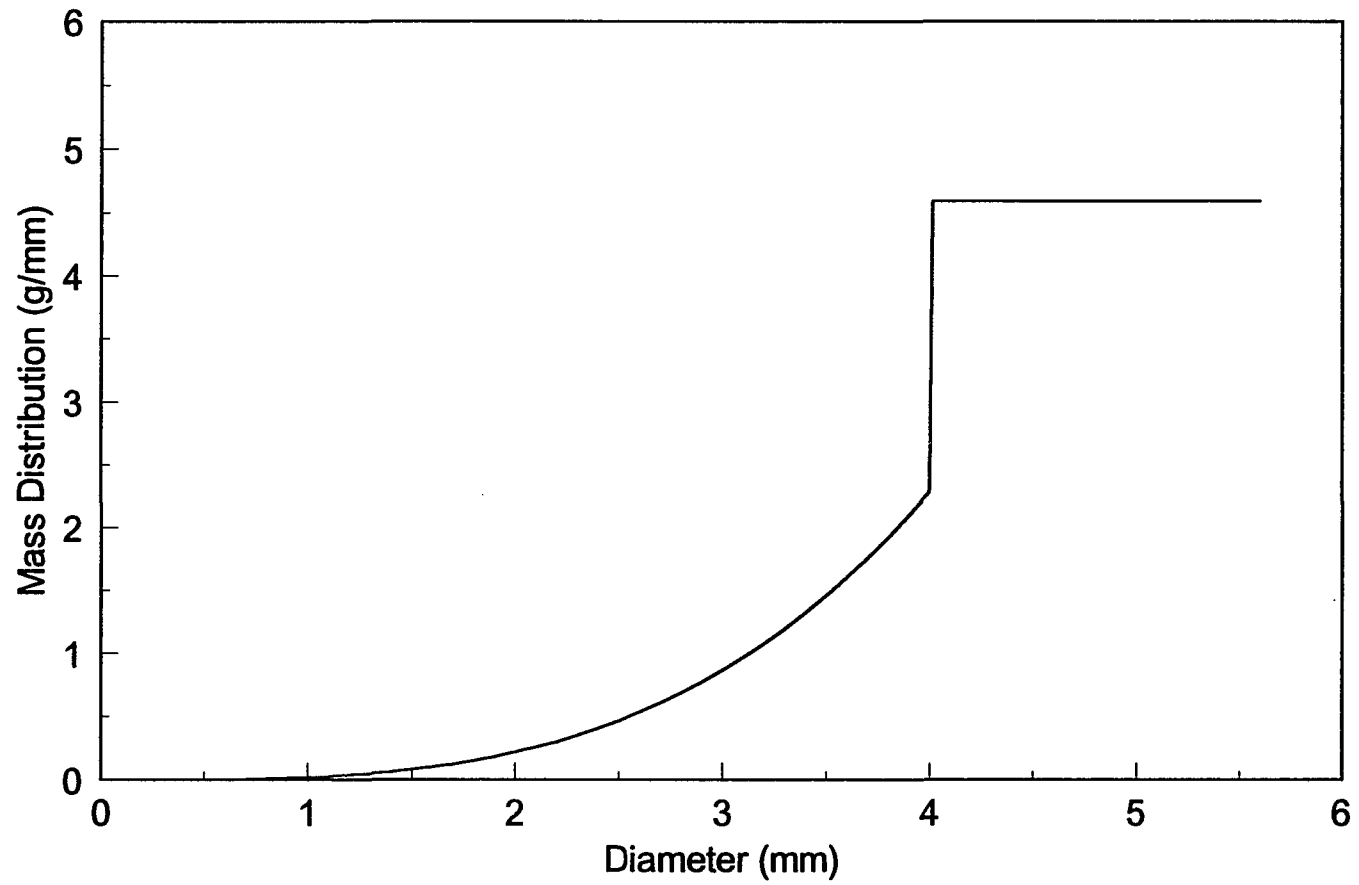


Fig. 5.7: Estimated initial  $\lambda$  distribution

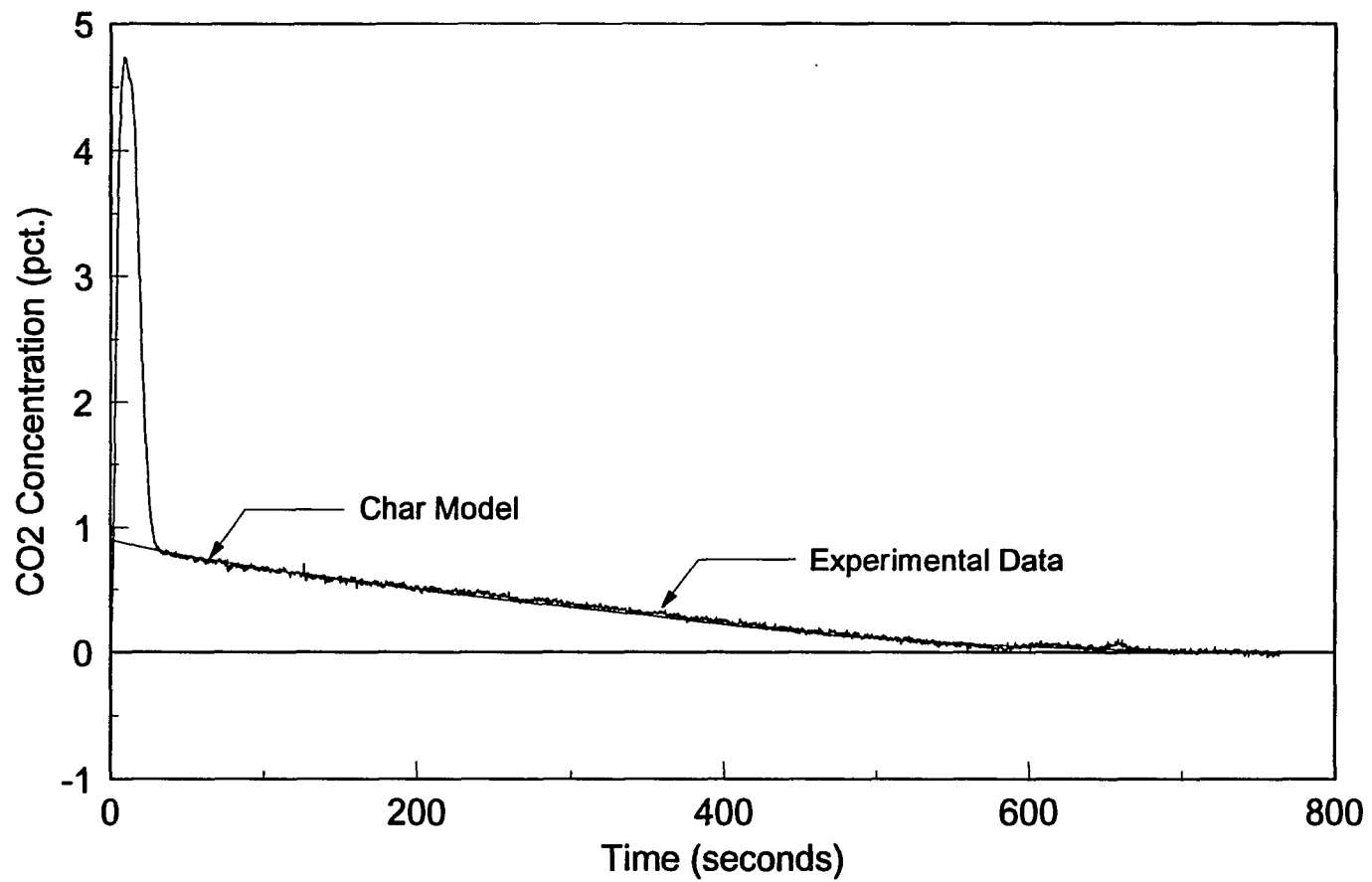


Fig. 5.8: Large particle char model ( $3.5 \times 4$  mesh)

For large char particle distributions, the combustion rate coefficient is significantly greater than those estimated for small particle distributions. The differences in rates likely reflect the differences in (effective) Sherwood numbers. For  $f \propto Sh \propto \sqrt{Re}$ , increases in the particle diameter accompany increases in the mass transfer rate. This explanation is complicated somewhat by the wide distribution of fragmented coal particles. However, if the mean diameter of the small particle distributions is taken as 1 mm and the mean diameter of the large particle distribution is taken as 4.5 mm, the expected ratio of combustion rate coefficients is 2.1. This ratio is close to the experimental ratios, which range from 2.0 to 2.3.

Besides the combustion rate coefficient, the other item worth examining is the curvature of the char response. Some curvature differences exist between the experimental data and the theoretical impulse response. These differences can be corrected by slightly adjusting the curvature of  $\lambda(D, 0^+)$ . Adjusting the curvature of  $\lambda(D, 0^+)$  is warranted in that the differences in the impulse responses are likely due to slight differences in the fragmented particle distributions between the test runs. Curvature deviations notwithstanding, the population balance equation provides useful insights into the combustion dynamics of large char particles.

When coal particles fragment, the resulting char fines have a considerable effect on the impulse response. That these fines influence the impulse response is clearly demonstrated by the differences in the  $\text{CO}_2$  profiles between small particle and large particle distributions. However, consider the extreme case of a fragmented particle distribution that is uniform  $\forall D_o \in (0, D_{\max}]$ . This distribution is shown in Fig. 5.9, and the theoretical char consumption profile for this distribution is illustrated in Fig. 5.10. This response suggests that combustion of small, fragmented char particles might be mistaken for the combustion of volatiles. While a distribution of this sort is unlikely to occur,

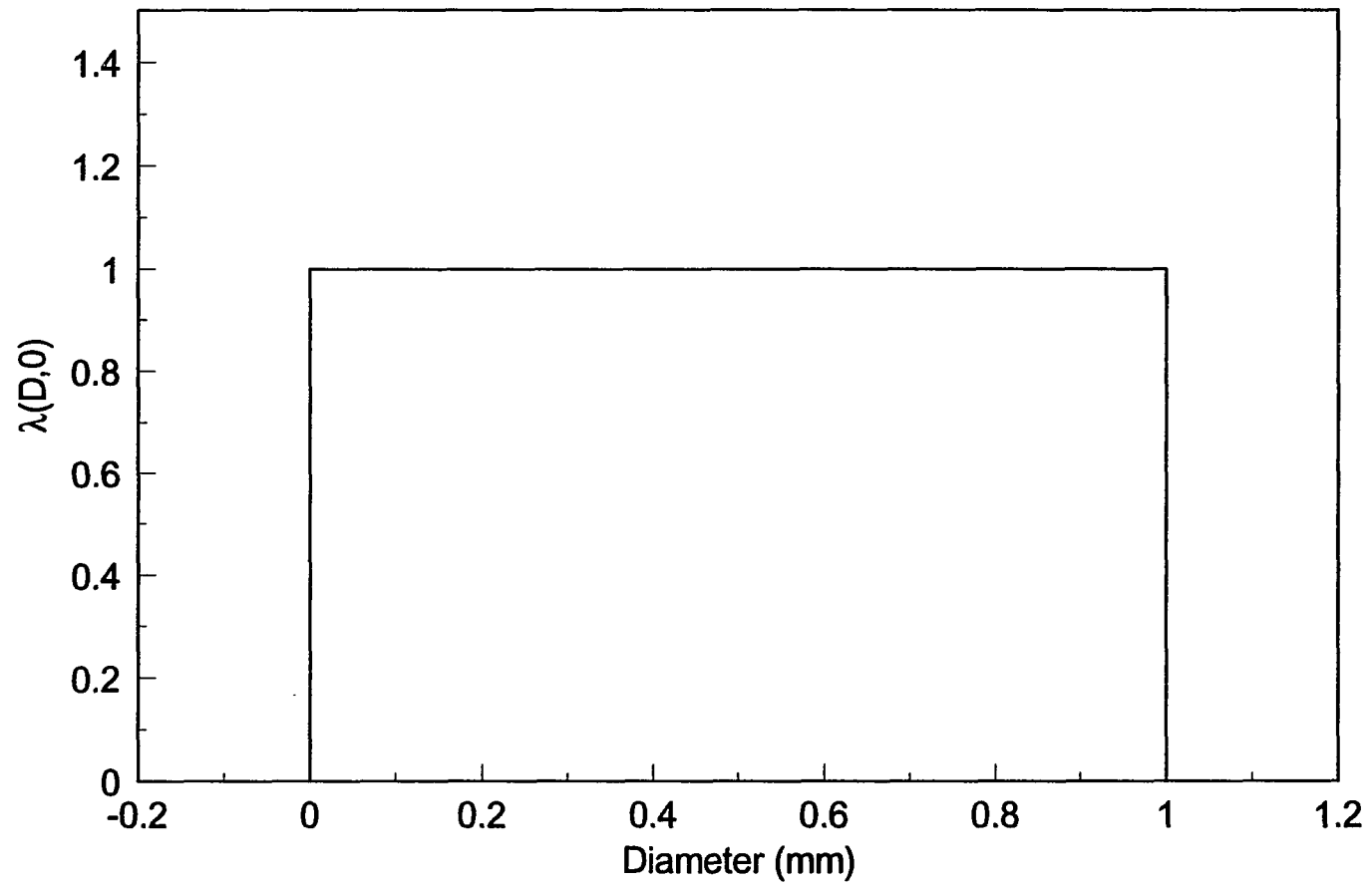


Fig. 5.9: Uniform  $\lambda$  distribution

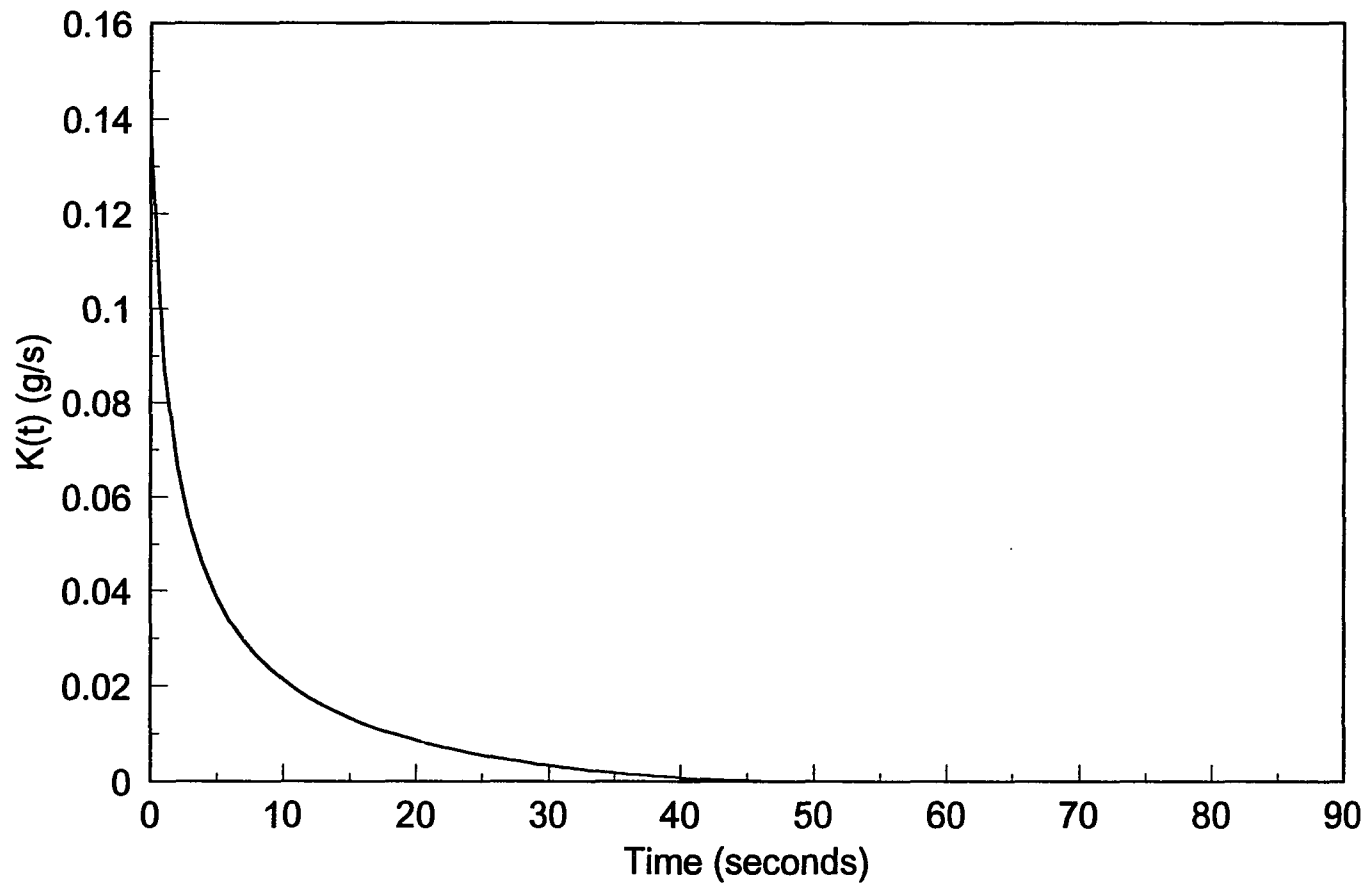


Fig. 5.10: Theoretical impulse response for a uniform  $\lambda$  distribution

consideration must be given to the possibility that the initial response actually comprises combustion of volatiles as well as combustion of char fines.

### 5.3 The Linear Combustion Model: Small Particle Distributions

Since the PMF technique is robust in the presence of noise, it was used to characterize the CO<sub>2</sub> impulse responses for both small and large particle distributions. Transfer function coefficients were estimated from a chain of integrators – a limiting case of the PMF approach. A chain of integrators was chosen since the forcing function is only active at a single instant in time: a chain of integrators will capture this point and retain this information as time progresses. With an impulse input and a chain of integrators, the Poisson moment functionals of the forcing function can be calculated off-line; i.e., for  $t \geq 0$ ,  $u_0(t) = 1$ ,  $u_1(t) = t$ ,  $u_2(t) = t^2 / 2$ , . . . .

In a similar manner, Poisson moment functionals  $y_0(t)$ ,  $y_1(t)$ ,  $y_2(t)$ , . . . are found by successively integrating the output data signal. However, since the PMF approach is parametric, a model structure must be determined before coefficients can be calculated. This can be done by decomposing the nonlinear model into its constituents. For example, CO<sub>2</sub> generation from the combustion of volatiles can be approximated as an exponential decay, which, in the Laplace domain, is given by the transfer function

$$\frac{A}{s + a} \quad (5.3)$$

where  $A$  and  $a$  are unknown constants. Char combustion is a little more complicated. Roughly, the impulse response for a block particle distribution can be modeled as an exponentially damped, phase-shifted sinusoid. In the Laplace domain, this response can be modeled by the transfer function

$$\frac{Bs + C}{s^2 + Ds + E} \quad (5.4)$$

where  $B$ ,  $C$ ,  $D$ , and  $E$  are unknown constants. Combining these components, the total impulse response can be modeled by a third-order system with second-order numerator dynamics:

$$\frac{CO_2(s)}{F_o(s)} = \frac{b_2s^2 + b_1s + b_o}{s^3 + a_2s^2 + a_1s + a_o} \quad (5.5)$$

This linear model was used to estimate the nonlinear  $CO_2$  response for small particle distributions. However, because the volatile response decays quickly, least-squares estimates tend to emphasize char combustion data. To reduce the emphasis on char data, a weighted least-squares procedure was used with the PMF approach to estimate transfer function parameters. Estimated transfer functions and roots of the corresponding characteristic equations for various particle distributions are listed in Table 5.3. Plots of experimental data and transfer function impulse responses are illustrated in Figs. 5.11 through 5.14.

The impulse responses of the estimated transfer functions follow experimental trends well. However, when the impulse responses are decomposed into their constituents (Figs. 5.15 – 5.18), individual components follow theoretical trends poorly. (Indeed, negative  $CO_2$  concentrations for char combustion are unrealistic.) The difficulty stems from modeling char combustion as an exponentially damped, phase-shifted sinusoid. While this model follows char combustion trends at large times, the nonlinear and linear models are initially incompatible. However, since the composite response follows experimental trends well, deficiencies in the char response model are compensated by the volatile response model. In other words, the exponential decay modeling volatile combustion not only models volatile combustion dynamics but also compensates for

Table 5.3: Transfer function estimates for small particle distributions

Particle Distribution	Transfer Function Estimate	Transfer Function Poles (sec <sup>-1</sup> )
16 × 18	$\frac{3.4668s^2 + 0.3718s + 0.0430}{s^3 + 0.3393s^2 + 0.0253s + 0.0009}$	$\lambda_1 = -0.2537$ $\lambda_2 = -0.0428 + 0.0418i$ $\lambda_3 = -0.0428 - 0.0418i$
16 × 20	$\frac{3.8330s^2 + 0.5561s + 0.0736}{s^3 + 0.4032s^2 + 0.0386s + 0.0015}$	$\lambda_1 = -0.2872$ $\lambda_2 = -0.0580 + 0.0441i$ $\lambda_3 = -0.0580 - 0.0441i$
16 × 25	$\frac{3.5980s^2 + 0.5157s + 0.0730}{s^3 + 0.3383s^2 + 0.0359s + 0.0015}$	$\lambda_1 = -0.1899$ $\lambda_2 = -0.0742 + 0.0473i$ $\lambda_3 = -0.0742 - 0.0473i$
16 × 30	$\frac{3.8110s^2 + 0.8380s + 0.1138}{s^3 + 0.4525s^2 + 0.0545s + 0.0023}$	$\lambda_1 = -0.2947$ $\lambda_2 = -0.0789 + 0.0418i$ $\lambda_3 = -0.0789 - 0.0418i$

shortcomings in the char combustion model. Therefore, although the composite responses may follow experimental data well, physical insights into combustion dynamics are tempered by the limitations of modeling nonlinear responses with linear system dynamics.

Despite these limitations, a linear transfer function estimate is useful in modeling the transient response for an arbitrary forcing function. In the time domain, the total CO<sub>2</sub> response is formed by the convolution of the impulse response with the forcing function. Provided that deviations in the coal feed rate are small, the nonlinear impulse response can be replaced by the linear estimate. Difficulties are encountered when nonlinear dynamics significantly alter the nonlinear impulse response, as would be the case for a feed rate that depletes oxygen concentrations in the combustor.

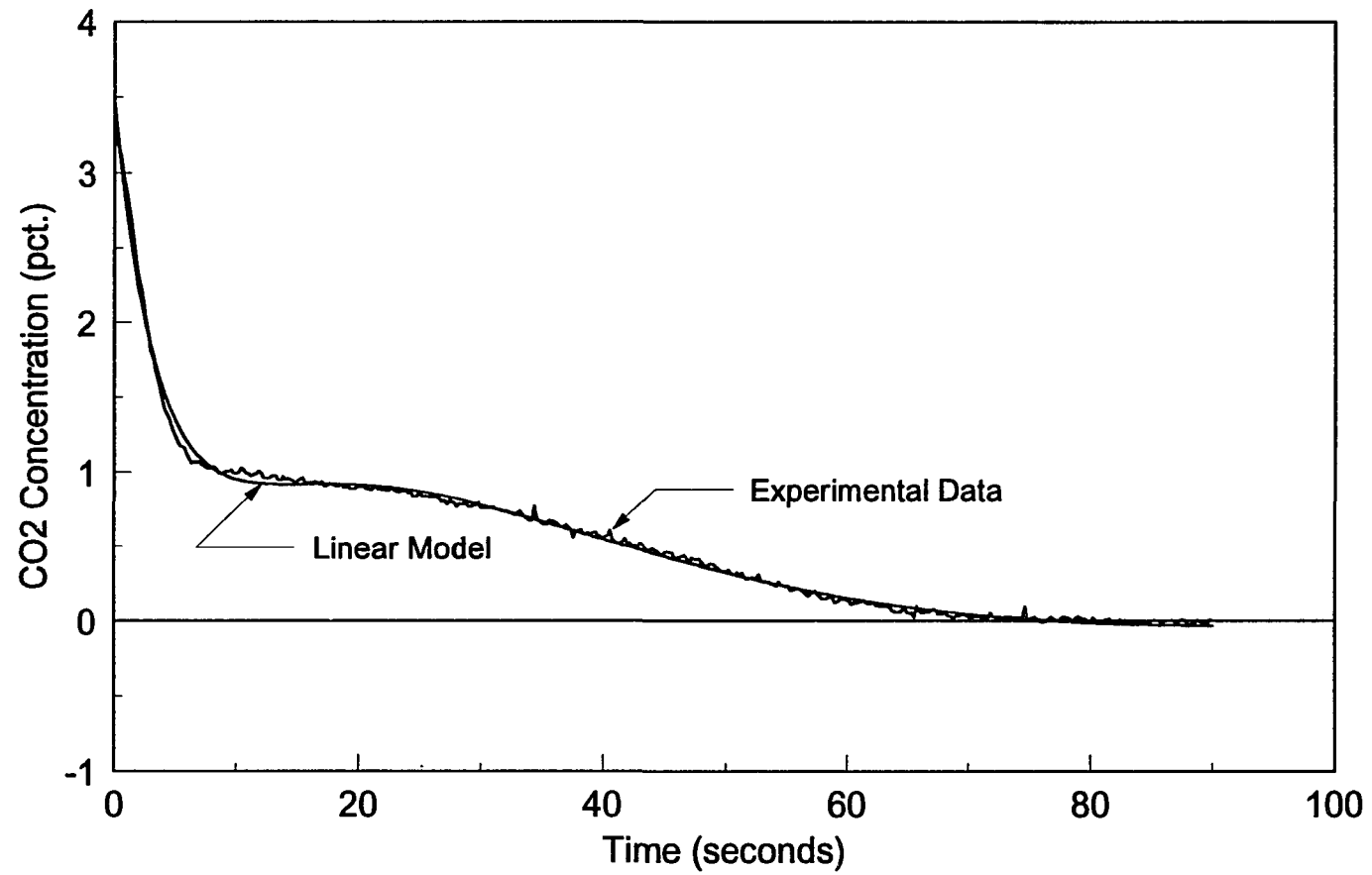


Fig 5.11: Impulse response of the PMF estimated transfer function ( $16 \times 18$  mesh)

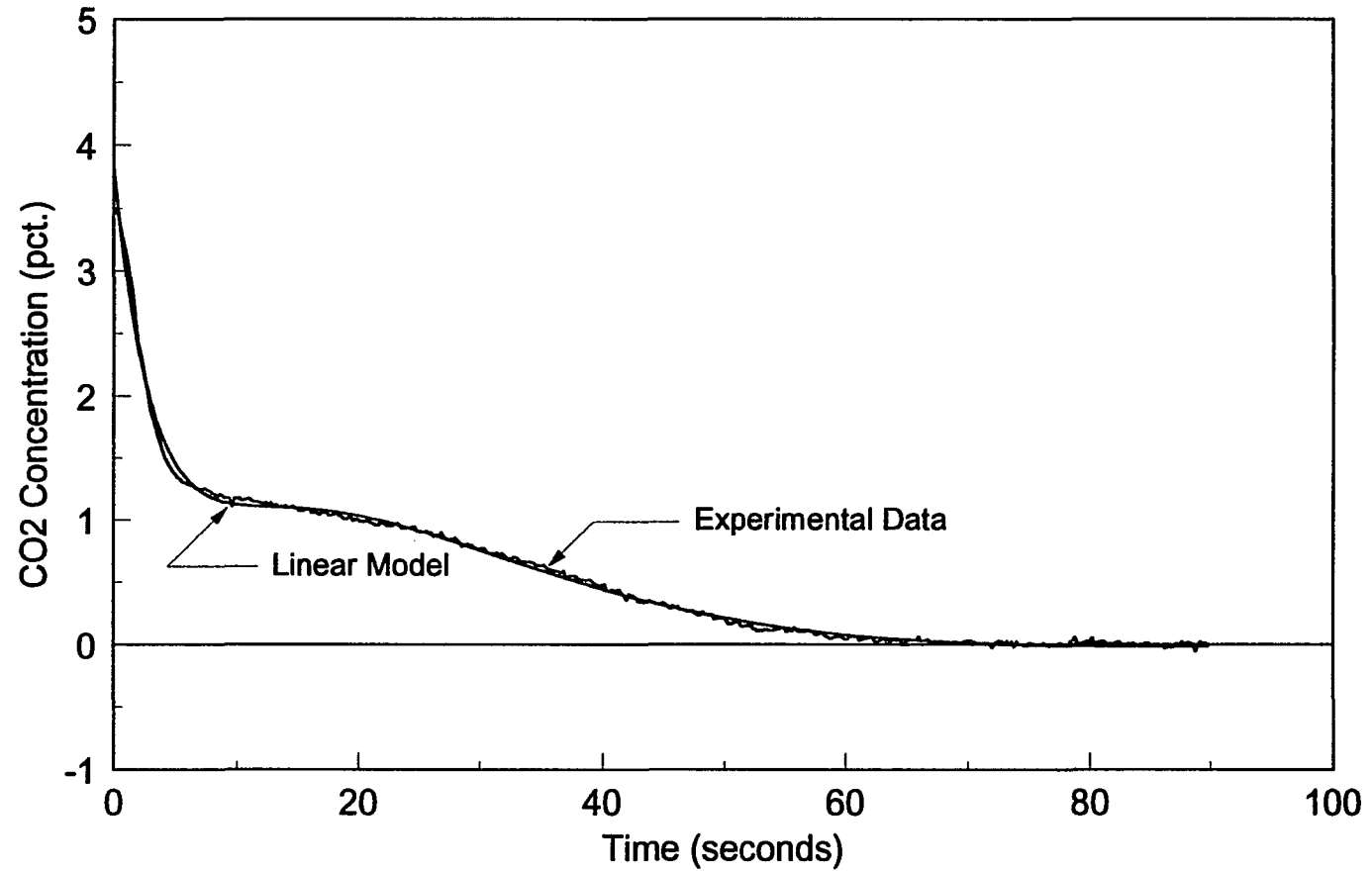


Fig 5.12: Impulse response of the PMF estimated transfer function ( $16 \times 20$  mesh)

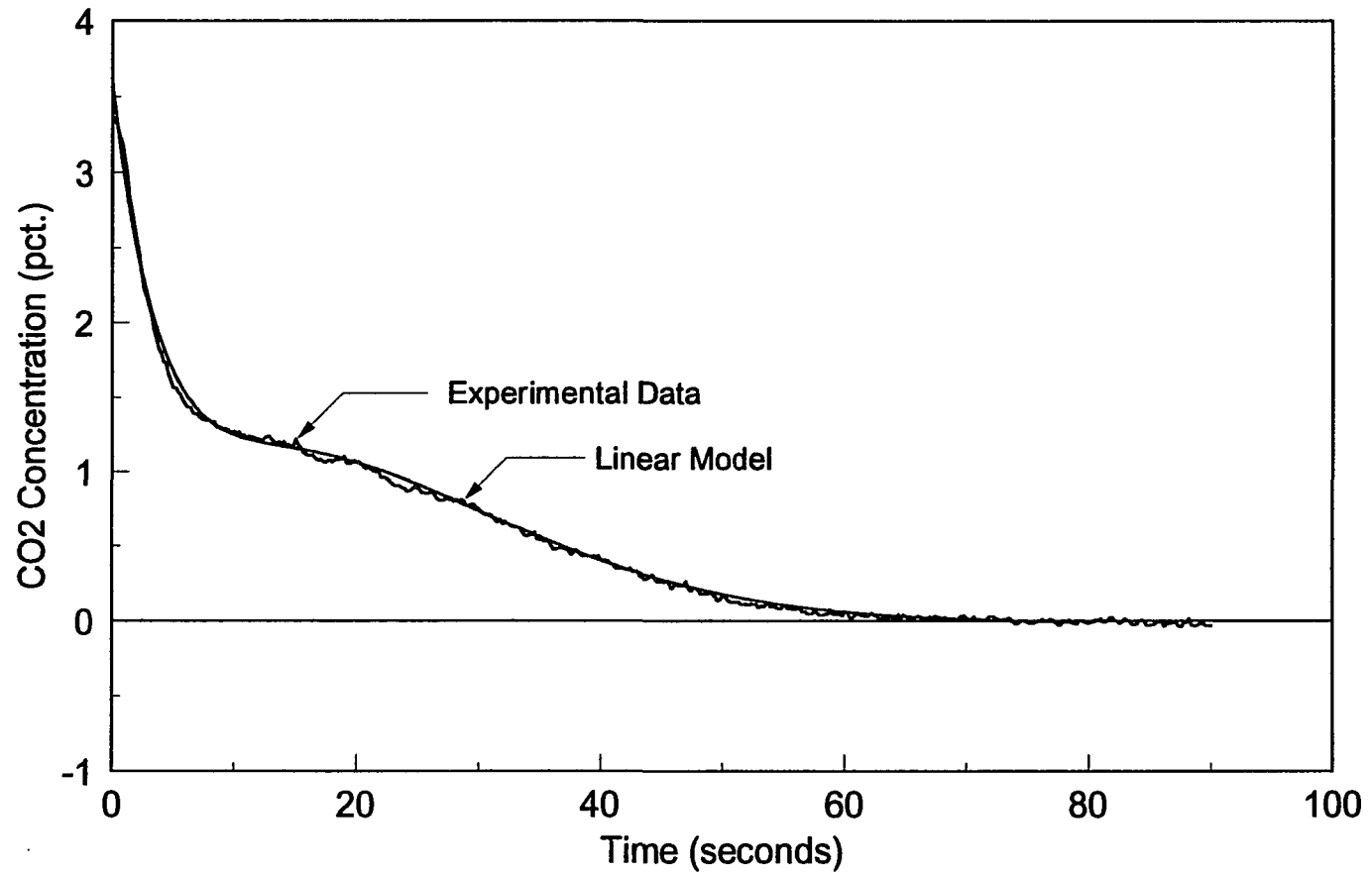


Fig 5.13: Impulse response of the PMF estimated transfer function ( $16 \times 25$  mesh)

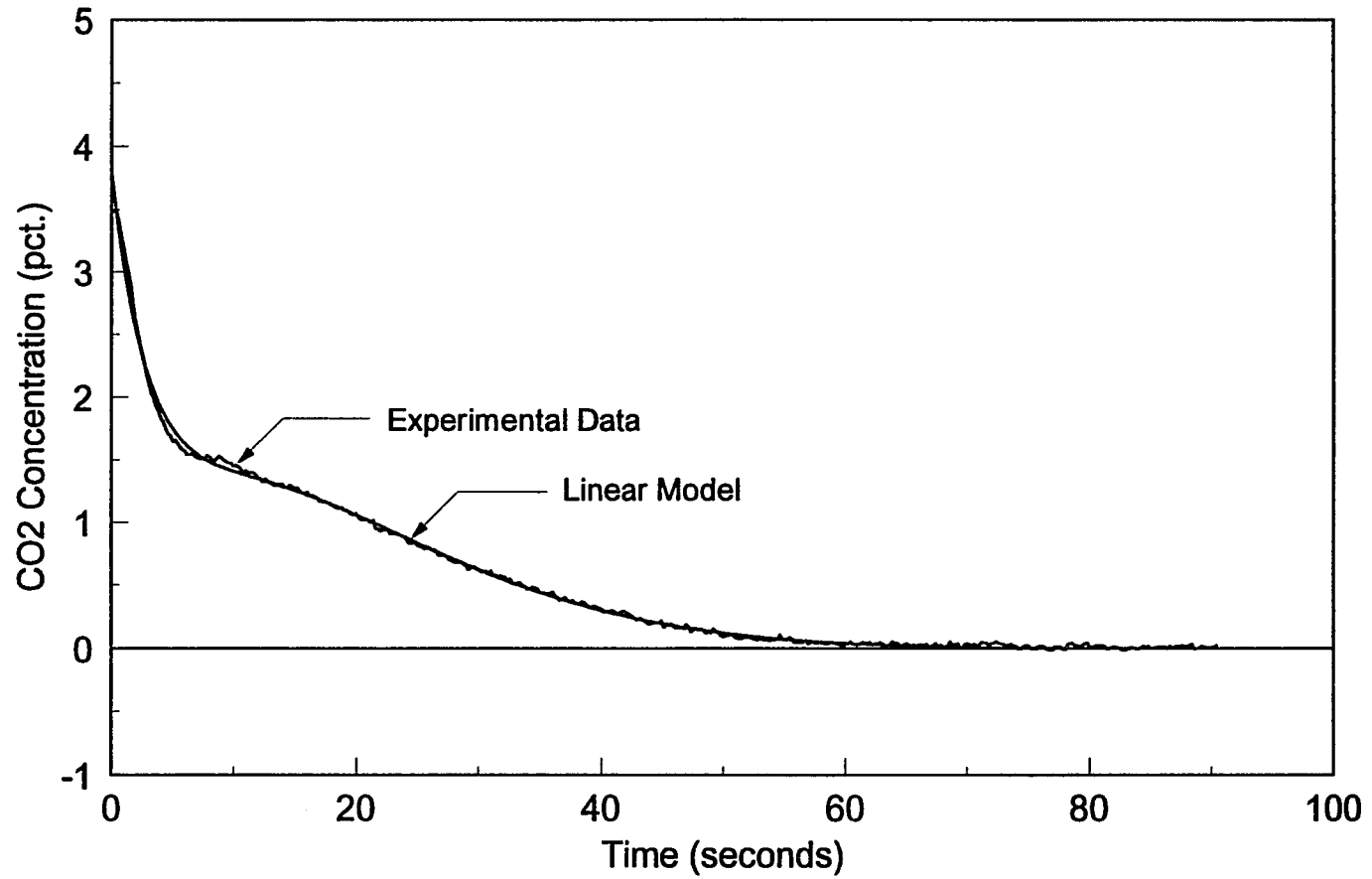


Fig 5.14: Impulse response of the PMF estimated transfer function (16 × 30 mesh)

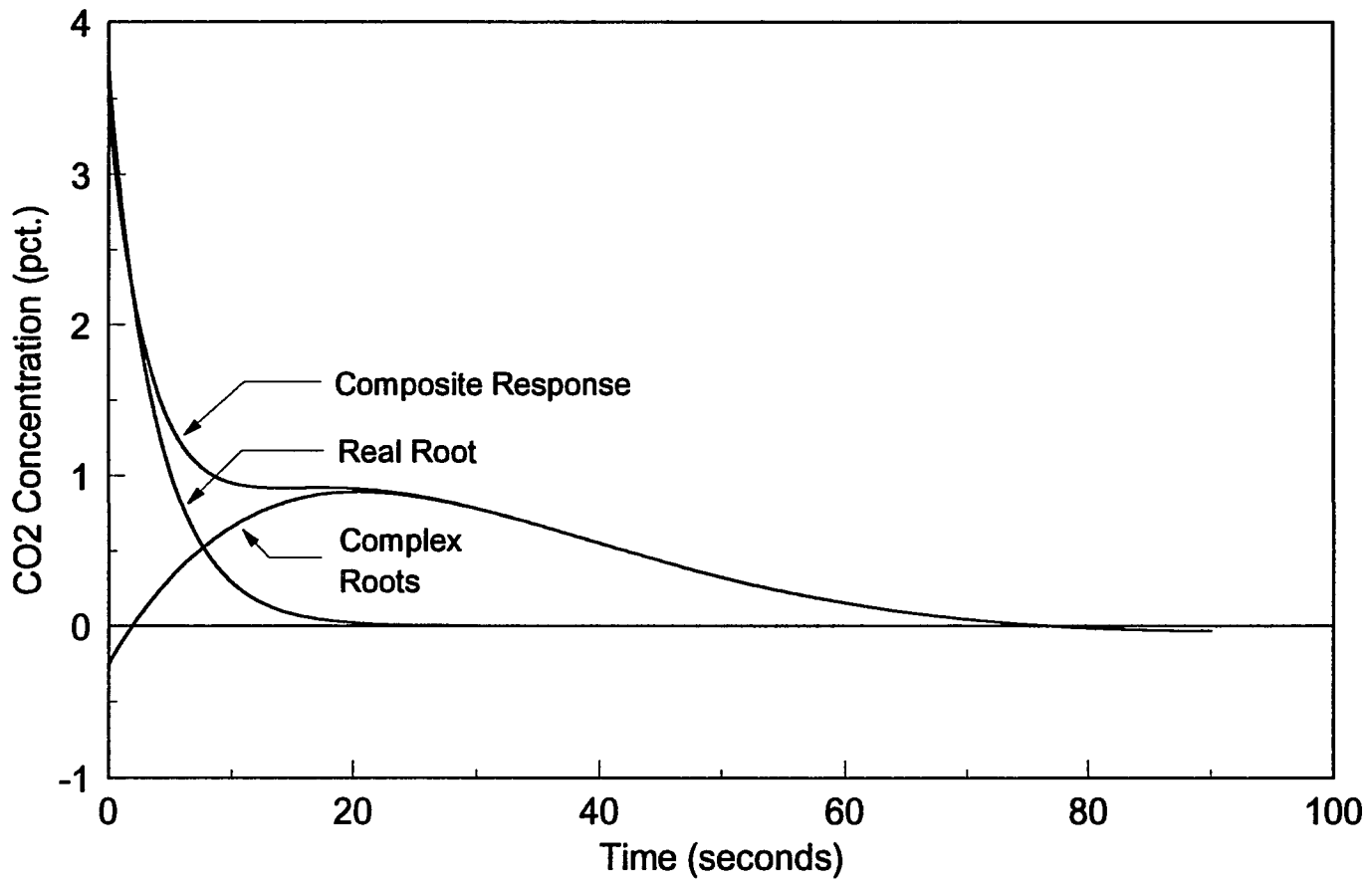


Fig. 5.15: Impulse response of the decomposed transfer function (16 × 18 mesh)

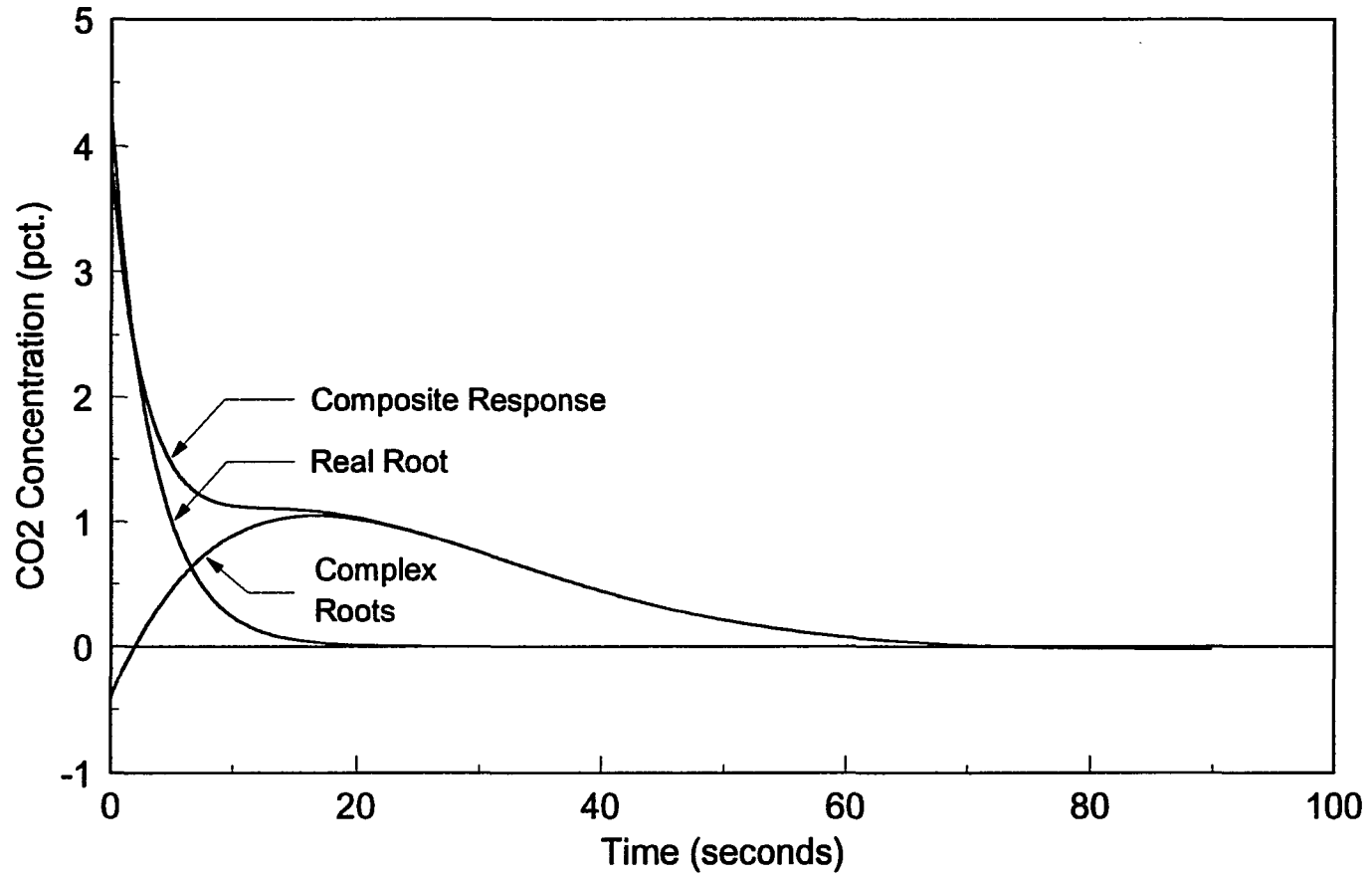


Fig. 5.16: Impulse response of the decomposed transfer function ( $16 \times 20$  mesh)

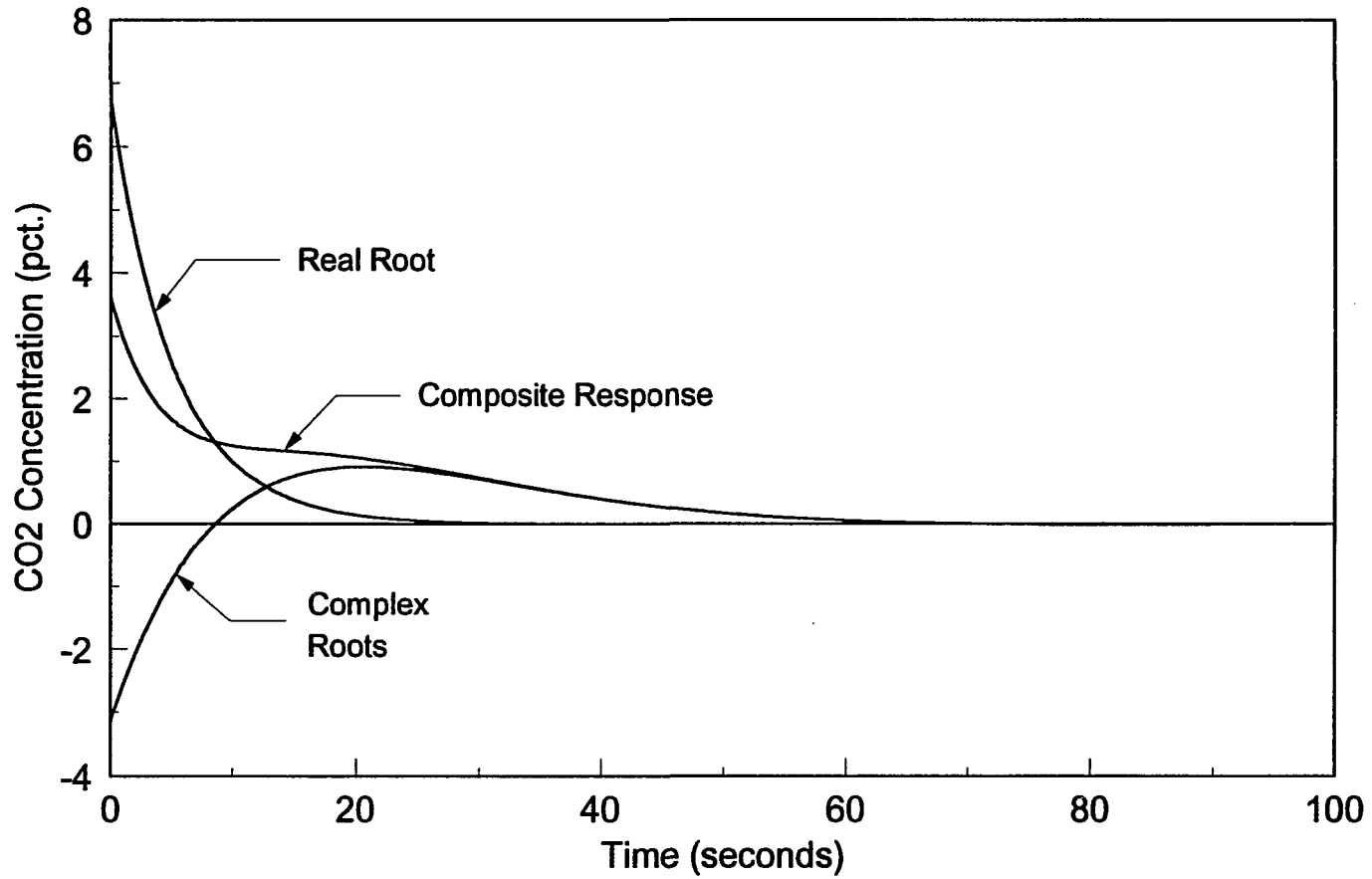


Fig. 5.17: Impulse response of the decomposed transfer function (16 × 25 mesh)

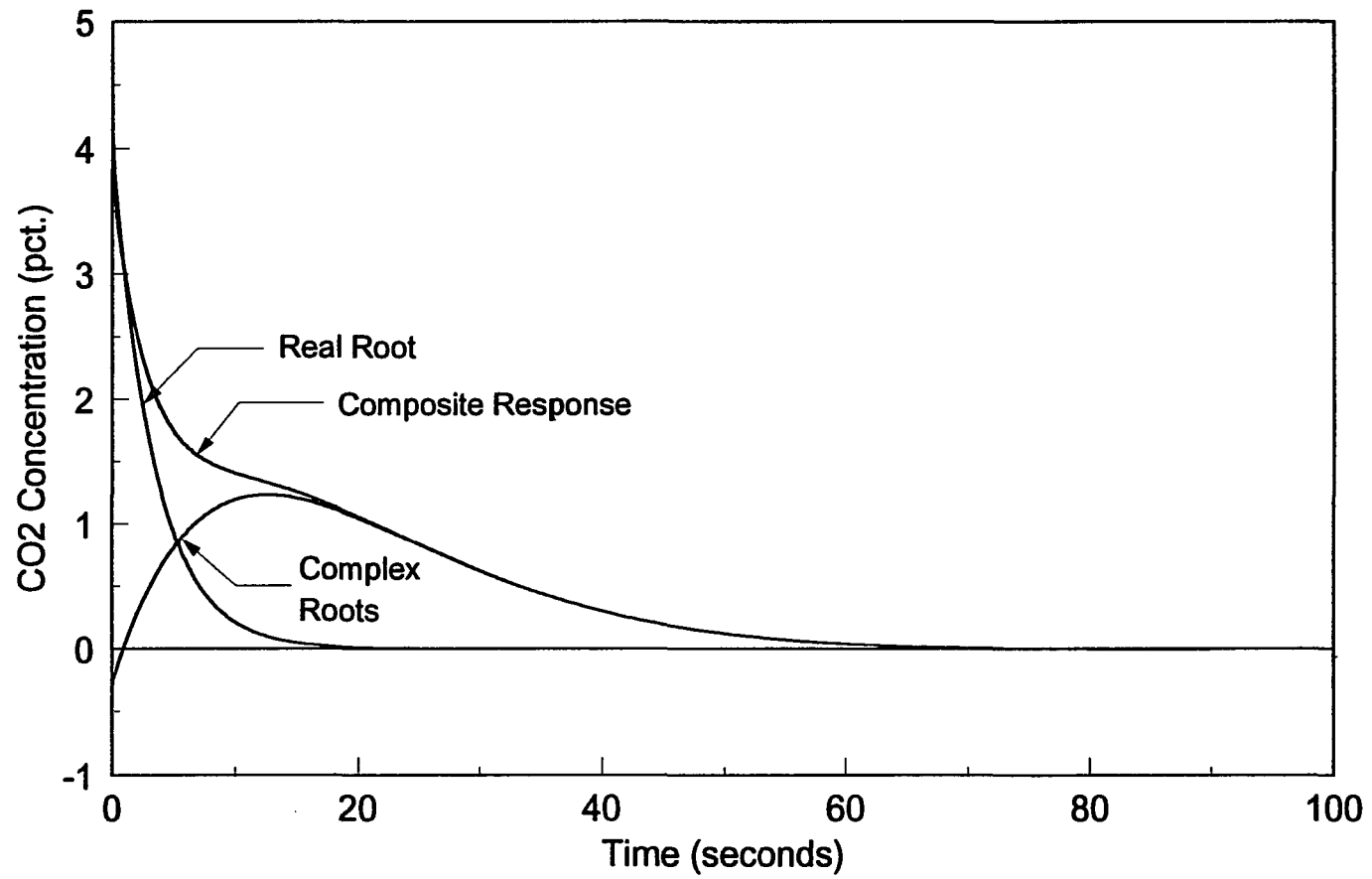


Fig. 5.18: Impulse response of the decomposed transfer function ( $16 \times 30$  mesh)

### 5.4 The Linear Combustion Model: Large Particle Distributions

Calculating theoretical impulse responses for large particle distributions is difficult since the response is based on an unknown – and often unmeasurable – fragmented particle distribution. Ironically, the impulse response for large particle distributions is simpler to model with a linear transfer function since the char combustion transient can be approximated by a slow exponential decay. In the Laplace domain, the char response can be modeled by the transfer function

$$\frac{B}{s+b} \quad (5.5)$$

where  $B$  and  $b$  are unknown constants. Similarly, the volatile response can be modeled with the transfer function

$$\frac{A}{s+a} \quad (5.6)$$

where  $A$  and  $a$  are unknown constants. Combining these exponential functions, the entire  $\text{CO}_2$  response can be modeled as a second-order system with first-order numerator dynamics:

$$\frac{\text{CO}_2(s)}{F_o(s)} = \frac{b_1s + b_o}{s^2 + a_1s + a_o} \quad (5.7)$$

As with the small particle response, a weighted least-squares procedure was used with the PMF approach to estimate transfer function parameters. For the data set in Fig. 5.8, the PMF estimate of the  $\text{CO}_2$  transfer function is

$$\frac{\text{CO}_2(s)}{F_o(s)} = \frac{5.8377s + 0.1738}{s^2 + 0.1540s + 0.0006} \quad (5.8)$$

This transfer function has poles at  $\lambda_1 = -0.1499 \text{ sec}^{-1}$  (volatile combustion) and  $\lambda_2 = -0.0041 \text{ sec}^{-1}$  (char combustion). Plots of the experimental data and the transfer

function impulse response are illustrated in Fig. 5.19; the decomposed impulse response is illustrated in Fig. 5.20.

In this data set, the sharp transition between the volatile response and the char response creates a mismatch between the experimental data and the exponential model. Better fits are obtained when the transition region is less abrupt, as would be the case when fragmented particle distributions contain large quantities of char fines. A data set with this characteristic is illustrated in Fig. 5.21. For this data set, the PMF transfer function estimate is

$$\frac{\text{CO}_2(s)}{F_o(s)} = \frac{3.6389s + 0.0487}{s^2 + 0.1532s + 0.0003} \quad (5.9)$$

This transfer function has poles at  $\lambda_1 = -0.1509 \text{ sec}^{-1}$  (volatile combustion) and  $\lambda_2 = -0.0023 \text{ sec}^{-1}$  (char combustion). The impulse response of this transfer function is superimposed on the experimental data in Fig. 5.21; the decomposed impulse response is illustrated in Fig. 5.22.

If the initial particle distribution is known or can be approximated, physical parameters of the nonlinear response can be estimated from the linear model. For example, consider an initial fragmented distribution that can be approximated by the function

$$\phi_o(D_o) = \begin{cases} aD_o^4, & 0 \leq D_o \leq D_{\max} \\ 0, & \text{Otherwise} \end{cases} \quad (5.10)$$

where  $a$  is a constant. With this initial particle distribution, the population balance equation has the solution

$$\lambda(D,t) = aD^4 h \left( \frac{D_{\max}^2 - D^2}{2f} - t \right) \quad (5.11)$$

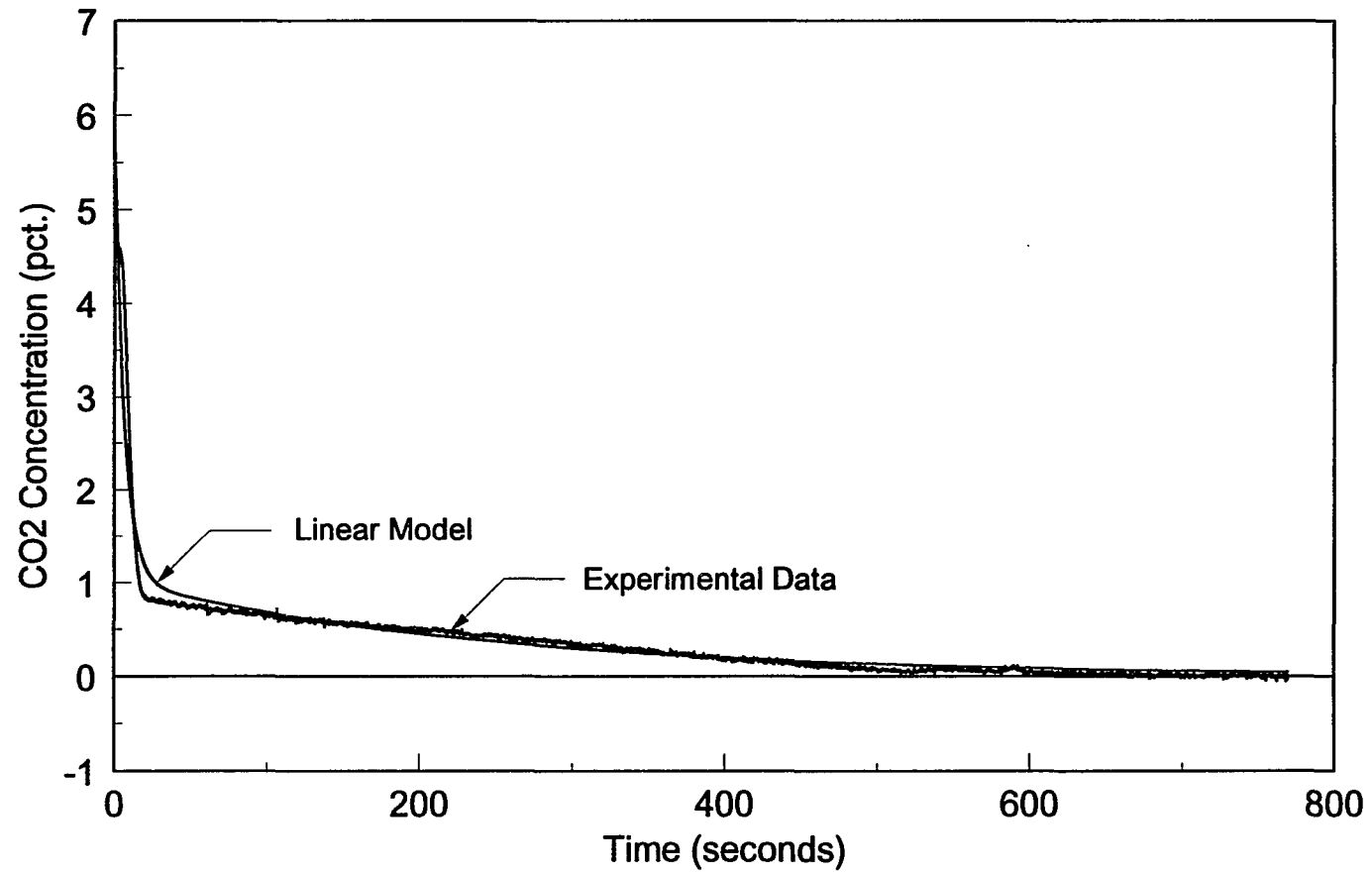


Fig 5.19: Impulse response of the PMF estimated transfer function ( $3.5 \times 4$  mesh)

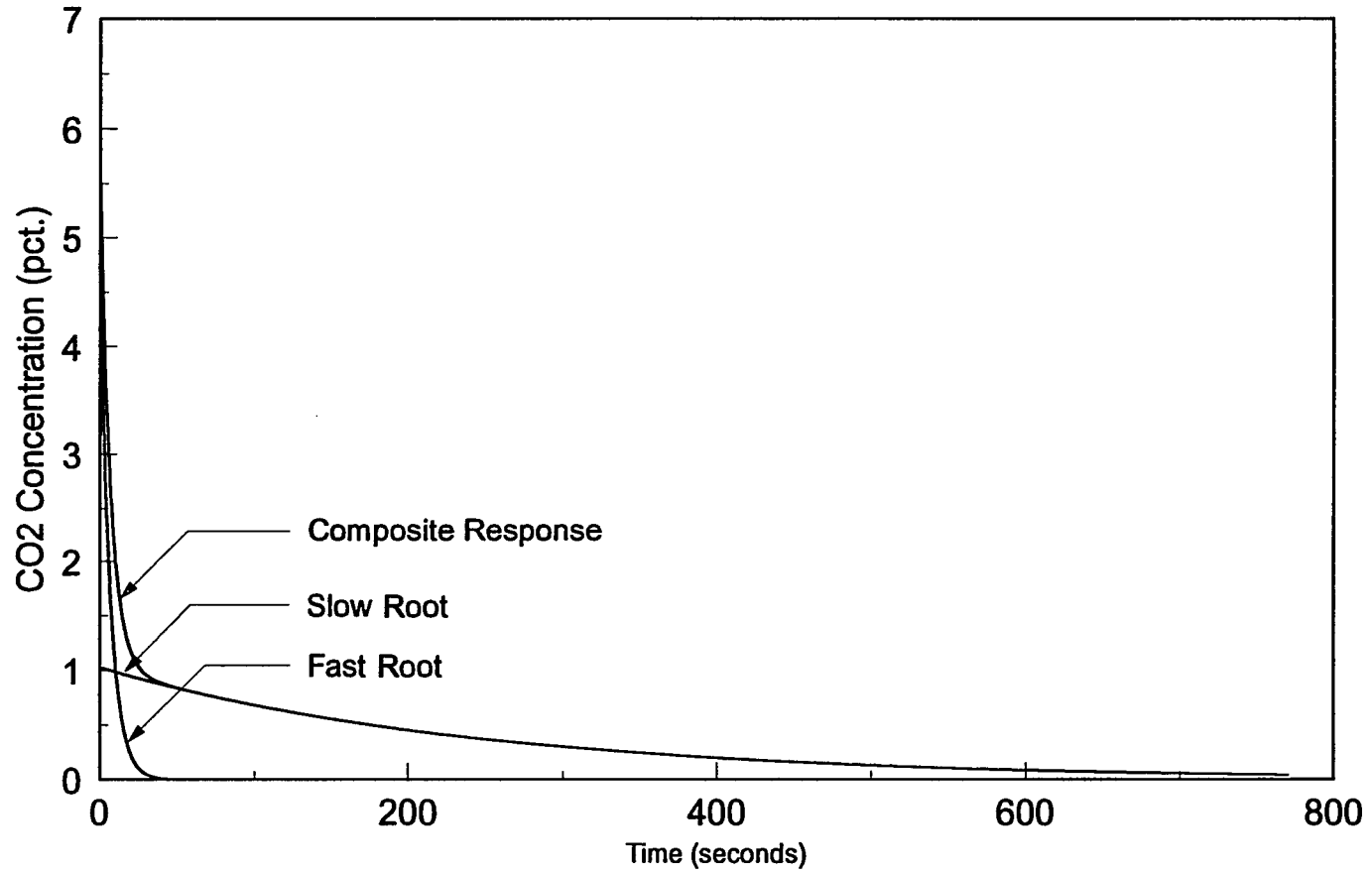


Fig. 5.20: Impulse response of the decomposed transfer function ( $3.5 \times 4$  mesh)

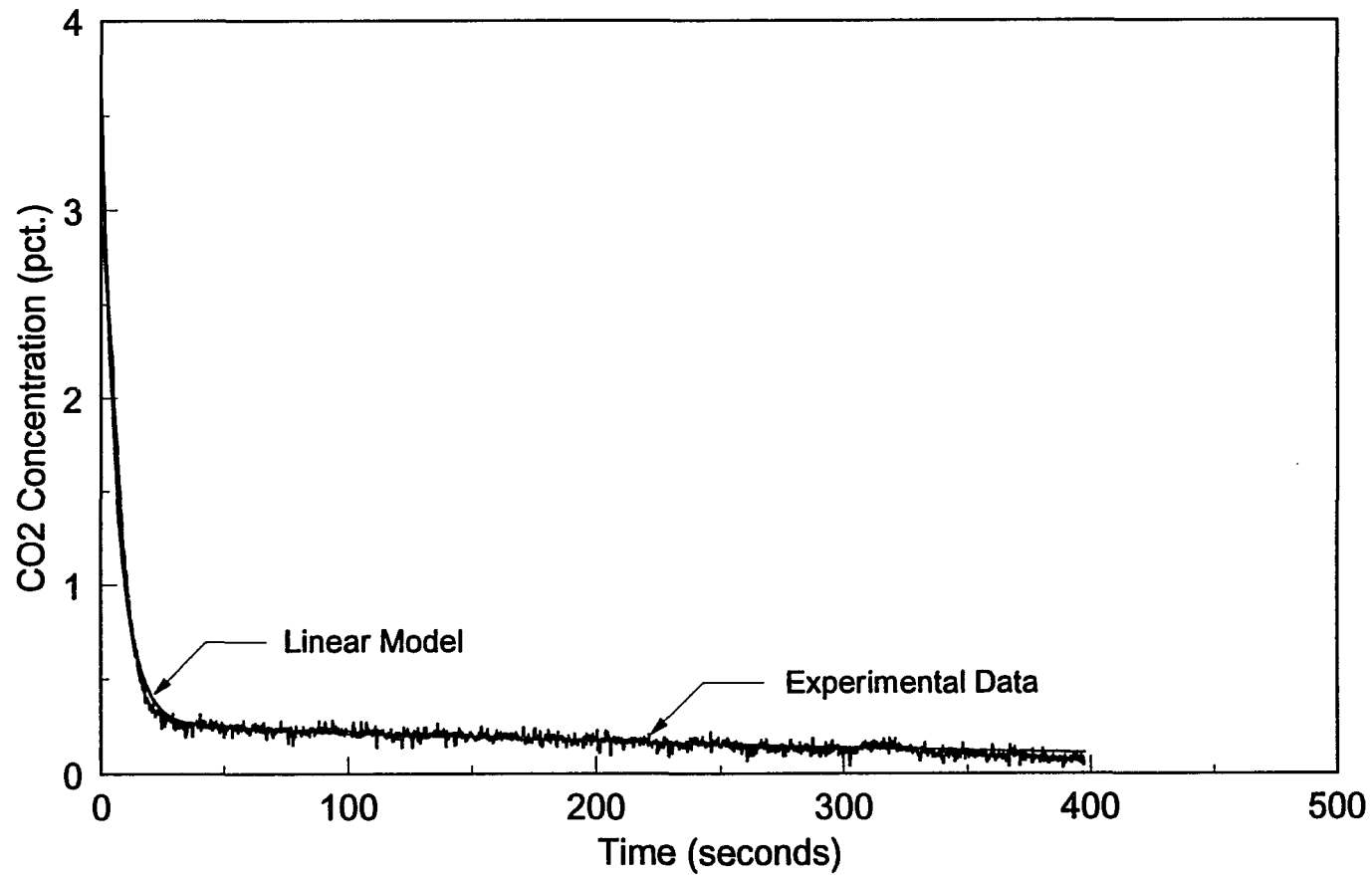


Fig 5.21: Impulse response of the PMF estimated transfer function ( $6 \times 7$  mesh)

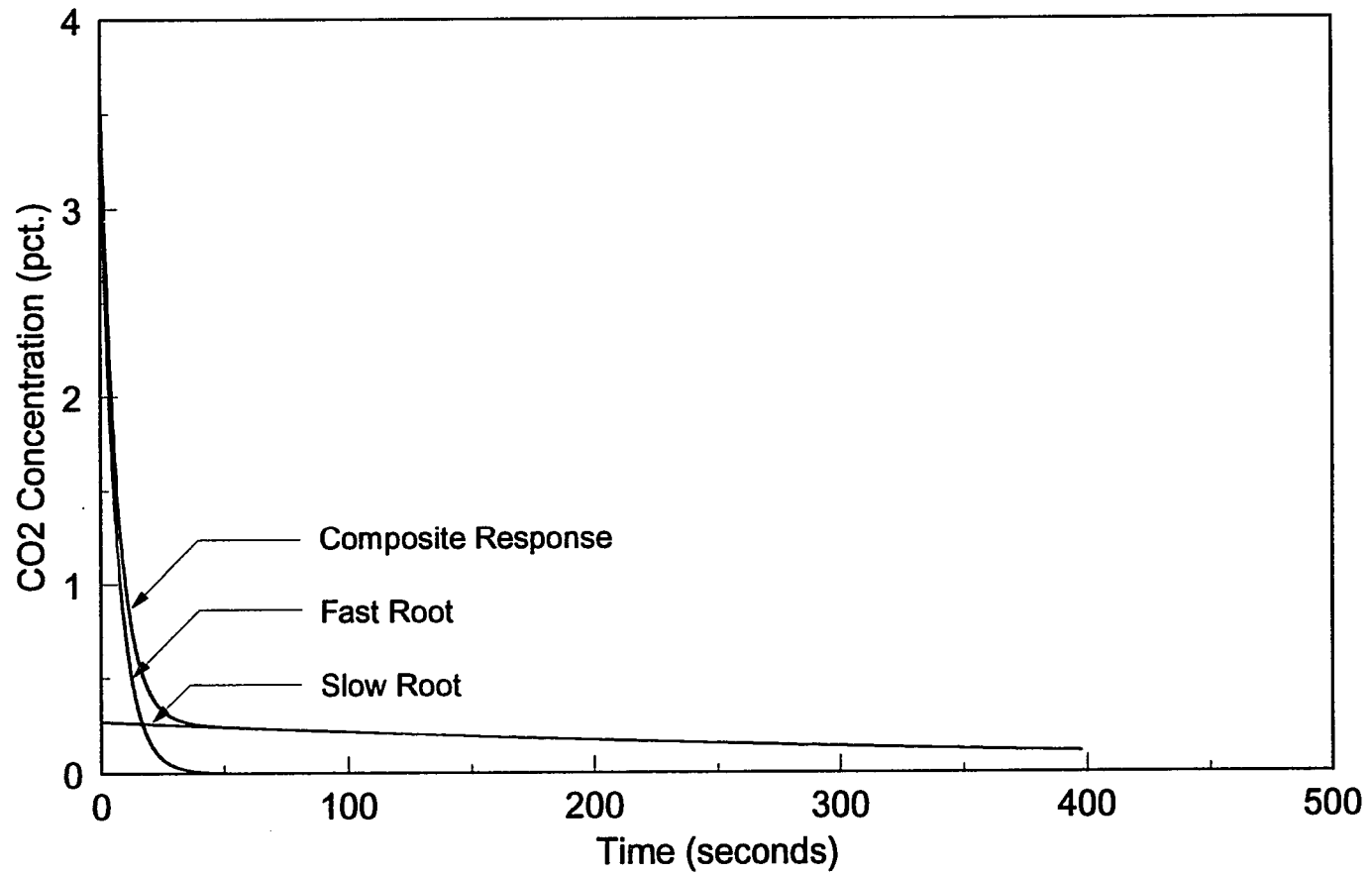


Fig. 5.22: Impulse response of the decomposed transfer function ( $6 \times 7$  mesh)

The rate of char consumption follows directly from the integral

$$K(t) = \int_0^{\infty} \frac{3f\lambda(D,t)}{D^2} dD \quad (5.12)$$

so that

$$K(t) = fa(D_{\max}^2 - 2ft)^{3/2} \quad (5.13)$$

This equation can be expanded in a Maclaurin series and compared term-for-term with a series expansion of an exponential decay. Matching zero- and first-order terms, the nonlinear char combustion model can be approximated by an exponential decay with a time constant of  $D_{\max}^2 / 3f$  seconds. This quantity will vary slightly depending on the structure of the fragmented model.

Clearly, as demonstrated by these examples, the PMF method is a powerful system identification tool. However, these examples also demonstrate that care must be taken when associating physical phenomena with linear system parameters. This is a limitation with all linear system identification algorithms: a good fit does not imply that physical phenomena have been correctly or completely modeled. Nevertheless, with this in mind, linear transfer functions can be used to characterize dynamic responses of nonlinear systems and can often be used to reduce system analysis to manageable levels.

## 6. CONCLUSION

In many studies, the effects of particle distributions have been largely ignored. This study suggests that particle distributions, even narrow distributions, significantly affect the transient response of coal combustion in fluidized beds. Furthermore, this study presents a unified theory that explains the wide differences observed between the impulse responses of small and large coal particles.

While a solution to the population balance equation goes a long way towards modeling char combustion phenomena, it is only a first step. For small particle distributions, the char combustion model presented in this investigation should be refined by relaxing the assumption of a constant emulsion-phase oxygen concentration. Contrary to current thought, oxygen consumption should be incorporated into the population balance equation as a local phenomenon, not a global (i.e., lumped parameter) phenomenon. On the other hand, for large particle distributions, future work should address fragmentation distributions. Indeed, with a solution for an arbitrary particle distribution, it may be possible to ascertain the degree of fragmentation by examining the curvature characteristics of transient combustion responses.

In contrast with models for char combustion, satisfactory models for volatile combustion remain elusive. In this study, the CO<sub>2</sub> measurement system was too sluggish to adequately track volatile transients. Future experiments should incorporate faster CO<sub>2</sub> meters and minimize mixing volumes between the combustion chamber and the meters. However, slower instruments act as low-pass filters, which reduce observation noise. As

with many chemical processes, tradeoffs exist between fast response times and low observation noise.

Besides modeling coal combustion transients, this study highlights some of the difficulties associated with identifying the parameters of processes corrupted by measurement noise. In recent years, much work has been done to further the study of discrete-time identification algorithms. However, many applications, especially those in the process industries, are inherently continuous-time systems with significant measurement noise. Since digital identification methods are sensitive to measurement noise, they may not be appropriate for many industrial applications. Similarly, modern spectral identification techniques require uncorrupted process signals, which limits their practical utility. Fourier techniques work well with corrupted signals, but since these techniques are inconsistent, they require inordinate amounts of data. Like Fourier techniques, continuous-time system identification methods, such as the PMF approach, work well with processes that are corrupted by measurement noise. However, many continuous-time system identification methods remain obscure. With a few notable exceptions, applications of the PMF method are artificial, and few design guidelines have been offered to maximize the capabilities of this method.

Independent of the parameter identification scheme, care must be taken when associating nonlinear physical phenomena with linear system parameters. Many system identification algorithms use a minimum square error criterion or a maximum likelihood criterion. However, these criteria are only meaningful if the model to be estimated has the same structure as the actual system. In other words, these criteria can be applied to any unknown model and any set of data; however, if the underlying model structures are not similar, the estimated parameters have little physical significance. Nevertheless, although the parameters of a linear transfer function may not have physical significance, a transfer

function estimate can still be used to characterize the dynamic response of a nonlinear system.

Whether through linear or nonlinear models, analysis of transient responses is the common thread that runs throughout this investigation. While transient responses are sometimes difficult to model and interpret, they provide a wealth of information that cannot be attained otherwise.

## REFERENCES

- [1] Anthony, D.B., J.B. Howard, H.C. Hottel, and H.P. Meissner (1976). "Rapid devolatilization of pulverized coal," *Fifteenth Symposium (International) on Combustion*, The Combustion Institute, Pittsburgh, Pennsylvania, pp. 1303–1317.
- [2] Astrom, K.J., and B. Wittenmark (1990). *Computer Controlled Systems: Theory and Design*, Prentice Hall, Englewood Cliffs, New Jersey.
- [3] Avedesian, M.M., and J.F. Davidson (1973). "Combustion of carbon particles in a fluidized bed," *Trans. Instn. Chem. Engrs*, Vol. 51, pp. 121–131.
- [4] Bergman, L.A., and A.L. Hale (1983). "Linear system identification via Poisson moment functionals," *AIAA Journal*, Vol. 22, No. 4, pp. 566–568.
- [5] Borghi, G., A.F. Sarofim, and J.M. Beer (1985). "A model of coal devolatilization and combustion in fluidized beds," *Combustion and Flame*, Vol. 61, pp. 1–16.
- [6] Brown, R.G. (1983). *Introduction to Random Signal Analysis and Kalman Filtering*, John Wiley, New York.
- [7] Chirone, R., L. Massimilla, and P. Salatino (1991). "Comminution of carbons in fluidized bed combustion," *Prog. Energy Combust. Sci.*, Vol. 17, pp. 297–326.
- [8] Cho, H. (1988). "System identification of the smoke opacity vs. fuel metering in a diesel engine," Ph.D. dissertation, Iowa State University, Ames, Iowa.
- [9] Cox, C.P. (1987). *A Handbook of Introductory Statistical Methods*, John Wiley, New York.
- [10] Doebelin, E.O. (1980). *System Modeling and Response: Theoretical and Experimental Approaches*, John Wiley, New York.

- [11] Essenhigh, R.H. (1981). "Fundamentals of coal combustion," *Chemistry of Coal Utilization: Second Supplementary Volume*, ed. M.A. Elliott, Wiley-Interscience, New York, pp. 1153–1280.
- [12] Essenhigh, R.H., A.K. Basak, D.W. Shaw, and G. Gangaram (1990). "Evaluation of reactivity functions for coal combustion from particle size analysis in backmix reactors," *Combustion and Flame*, Vol. 79, pp. 307–318.
- [13] Fairman, F.W., and W.C. Shen (1970). "Parameter identification for linear time-varying dynamic processes," *Proc. IEE*, Vol. 117, No. 10, pp. 2025–2029.
- [14] Goodwin, G.C., and K.S. Sin (1984). *Adaptive Filtering, Prediction, and Control*, Prentice-Hall, Englewood Cliffs, New Jersey.
- [15] Graupe, D. (1976). *Identification of Systems*, Robert E. Krieger Publishing Co., Huntington, New York.
- [16] Harris, S.L., and D.A. Mellichamp (1980). "On-line identification of process dynamics: Use of multifrequency binary sequences," *Ind. Eng. Chem. Process Des. Dev.*, Vol. 19, No. 1, pp. 166–174.
- [17] Hayhurst, A.N. (1991). "Does carbon monoxide burn inside a fluidized bed? A new model for the combustion of coal char particles in fluidized beds," *Combustion and Flame*, Vol. 85, pp. 155–168.
- [18] Helstrom, C.W. (1991). *Probability and Stochastic Processes for Engineers*, Macmillan, New York.
- [19] Hsia, T.C. (1977). *System Identification*, Lexington Books, Lexington, Massachusetts.
- [20] Jenkins, G.M., and D.G. Watts (1969). *Spectral Analysis and its Applications*, Holden-Day, San Francisco.
- [21] Kay, S.M. (1988). *Modern Spectral Estimation: Theory and Application*, Prentice-Hall, Englewood Cliffs, New Jersey.
- [22] Kunii, D., and O. Levenspiel (1969). *Fluidization Engineering*, Robert E. Krieger Publishing Co., Malabar, Florida.
- [23] Kwakernaak, H., and R. Sivan (1972). *Linear Optimal Control Systems*, Wiley Interscience, New York.

- [24] La Nauze, R.D. (1985). "Fundamentals of coal combustion in fluidised beds," *Chem. Eng. Res. Des.*, Vol. 63, pp. 3–34.
- [25] Ljung, L., and T. Soderstrom (1983). *Theory and Practice of Recursive Identification*, MIT Press, Cambridge, Massachusetts.
- [26] Marple, S.L., Jr. (1989). "A tutorial overview of modern spectral estimation," *Proceedings IEEE*, Vol. 4, pp. 2152–2157.
- [27] Oppenheim, A.V., and R.W. Schaffer (1989). *Discrete-Time Signal Processing*, Prentice Hall, Englewood Cliffs, New Jersey.
- [28] Press, W.H., B.P. Flannery, S.A. Teukolsky, and W.T. Vetterling (1989). *Numerical Recipes: The Art of Scientific Computing*, Cambridge University Press, New York.
- [29] Ross, I.B., and J.F. Davidson (1981). "Combustion of carbon particles in a fluidised bed," *Trans. Instn. Chem. Engrs*, Vol. 59, pp. 108–114.
- [30] Saha, D.C., and G.P. Rao (1983). *Identification of Continuous Dynamical Systems*, Springer-Verlag, New York.
- [31] Saha, D.C., and S.K. Mandal (1990). "Recursive least-squares parameter estimation in SISO systems via Poisson moment functionals: Part 1. Open-loop systems," *Int. Journal of System Science*, Vol. 21., No. 7, pp. 1205–1216.
- [32] Sarofim, A.F., and J.M. Beer (1978). "Modelling of fluidized bed combustion," *17th Symp. (International) Combustion*, The Combustion Institute, Pittsburgh, Pennsylvania, pp. 189–204.
- [33] Saxena, S.C. (1990). "Devolatization and combustion characteristics of coal particles," *Prog. Energy Combust. Sci.*, Vol. 16, pp. 55–94.
- [34] Suuberg, E.M., W.A. Peters, and J.B. Howard (1978). "Product composition and kinetics of lignite pyrolysis," *Ind. Engr. Chem. Process Des. Dev.*, Vol. 17, pp. 37–46.
- [35] Tuken, T. (1991). "Adaptive torque control of a diesel engine for transient test cycles," Ph.D. dissertation, Iowa State University, Ames, Iowa.

- [36] Turnbull, E., and J.F. Davidson (1984). "Fluidization combustion of char and volatiles from coal," *AiChE Journal*, Vol. 30, No. 6, pp. 881–889.
- [37] Unbehauen, H., and G.P. Rao (1987). *Identification of Continuous Systems*, North-Holland, New York.
- [38] van der Post, A.J., O.H. Bosgra, and G. Boelens (1981). "Modelling the dynamics of fluidisation and combustion on a coal-fired FBC," *Journal of Powder & Bulk Solids Technology*, Vol. 5, No. 4, pp. 32–37.
- [39] Whitfield, A.H. (1986). "Transfer function synthesis using frequency response data," *Int. J. Control*, Vol. 43, No. 5, pp. 1413–1426.

**APPENDIX A: DERIVATION OF EQ. (2.60)**

The analytical solution for the impulse response of a block particle distribution is cumbersome. Fortunately, the impulse response can be adequately approximated up to the point of inflection by the first few terms in a Maclaurin series expansion. Coefficients for the Maclaurin series expansion can be calculated from Eqs. (2.60) through (2.65). A derivation of Eq. (2.60) is presented in this appendix; subsequent equations can be derived in a similar manner.

**Objective:** Show that

$$\lim_{t \rightarrow 0} K(t) = 3f\phi_o \left[ \frac{1}{D_{\min}} - \frac{1}{D_{\max}} \right] \quad (\text{A.1})$$

where

$$K(t) = \frac{3f\phi_o}{4\sqrt{ft}D_{\max}^2D_{\min}^2} \left[ \sqrt{2}D_{\max}^2D_{\min}^2 \tan^{-1} \left( \frac{1}{2} \sqrt{\frac{2}{ft}} \sqrt{D_{\max}^2 - 2ft} \right) - 2D_{\min}^2 \sqrt{ft} \sqrt{D_{\max}^2 - 2ft} \right. \\ \left. - \sqrt{2}D_{\max}^2D_{\min}^2 \tan^{-1} \left( \frac{1}{2} \sqrt{\frac{2}{ft}} \sqrt{D_{\min}^2 - 2ft} \right) + 2D_{\max}^2 \sqrt{ft} \sqrt{D_{\min}^2 - 2ft} \right] \quad (\text{A.2})$$

**Proof:**

Taking advantage of symmetry, only the limit

$$\lim_{t \rightarrow 0} \frac{3f\phi_o}{4\sqrt{ft}D_{\max}^2D_{\min}^2} \left[ \sqrt{2}D_{\max}^2D_{\min}^2 \tan^{-1} \left( \frac{1}{2} \sqrt{\frac{2}{ft}} \sqrt{D_{\max}^2 - 2ft} \right) - 2D_{\min}^2 \sqrt{ft} \sqrt{D_{\max}^2 - 2ft} \right] \quad (\text{A.3})$$

will be evaluated. Before evaluating the limit, recall that an arc tangent can be expanded in the power series

$$\tan^{-1}(x) = \frac{\pi}{2} - \frac{1}{x} + \frac{1}{3x^3} - \frac{1}{5x^5} + \dots \quad |x| > 1 \quad (\text{A.4})$$

Using this power series, the arc tangent in Eq. (A.3) can be expanded about  $t = 0$  as

$$\tan^{-1}\left(\frac{1}{\sqrt{2ft}}\sqrt{D_{\max}^2 - 2ft}\right) = \frac{\pi}{2} - \frac{\sqrt{2ft}}{\sqrt{D_{\max}^2 - 2ft}} + \frac{1}{3}\frac{(2ft)^{3/2}}{(D_{\max}^2 - 2ft)^{3/2}} - \dots \quad (\text{A.5})$$

In this equation,  $\pi/2$  cancels with its symmetric part; therefore, its contribution will be ignored when calculating the limit. Hence,

$$\sqrt{2}\frac{3f\phi_o}{4\sqrt{ft}}\tan^{-1}(\cdot) = -\frac{3}{2}\frac{f\phi_o}{\sqrt{D_{\max}^2 - 2ft}} + \frac{\phi_o f^2 t}{(D_{\max}^2 - 2ft)^{3/2}} - \dots \quad (\text{A.6})$$

which, in the limit, reduces to

$$\lim_{t \rightarrow 0} \sqrt{2}\frac{3f\phi_o}{4\sqrt{ft}}\tan^{-1}(\cdot) = -\frac{3}{2}\frac{f\phi_o}{D_{\max}} \quad (\text{A.7})$$

Furthermore,

$$\lim_{t \rightarrow 0} \frac{3f\phi_o}{4\sqrt{ft}D_{\max}^2 D_{\min}^2} \left[ -2D_{\min}^2 \sqrt{ft} \sqrt{D_{\max}^2 - 2ft} \right] = -\frac{3}{2}\frac{f\phi_o}{D_{\max}} \quad (\text{A.8})$$

Adding the contributions of Eqs. (A.7) and (A.8), the limit of Eq. (A.3) is

$$-3f\phi_o \frac{1}{D_{\max}} \quad (\text{A.9})$$

The symmetric part of the limit is

$$3f\phi_o \frac{1}{D_{\min}} \quad (\text{A.10})$$

Adding Eqs. (A.9) and (A.10) gives Eq. (A.1) and finishes the proof.

In Fig. A.1, first-, second-, and third-order Maclaurin series approximations are superimposed on Eq. (A.2). Plots were generated for  $D_{\min} = 0.80$  mm,  $D_{\max} = 1.00$  mm,  $\phi_o = 1.00$  g/mm, and  $f = 0.01$  mm<sup>2</sup>/s. In the limit as  $D_{\max} \rightarrow D_{\min}$ , the Maclaurin series expansion of Eq. (A.2) reduces to the series expansion for a monodispersed particle distribution. Specifically, the rate of char consumption for a monodispersed particle distribution is given by

$$K(t) = \frac{3fm_o}{D_o^3} \sqrt{D_o^2 - 2ft} \quad (\text{A.11})$$

This equation can be expanded in a Maclaurin series as

$$K(t) = 3\frac{fm_o}{D_o^2} - 3\frac{f^2m_o}{D_o^4}t - \frac{3}{2}\frac{f^3m_o}{D_o^6}t^2 - \frac{3}{2}\frac{fm_o}{D_o^8}t^3 + O(t^4) \quad (\text{A.12})$$

The series coefficients in Eq. (A.12) can be calculated from those for a block particle distribution by taking the limit as  $D_{\max} \rightarrow D_{\min}$ . For example, the first coefficient in Eq. (A.12) can be calculated from

$$\lim_{t \rightarrow 0} K(t) = 3f\phi_o \left[ \frac{1}{D_{\min}} - \frac{1}{D_{\max}} \right] \quad (\text{A.13})$$

by substituting  $\phi_o = m_o/\Delta D$ ,  $D_{\min} = D_o$ , and  $D_{\max} = D_o + \Delta D$  and taking the limit as  $\Delta D \rightarrow 0$ :

$$\begin{aligned} \lim_{\Delta D \rightarrow 0} 3f\phi_o \left[ \frac{1}{D_{\min}} - \frac{1}{D_{\max}} \right] &= \lim_{\Delta D \rightarrow 0} 3\frac{fm_o}{\Delta D} \left[ \frac{1}{D_o} - \frac{1}{D_o + \Delta D} \right] \\ &= \lim_{\Delta D \rightarrow 0} 3\frac{fm_o}{\Delta D} \left[ \frac{\Delta D}{D_o(D_o + \Delta D)} \right] \\ &= 3\frac{fm_o}{D_o^2} \end{aligned} \quad (\text{A.14})$$

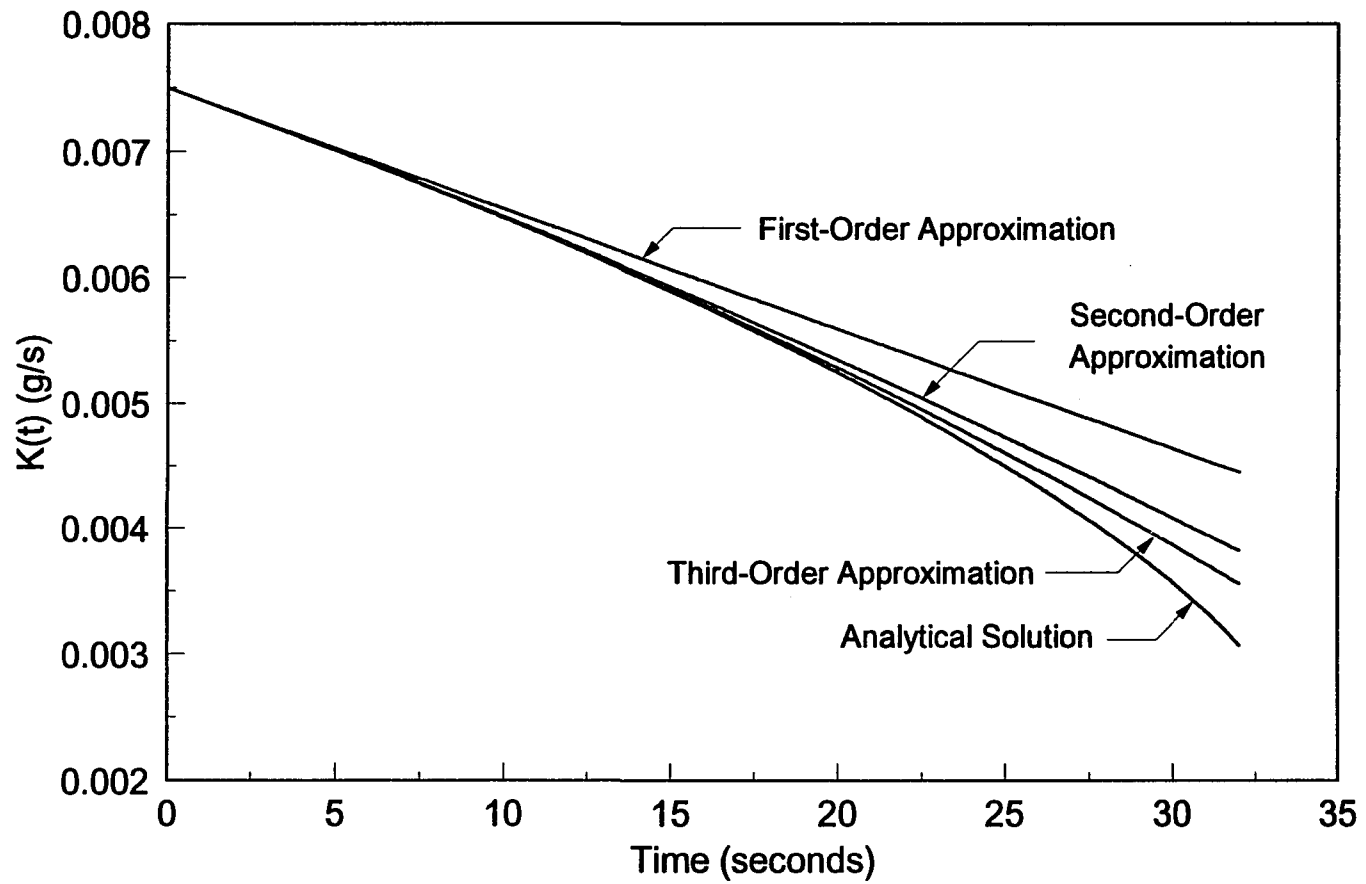


Fig A.1: Maclaurin series approximations of Eq. (A.2)

Likewise, the second coefficient in Eq. (A.12) can be calculated from

$$\lim_{\Delta t \rightarrow 0} K(t) = f^2 \phi_o \left[ \frac{1}{D_{\max}^3} - \frac{1}{D_{\min}^3} \right] \quad (\text{A.15})$$

by substituting  $\phi_o = m_o / \Delta D$ ,  $D_{\min} = D_o$ , and  $D_{\max} = D_o + \Delta D$ , and taking the limit as  $\Delta D \rightarrow 0$ :

$$\begin{aligned} \lim_{\Delta D \rightarrow 0} f^2 \phi_o \left[ \frac{1}{D_{\max}^3} - \frac{1}{D_{\min}^3} \right] &= \lim_{\Delta D \rightarrow 0} \frac{f^2 m_o}{\Delta D} \left[ \frac{1}{(D_o + \Delta D)^3} - \frac{1}{D_o^3} \right] \\ &= \lim_{\Delta D \rightarrow 0} \frac{f^2 m_o}{\Delta D} \left[ \frac{-3D_o^2 \Delta D - 3D_o \Delta D^2 - \Delta D^3}{D_o^3 (D_o + \Delta D)^3} \right] \\ &= -3 \frac{f^2 m_o}{D_o^4} \end{aligned} \quad (\text{A.16})$$

Higher order coefficients for a monodispersed particle distribution can be derived from the coefficients for a block particle distribution in a similar manner.

## APPENDIX B: ELS AND PMF MATLAB MACROS

Performance characteristics of the ELS and PMF approaches to system identification were evaluated through Matlab simulations. Matlab macro codes for these identification schemes are presented in this appendix. Comment lines are preceded by a percent sign.

```

%                               Matlab v. 3.5f Macro: ELS
%                               Parameter Estimates
% Nomenclature
%
%   den      = Transfer function denominator
%   e        = Error estimate
%   n        = Number of iterations
%   noise    = Zero-mean additive measurement noise
%   nsr      = Noise-to-signal ratio (pct.)
%   num      = Transfer function numerator
%   p1       = P(k-1)
%   p2       = P(k-2)
%   param    = Parameter estimate trajectory
%   phi1     =  $\phi(k-1)$ 
%   theta    = Parameter vector,  $\theta(k)$ 
%   theta1   =  $\theta(k-1)$ 
%   u        = System input
%   y        = System output with measurement noise
%   yideal   = Uncorrupted system output

% Initialize system parameters

echo on
n = 1000;

```

```

nsr = 1;                                % 1 pct. measurement noise

% Define the transfer function in decreasing powers of s

num = [3.5];
den = [1, 3, 3.5];

% Calculate the discrete-time transfer function (with a zero-order hold)

[dnum,dden] = c2dm(num,den,1/15,'zoh');

% Generate output data to input u(k), k = 1,2,3, ...,n

u = randn(n,1);                          % randn generates unity variance,
[yideal,x] = dlsim(dnum,dden,u);          % zero-mean Gaussian random noise

var = cov(yideal);
noise = sqrt(nsr / 100 * var) * randn(n,1);
y = yideal + noise;

% ELS algorithm

theta1 = [0 0 0 0 0 0]';
p2 = 1000 * eye(6);
e1 = 0;
e2 = 0;
param = theta1';

for i = 3:n;
    phi1 = [-y(i-1), -y(i-2), u(i-1), u(i-2), e1, e2]';
    yhat = phi1' * theta1;
    p1 = p2 - p2 * phi1 * phi1' * p2 / (1 + phi1' * p2 * phi1);
    theta = theta1 + p1 * phi1 * (y(i) - yhat);
    e2 = e1;
    e1 = y(i) - phi1' * theta;          % A Posteriori Prediction
    p2 = p1;
    theta1 = theta;
    param = [param; theta'];
end;

return

```

```

%                               Matlab v. 3.5f Macro: PMF
%                               Parameter Estimates
% Nomenclature
%
%   b       = Estimated parameter vector
%   den     = Transfer function denominator
%   lam     = Filter coefficient
%   n       = Number of iterations
%   noise   = Zero-mean additive measurement noise
%   nsr     = Noise-to-signal ratio (pct.)
%   num     = Transfer function numerator
%   u       = System input
%   x*      = Temporary storage vector
%   y       = System output with measurement noise
%   yideal  = Uncorrupted system output

% Initialize system parameters

    echo on
    clear

    nsr = 1;                % 1 pct. measurement noise
    n = 1000;
    lam = 1.8;

% Define the transfer function in decreasing powers of s

    num = 3.5;
    den = [1, 3, 3.5];

    u = randn(n,1);        % randn generates zero-mean, unity variance
    dt = 1/100;           % Gaussian random noise
    t = dt * [0:(n-1)]';

% Generate output data to input u(k), k = 1,2,3,...,n

    [yideal,xdum] = lsim(num,den,u,t);

    var = cov(yideal);
    noise = sqrt(nsr/100 * var) * randn(n,1);
    y = yideal + noise;

```

**% Calculate the PMF parameter estimates (collectively, in state-space form)**

```

a = [-lam, 0, 0; 1, -lam, 0; 0, 1, -lam];
b = [1 0 0]';
c = eye(3);
d = [0 0 0]';

```

```

[xU,xdum] = lsim(a,b,c,d,u,t);
[xY,xdum] = lsim(a,b,c,d,y,t);

```

```

yo = xY(:,1);
y1 = xY(:,2);
y2 = xY(:,3);

```

```

uo = xU(:,1);
u1 = xU(:,2);
u2 = xU(:,3);

```

```

x = [y1-lam*y2, y2, -u2];
z = [-yo+2*lam*y1-lam^2*y2];

```

```

b = inv(x'*x)*(x'*z);
num = b(3);
den = [1 b(1) b(2)];

```

**% Calculate equivalent discrete-time model**

```

[dnum,dden] = c2dm(num,den,1/15, 'zoh');

```

```

return

```

**APPENDIX C: DERIVATION OF EQ. (3.72)**

The PMF transform of  $f(t)$  over the interval  $0 \leq t \leq t_o$  is defined as

$$M_k[f(t)] = f_k(t_o) = \int_0^{t_o} f(t) p_k(t_o - t) dt \quad (C.1)$$

$$p_k(t_o) = \frac{t_o^k}{k!} e^{-\lambda t_o}, \quad \lambda \geq 0, \quad k = 0, 1, 2, 3, \dots$$

The PMF transform of  $f'(t)$  about  $t_o$  is defined in a similar manner:

$$M_k[f'(t)] = \int_0^{t_o} \frac{(t_o - t)^k}{k!} e^{-\lambda(t_o - t)} f'(t) dt \quad (C.2)$$

The right-hand side of this equation can be integrated by parts:

$$\int_0^{t_o} \frac{(t_o - t)^k}{k!} e^{-\lambda(t_o - t)} f'(t) dt = \left. \frac{(t_o - t)^k}{k!} e^{-\lambda(t_o - t)} f(t) \right|_0^{t_o}$$

$$- \int_0^{t_o} \left[ -\frac{(t_o - t)^{k-1}}{(k-1)!} e^{-\lambda(t_o - t)} + \lambda \frac{(t_o - t)^k}{k!} e^{-\lambda(t_o - t)} \right] f(t) dt \quad (C.3)$$

which gives

$$M_k[f'(t)] = f_{k-1}(t_o) - \lambda f_k(t_o) - p_k(t_o) f(0) \quad (C.4)$$

Likewise, the PMF transform of  $f''(t)$  about  $t_o$  is defined as

$$M_k[f''(t)] = \int_0^{t_o} \frac{(t_o - t)^k}{k!} e^{-\lambda(t_o - t)} f''(t) dt \quad (C.5)$$

Integrating the right-hand side by parts gives

$$\int_0^{t_0} \frac{(t_0 - t)^k}{k!} e^{-\lambda(t_0 - t)} f''(t) dt = \frac{(t_0 - t)^k}{k!} e^{-\lambda(t_0 - t)} f'(t) \Big|_0^{t_0} - \int_0^{t_0} \left[ -\frac{(t_0 - t)^{k-1}}{(k-1)!} e^{-\lambda(t_0 - t)} + \lambda \frac{(t_0 - t)^k}{k!} e^{-\lambda(t_0 - t)} \right] f'(t) dt \quad (\text{C.6})$$

which reduces to

$$\begin{aligned} M_k[f''(t)] &= -p_k(t_0)f'(t_0) + M_{k-1}[f'(t)] - \lambda M_k[f'(t)] \\ &= f_{k-2}(t_0) - 2\lambda f_{k-1}(t_0) + \lambda^2 f_k(t_0) \\ &\quad - [p_{k-1}(t_0) - \lambda p_k(t_0)]f(0) - p_k(t_0)f'(0) \end{aligned} \quad (\text{C.7})$$